GEOSPHERE

GEOSPHERE, v. 19, no. 1

https://doi.org/10.1130/GES02548.1

21 figures; 6 tables; 1 set of supplemental files

CORRESPONDENCE: wuchen@itpcas.ac.cn

CITATION: Li, J., Wu, C., Chen, X., Yin, A., Zuza, A.V., Haproff, P.J., Chen, Y., Wang, L., and Shao, Z., 2022, Tectonic setting of metamorphism and exhumation of eclogite-facies rocks in the South Beishan orogen, northwestern China: Geosphere, v. 19, no. 1, p. 100–138, https://doi.org/10.1130/GES02548.1

Science Editor: Andrea Hampel Associate Editor: Jason W. Ricketts

Received 10 May 2022 Revision received 9 September 2022 Accepted 30 September 2022

Published online 6 December 2022





This paper is published under the terms of the CC-BY-NC license.

© 2022 The Authors

Tectonic setting of metamorphism and exhumation of eclogitefacies rocks in the South Beishan orogen, northwestern China

Jie Li¹.².³, Chen Wu¹, Xuanhua Chen³, An Yin⁴, Andrew V. Zuza⁵, Peter J. Haproff¢, Yanfei Chen³, Luojuan Wang³, and Zhaogang Shao³

- State Key Laboratory of Tibetan Plateau Earth System, Environment and Resources (TPESER), Institute of Tibetan Plateau Research, Chinese Academy of Sciences, Beijing 100101, China
- ²School of Earth Sciences and Resources, China University of Geosciences (Beijing), Beijing 100083, China
- ³SinoProbe Center, Chinese Academy of Geological Sciences, Beijing 100037, China
- ⁴Department of Earth, Planetary, and Space Sciences, University of California, Los Angeles, California 90095-1567, USA
- ⁵Nevada Bureau of Mines and Geology, University of Nevada, Reno, Nevada 89557, USA
- Department of Earth and Ocean Sciences, University of North Carolina Wilmington, Wilmington, North Carolina 28403, USA

ABSTRACT

High-pressure metamorphic rocks occur as distinct belts along subduction zones and collisional orogens or as isolated blocks within orogens or mélanges and represent continental materials that were subducted to deep depths and subsequently exhumed to the shallow crust. Understanding the burial and exhumation processes and the sizes and shapes of the high-pressure blocks is important for providing insight into global geodynamics and plate tectonic processes. The South Beishan orogen of northwestern China is notable for the exposure of early Paleozoic high-pressure (HP), eclogite-facies metamorphic rocks, yet the tectonism associated with the HP metamorphism and mechanism of exhumation are poorly understood despite being key to understanding the tectonic evolution of the larger Central Asian Orogenic System. To address this issue, we examined the geometries, kinematics, and overprinting relationships of structures and determined the temperatures and timings of deformation and metamorphism of the HP rocks of the South Beishan orogen. Geochronological results show that the South Beishan orogen contains ca-1.55-1.35 Ga basement metamorphic rocks and ca. 970-866 Ma granitoids generated during a regional tectono-magmatic event. Ca. 500-450 Ma crustal thickening and HP metamorphism may have been related to regional contraction in the South Beishan orogen. Ca. 900–800 Ma protoliths experienced eclogite-facies metamorphism (~1.2-2.1 GPa and ~700-800 °C) in thickened lower crust. These HP rocks were subsequently exhumed after ca. 450 Ma to mid-crustal depths in the footwall of a regional detachment fault during southeast-northwest-oriented crustal extension, possibly as the result of rollback of a subducted oceanic slab. Prior to ca. 438 Ma, north-south-oriented contraction resulted in isoclinal folding of the detachment fault and HP rocks. Following this contractional phase in the middle Mesozoic, the South Beishan orogen experienced thrusting interpreted to be the response to the closure of the Tethyan and Paleo-Asian Ocean domains. This contractional phase was followed by late Mesozoic extension and subsequent surface erosion that controlled exhumation of the HP rocks.

Chen Wu https://orcid.org/0000-0003-0647-3530

■ INTRODUCTION

Surface exhumation of high-pressure (HP) metamorphic rocks from deep depths is an important and much-debated process with broad implications for tectonics (Fig. 1) (e.g., Avigad and Garfunkel, 1991; Nie et al., 1994; Chatzaras et al., 2006; Bond et al., 2007; Yin et al., 2007; Guillot et al., 2009; Hacker et al., 2013; Erdman and Lee, 2014; Marques et al., 2018). Global HP terranes are classified as either oceanic or continental type based on their lithologic assemblages and tectonic settings (Burov et al., 2014; Baziotis et al., 2019; Wang et al., 2019). Unravelling the tectono-metamorphic histories of these terranes is fundamental to understanding the processes of lithospheric deformation and interactions with the asthenosphere and to providing constraints on the formation and exhumation of HP rocks (Nie et al., 1994; Eide, 1995; Chemenda et al., 1996; Lardeaux et al., 2001; Guillot et al., 2009). Determination of the mechanisms of HP metamorphism in continental crust requires knowledge of the tectonic setting in which metamorphism occurs (Guillot et al., 2009; Zhang and Wang, 2020).

The Central Asian Orogenic System (Figs. 2A and 2B) (Briggs et al., 2007, 2009; Wu et al., 2016a; Zuza and Yin, 2017), also known as the Altai orogenic system (Şengör, 1984; Şengör et al., 1993), the Central Asia fold belt (Zonenshain et al., 1990), and the Central Asian Orogenic Belt (Şengör, 1984; Jahn et al., 2000; Windley et al., 2007; Xiao et al., 2015; Windley and Xiao, 2018; Chen et al., 2022), is the largest Phanerozoic accretionary orogen on Earth and contains widespread HP metamorphic rocks (e.g., Tagiri et al., 1995; Shatsky et al., 1996; Beane and Connelly, 2000; Buslov et al., 2002; Parkinson et al., 2002; Gao and Klemd, 2003; Dobretsov and Buslov, 2004; Ota et al., 2007; Togonbaeva et al., 2009; Saktura et al., 2017; Liu et al., 2019; Meng et al., 2020). Despite the regional prominence of the HP metamorphic rocks as part of the Central Asian Orogenic System, how the HP rocks formed and were exhumed remain uncertain (Warren, 2013; Zhang and Wang, 2020), which has impeded our understanding of the larger tectonic evolution of Eurasia.

Over the past several decades, two classes of tectonic models have been developed to explain the formation and exhumation of the HP rocks in the

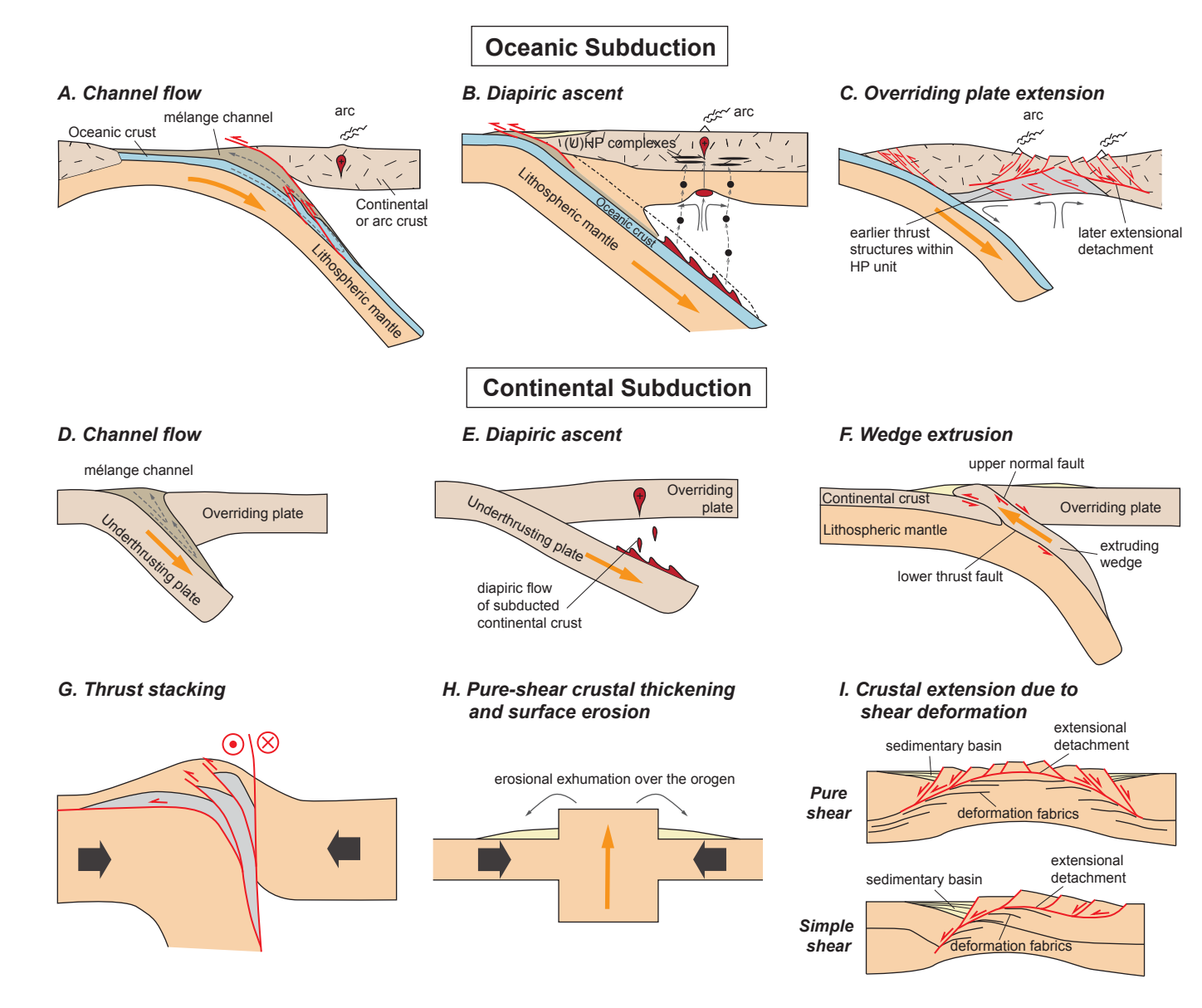


Figure 1. Tectonic models of exhumation processes for high-pressure (HP) metamorphic rocks. (A) Channel flow during oceanic subduction (Jin et al., 2021). (B) Diapiric ascent of subducted oceanic materials during subduction (Yin et al., 2007). (U)HP—(ultra)high-pressure. (C) Overriding plate extension and thinning during oceanic subduction (Jolivet et al., 1994; Brun and Faccenna, 2008; Malusà et al., 2011). (D) Channel flow during continental subduction (Mancktelow, 1995; Jolivet et al., 2005). (E) Diapiric ascent of subducted continental materials (Hacker et al., 2005). (F) Wedge extrusion during continental subduction (Chemenda et al., 1995, 1996, 1997). (G) Thrust stacking during continental collision (Okay and Şengör, 1992; Nie et al., 1994). (H) Pure-shear crustal thickening during continental collision (Dewey et al., 1993). (I) Crustal extension due to shear deformation during orogen collapse (Avigad and Garfunkel, 1991; Fassoulas et al., 1994; Bond et al., 2007).

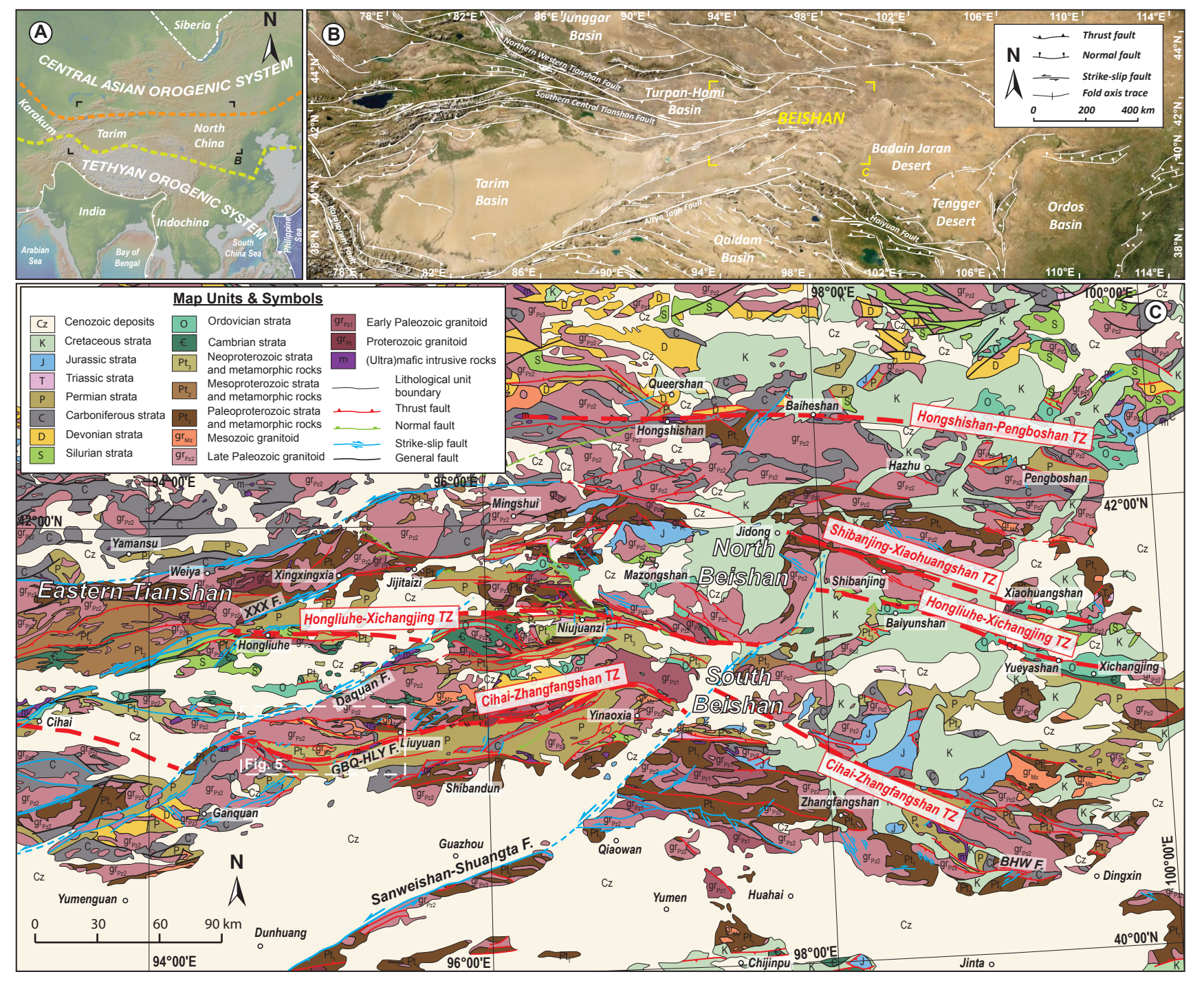


Figure 2. (A) Tectonic map of central Asia showing Tethyan Orogenic System and Central Asian Orogenic System. (B) Tectonic map of Tarim–North China craton showing major thrust systems (Yin and Harrison, 2000; Yin, 2010; Ding et al., 2020; Shi et al., 2020; Wu et al., 2020). (C) Geologic map of Beishan region based on Gansu BGMR (1989) and our structural observations. Abbreviations: XXX F.—Xingxingxia fault; GBO-HLY F.—Gubaoquan-Hongliuyuan fault; BHW F.—Beihewan fault; TZ—tectonic zone.

Central Asian Orogenic System (Fig. 1): (1) the oceanic subduction models (i.e., Pacific type) that involve HP metamorphism during oceanic subduction and arc magmatism, and subsequent exhumation (Yin et al., 2007; Agard et al., 2009; Nielsen and Marschall, 2017; Jin et al., 2021); and (2) the continental subduction models (i.e., Himalayan type) that involve formation and exhumation of HP metamorphic rocks during continent-continent collision and orogenic collapse (Nie et al., 1994; Davies and von Blanckenburg, 1995; Chemenda et al., 1996; Liou et al., 2004; Osozawa and Pavlis, 2007; Wang et al., 2014a, 2018a; Osozawa and Wakabayashi, 2015; Long et al., 2020; Feng et al., 2021). The oceanic subduction model is based on the occurrence of HP metamorphic rocks in oceanic subduction zones and the resemblance of their protoliths to oceanic lithosphere (e.g., England and Holland, 1979; Kurz et al., 1998; Malatesta et al., 2012; Starr et al., 2020). The oceanic subduction model is further divided into three sub-models based on the predicted geological processes and related deformation style: (1) channel flow during oceanic subduction (Fig. 1A) (e.g., Li et al., 2011a; Marques et al., 2018; Schwarzenbach et al., 2021); (2) diapiric ascent of subducted oceanic materials during subduction (Fig. 1B) (e.g., Yin et al., 2007); and (3) overriding plate extension due to rollback of subducted oceanic slab or mantle wedge flow (Fig. 1C) (e.g., Platt, 1986; Jolivet et al., 1994; Husson et al., 2009). The continental subduction model is based on the occurrence of HP metamorphic rocks with oceanic subduction characteristics within collisional orogens (e.g., Okay and Şengör, 1992; Nie et al., 1994). The continental subduction model is further divided into several sub-models according to different continental subduction-collision processes: (1) channel flow during continental subduction (Fig. 1D) (e.g., Mancktelow, 1995; Boutelier et al., 2004); (2) diapiric ascent of subducted continental materials during continental subduction (Fig. 1E) (e.g., Hacker et al., 2005; Erdman and Lee, 2014); (3) wedge extrusion induced by upward motion of the subducted crustal body (Fig. 1F) (e.g., Ernst and Liou, 1995; Davies and von Blanckenburg, 1995; Chemenda et al., 1995, 1996, 1997); (4) intracontinental thrust stacking (Fig. 1G) (e.g., Okay and Sengör, 1992; Nie et al., 1994); (5) pure-shear crustal thickening and coeval surface erosion during continental collision (Fig. 1H) (e.g., Dewey et al., 1993; Gilotti and Krogh Ravna, 2002); and (6) crustal extension due to shear deformation during orogen collapse (Fig. 11) (e.g., Avigad and Garfunkel, 1991; Fassoulas et al., 1994; Bond et al., 2007).

These two end-member models make specific predictions regarding the temporal and spatial relationships between HP metamorphism and arc magmatism, types of metamorphic rock assemblages and their protoliths, timing between peak metamorphism and protolith formation, pressure-temperature (*P-T*) paths, exhumation mechanisms and rates, and modes and kinematic histories of deformation associated with pro- and retrograde metamorphism (Table 1) (Cloos and Shreve, 1988; Okay and Şengör, 1992; Mancktelow, 1995; Ernst, 1999; Kurz and Froitzheim, 2002; Yin et al., 2007; Guillot et al., 2009; Song et al., 2015; Zhang and Wang, 2020). For example, the oceanic subduction model predicts coeval arc magmatism and HP metamorphism and a <200 m.y. interval between protolith formation and peak metamorphism (Song et al., 2015).

To test the predictions of the oceanic and continental subduction models, we collected field-based and microstructural observations and geo- and thermochronological data from the South Beishan orogen, which is south of the Hongliuhe-Xichangjing tectonic zone, located along the central-southern margin of the Central Asian Orogenic System (Fig. 2C). We focused our investigation on the HP rocks of the South Beishan orogen to constrain their tectonic setting, exhumation mechanism, and time scales to better understand the tectonic evolution of the Central Asian Orogenic System and thus assembly of the Eurasian continent.

■ GEOLOGICAL SETTING

Beishan Orogen

The Beishan region of central Asia is located within northwestern China and encompasses parts of the Xinjiang Uygur Autonomous Region, Gansu Province, and Inner Mongolia Autonomous Region (Fig. 2B). The east-westtrending Beishan orogen is located along the central-southern margin of the Central Asian Orogenic System and contains several Paleozoic tectonic zones that, from north to south, include the Hongshishan-Pengboshan, Shibanjing-Xiaohuangshan, Hongliuhe-Xichangjing, and Cihai-Zhangfangshan tectonic zones (Fig. 2C) (Hsü and Chen, 1999; Xiao et al., 2010). The Mesozoic tectonic history of the Beishan orogen is poorly understood. In addition, the spatial and temporal relationships between reported contractional and extensional deformation in the Beishan region and adjacent areas of North China, Mongolia, Tianshan, and Qilianshan are uncertain (Zheng et al., 1996; Webb et al., 1999; Dumitru and Hendrix, 2001; Graham et al., 2001; Johnson et al., 2001; Vincent and Allen, 2001; Davis et al., 2002; Briggs et al., 2007, 2009; Wu et al., 2016b, 2022a, 2022b; Zuza et al., 2018; Wang et al., 2022). The Beishan orogen is cut by several Cenozoic left-slip faults related to the Altyn Tagh fault along the northern margin of the Tibetan Plateau (Guo et al., 2008) (Fig. 2). A few studies show that Cenozoic deformation initiated in the Pliocene with slip along the Daguan fault zone (Fig. 2C) and progressively propagated eastward to the southeastern Beishan region during the late Quaternary (Guo et al., 2008; Yang et al., 2019; Yun et al., 2021).

The prominent tectonic event recorded in the Beishan orogen involved the creation and subsequent destruction of the Paleo-Asian Ocean from the late Proterozoic to the latest Paleozoic, which led to the formation of the Central Asian Orogenic System (Şengör, 1984; Zonenshain et al., 1990; Şengör et al., 1993, 2018; Liu and Wang, 1995; Jahn et al., 2000; Heubeck, 2001; Windley et al., 2007; Xiao et al., 2009, 2010, 2014; Wilhem et al., 2012; Liu et al., 2017; Yakubchuk, 2017; Chen et al., 2022). Evidence of Neoproterozoic to latest Paleozoic tectonism in the Beishan orogen includes widespread occurrence of Paleozoic arc-related rocks, fault-bounded zones of (ultra)mafic rocks, and deformation of Neoproterozoic–Permian strata (Fig. 2C) (Xiao et al., 2010; Zhang and Cunningham, 2012; Song et al., 2014; Tian et al., 2014a, 2021; Cleven et al., 2018; Shi et al.,

TABLE 1. PREDICTIONS OF MAJOR TECTONIC MODELS FOR HIGH-PRESSURE (HP) METAMORPHIC ROCKS EXHUMATION PROCESSES

Prediction	Temporal relation to magmatism	Style of exhumation	Tectonic setting	Pressure-temperature (P-T) paths	Protolith of HP rocks	Interval between protolith and peak metamorphism age	Residence time in the lower crust	Deformation style and history	References
Channel flow Opportunity Oppo	Syn-arc magmatism	Localized exhumation in accretionary complexes at a rate of tens of centimeters per year from deep to lower- crust level	Active oceanic convergent margins	Uniform <i>P-T</i> path; most peak conditions, <550 °C, 1.5–2.5 GPa	Oceanic and continental materials	No more than 200 m.y.	A few million years	(1) Presence of poorly deformed lenses (from meter- to kilometer-scale) of heterogeneous lithologies inside highly sheared serpentinite and metasediments country-rocks, (2) strong strain partitioning, (3) tectonic mixing resulting in heterogeneous metamorphic peak conditions of different lenses	England and Holland, 1979; Gerya et al., 2002; Agard et al., 2009; Li et al., 2011a; Malatesta et al., 2012; Erdman and Lee, 2014; Marques et al., 2018; Starr et al., 2020; Jin et al., 2021; Schwarzenbach et al., 2021
Diapiric ascent O Overriding plate	Syn-arc magmatism	No exhumation required during HP metamorphism	Active oceanic convergent margins	Diverse P-T path	Oceanic and continental materials	No more than 200 m.y.	Tens of millions of years	HP rocks as xenoliths occur within magmatic arcs	Yin et al., 2007
S Overriding plate extension	Syn–arc magmatism	Coherent uplift exhumation in the overriding plate or subduction zone	Active oceanic convergent margins	Uniform <i>P-T</i> path; most peak conditions, <550 °C, 1.5–2.5 GPa	Oceanic and continental materials	No more than 200 m.y.	Tens of millions of years	(1) HP rocks within the arc or back-arc belt, (2) normal-sense fault emplacing HP rocks in contact with supracrustal rocks, (3) later detachment fault cutting across the earlier thrust structures	Platt, 1986; Jolivet et al., 1994; Krohe and Mposkos, 2002; Brun and Faccenna, 2008; Husson et al., 2009; Malusà et al., 2011; Liang et al., 2017; Lian et al., 2018
Channel flow	Post–arc magmatism	Localized along sutures; 5–10 cm/yr	Collisional orogens	Uniform P-T path; most peak conditions, >600 °C	Continental protoliths	No definite age range	A few million years	Ductile deformation associated with tectonic mixing	Mancktelow, 1995; Boutelier et al., 2004; Jolivet et al., 2005
Diapiric ascent	Post–arc magmatism	No exhumation required during HP metamorphism	Collisional orogens	Diverse P-T path due to different diapir sizes and thermal structures	Continental protoliths	No definite age range	Tens of millions of years	HP rocks intrude into lower and middle crustal rocks mostly as xenoliths	Hacker et al., 2005; Erdman and Lee, 2014
Wedge extrusion	Post–arc magmatism and syn– to post–collisional magmatism	Localized exhumation along the extrusion wedge	Collisional orogens	Uniform <i>P-T</i> path; most peak conditions, >600 °C	Continental protoliths	No definite age range	A few million years	(1) Coeval thrust-type and normal-sense faults and/or shear zones in the downgoing continental crust, (2) at the stage of deep subduction, associated with a major thrust fault, and at the exhumation stage, with a major normal fault corresponding to the upper surface of the rising crustal or sedimentary body	Chemenda et al., 1995, 1996, 1997; Davies and von Blanckenburg, 1995; Ernst and Liou, 1995; Chatzaras et al., 2006; Ring et al., 2007; Butler et al., 2013
Thrust stacking Outin	Post–arc magmatism	Main exhumation in overriding thrust plates	Collisional orogens	Uniform <i>P-T</i> path; most peak conditions, >600 °C	Continental protoliths	No definite age range	A few million years to ~10 m.y. for plate-tectonic rate of thrusting	(1) Crustal thickening via thrusting or stacking of crustal wedges, (2) coherent crustal section with HP rocks thrusting over low-grade rocks	Okay and Şengör, 1992; Nie et al., 1994; Eide, 1995
Pure-shear thickening	Post–arc magmatism	Exhumation within collisional orogens	Collisional orogens	Uniform P-T path; most peak conditions, >600 °C	Continental protoliths	No definite age range	A few million years to ~10 m.y. for plate tectonic rate of convergence	Distributed crustal shortening	Dewey et al., 1993; Gilotti and Krogh Ravna, 2002
Crustal extension due to pure shear	Post–arc magmatism	Crust thinning due to pure shear and uplift due to isostasy	Post-collisional orogens	Uniform P-T path; most peak conditions, >600 °C	Continental protoliths	No definite age range	Tens of millions of years	(1) HP rocks in direct normal-fault contact with low-grade rocks, (2) bulk coaxial deformation	Fassoulas et al., 1994; Bond et al., 2007
Crustal extension due to simple shear	Post–arc magmatism	Crust thinning due to simple shear and uplift due to isostasy	Post-collisional orogens	Uniform P-T path; most peak conditions, >600 °C	Continental protoliths	No definite age range	Tens of millions of years	(1) HP rocks in direct normal-fault contact with low-grade rocks, (2) asymmetrical shearing deformation	Avigad and Garfunkel, 1991

104

2018a; Zheng et al., 2018; Li et al., 2020; Soldner et al., 2020a; Wang et al., 2021; Li et al., 2022). The (ultra)mafic rocks are distributed within several tectonic zones including the Hongshishan-Pengboshan (ca. 347–342 Ma; e.g., Wang et al., 2014b; Niu et al., 2020a; Zhang et al., 2020), Shibanjing-Xiaohuangshan (ca. 516–453 Ma; e.g., Chen et al., 2017; Shi et al., 2018a; Meng et al., 2021), Hongliuhe-Xichangjing (ca. 528–405 Ma; e.g., Zhang and Guo, 2008, Hou et al., 2012; Wu et al., 2012; Tian et al., 2014a; Cleven et al., 2015; Hu et al., 2015; Sun et al., 2017; Shi et al., 2018a; Wang et al., 2018b), and Cihai-Zhangfangshan (ca. 307–268 Ma; e.g., Zhang et al., 2011; Mao et al., 2012b; Chen et al., 2013; Xu et al., 2019; Wang et al., 2020b) tectonic zones (Fig. 2C).

The HP metamorphic rocks of the South Beishan orogen, located south of the Hongliuhe-Xichangjing suture, are ideal assemblages for investigating the tectonic evolution of the Central Asian Orogenic System and their exhumation mechanism (e.g., Liu et al., 2011; Qu et al., 2011; Saktura et al., 2017; Soldner et al., 2020b). The South Beishan orogen consists of Paleo- to Mesoproterozoic basement overlain by a Meso- to Neoproterozoic cover sequence (Fig. 3) (Gansu BGMR, 1997; Shaanxi IGS, 2014). Basement intrusions have ca. 1.5–1.4 Ga magmatic zircon ages and ca. 1.7-1.5 Ga zircon Hf model ages, which are similar to ages recorded in the North China craton (He et al., 2015; Yuan et al., 2019). The opening of the Beishan Ocean along the Hongliuhe-Niujuanzi-Xichangiing suture during the Neoproterozoic is evidenced by widespread Neoproterozoic-early Paleozoic passive-margin strata (Fig. 2C) (Gansu BGMR, 1989, 1996). The discontinuously exposed Hongliuhe-Niujuanzi-Xichangjing suture zone consists of early Paleozoic ophiolite complexes and volcanic arc rocks (e.g., Tian et al., 2014a; Cleven et al., 2015; Hu et al., 2015; Shi et al., 2018a; Wang et al., 2020a). Abundant early Paleozoic arc-magmatic rocks intrude Precambrian basement rocks and overlying sedimentary strata and have been interpreted to be related to southward subduction of Paleo-Asian oceanic lithosphere (Fig. 2C) (e.g., Li et al., 2009, 2011b; Mao et al., 2012a; Niu et al., 2020b; Zhao et al., 2020; Sun et al., 2021; Li et al., 2022). The Carboniferous-Permian opening of the Liuyuan Ocean along the Cihai-Liuyuan-Zhangfangshan tectonic zone is evidenced by rift-related deposits and ca. 307-268 Ma bimodal volcanic and intrusive rocks (Figs. 2C and 3) (e.g., Gao et al., 2018a, 2018b; Niu et al., 2018a, 2018b, 2021; Gao et al., 2020; Zheng et al., 2021). After the Jurassic, both the North and South Beishan orogens experienced intracontinental deformation, evidenced by strongly deformed Jurassic strata. This deformation event has been attributed to final closure of the Paleo-Asian Ocean tectonic domain in the north and closure of the Tethyan tectonic domain in the south (e.g., Zuo et al., 1991; Zheng et al., 1996; Yin and Harrison, 2000; Zhang and Cunningham, 2012; Zuza and Yin, 2017).

High-Pressure Eclogite-Facies Metamorphism in the Beishan Orogen

Studies focused on the HP rocks of the South Beishan orogen near Liuyuan town (Fig. 2C) have presented several models to explain the metamorphism and exhumation of eclogite and the multi-stage tectonic evolution of the orogen

(Fig. 4) (Mei et al., 1999a; Yang et al., 2006; Liu et al., 2011; Qu et al., 2011; Soldner et al., 2020b). Whereas few thermochronologic studies have provided age constraints on the exhumation of the HP rocks (Qu et al., 2011; Gillespie et al., 2017), a coherent tectonic model for the emplacement and exhumation of these rocks is not yet available given the scarcity of ages and lack of structural observations. Two hypotheses have been proposed to explain the exhumation of the HP rocks of the South Beishan orogen to the shallow crust (Fig. 4). One model involves Middle Ordovician-early Permian northward subduction of the Paleo-Asian oceanic slab to eclogite-facies depths (Xiao et al., 2010; Qu et al., 2011) (Fig. 4A). Alternatively, Liu et al. (2011) suggested that the formation of eclogite during subduction occurred in the Middle Ordovician-Silurian (Fig. 4B). The second hypothesis involves northward subduction of the Dunhuang continental block beneath the Huaniushan-Shuangyingshan continental block (Saktura et al., 2017; Soldner et al., 2020b) (Figs. 4C and 4D). In this model, Saktura et al. (2017) suggested that crustal thickening caused by continentcontinent collision prompted eclogite-facies metamorphism of mafic dikes and/or sills that intruded granitic gneiss (Fig. 4C). Alternatively, Soldner et al. (2020b) argued that eclogitized basaltic lower crust was underplated beneath overriding continental crust ca. 890-870 Ma (Soldner et al., 2020a) and was subsequently emplaced adjacent to granitic gneiss via two-stage folding and contraction-related mixing (Fig. 4D).

The Liuyuan metamorphic complex of the South Beishan orogen (Fig. 5) contains Precambrian metamorphic rocks (Xiao et al., 2010; Liu et al., 2015) and early Paleozoic HP eclogite (Mei et al., 1999a; Qu et al., 2011). The occurrence of HP rocks in the South Beishan orogen invokes two important questions regarding its tectonic evolution: (1) What is the tectonic setting for the HP metamorphism?; and (2) When and how were these rocks exhumed? In the Geological Setting section, we summarize existing constraints on the HP and surrounding rocks.

Lithology

The Gubaoquan area exposes high- and low-grade metamorphic rocks that include Neoproterozoic mylonitic granitoid and HP rocks intruded by Silurian and Permian granitoids (Mei et al., 1999a, 1999b; Yu et al., 1999; Liu et al., 2002; Yang et al., 2006). Unmetamorphosed rocks consist of early Permian riftbasin sedimentary and volcanic rocks (i.e., basalt, sandstone, and shale) and Cenozoic fluvial sedimentary rocks (Fig. 5) (Chen et al., 2016; Niu et al., 2021).

In the Gubaoquan area, metamorphic rocks are divided into a HP metamorphic unit and its wall-rock unit. Mylonitic granitoid of the wall-rock unit and eclogite-bearing HP rocks are referred to as the Huaniushan Group, which has been associated with Paleozoic oceanic subduction (Mao et al., 2012b). Other researchers have designated the mylonitic wall-rock granitoids and eclogite-bearing HP unit as the Neoarchean–Paleoproterozoic Dunhuang Group, which has been interpreted to represent basement rocks of the Beishan orogen (Gansu BGMR, 1989). However, recent geochronology results show that the crystallization age of mylonitic granitoid and protolith ages of the HP

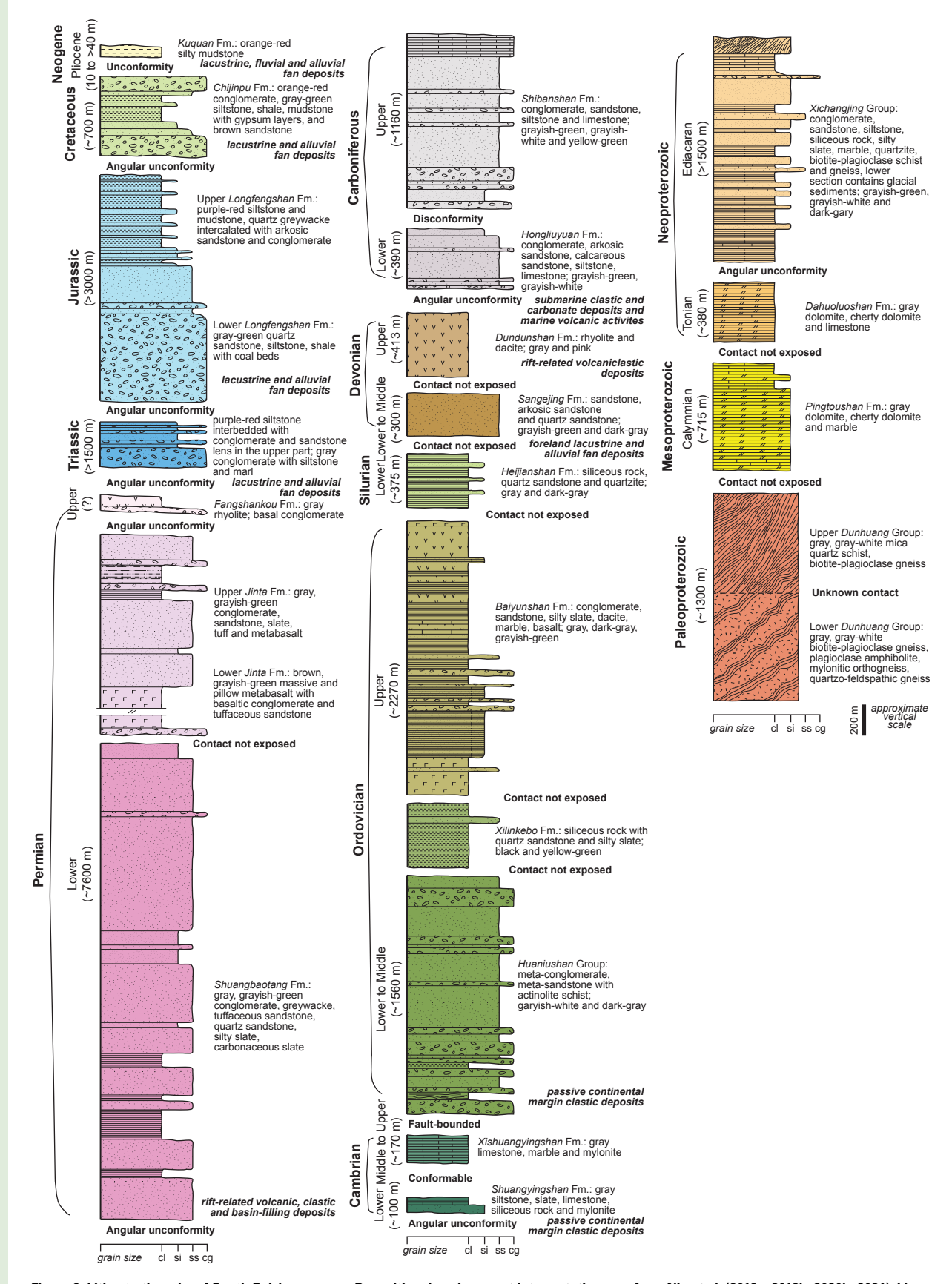


Figure 3. Lithostratigraphy of South Beishan orogen. Depositional environment interpretations are from Niu et al. (2018a, 2018b, 2020b, 2021), Liang et al. (2020), Chen et al. (2017), and Zuo et al. (1987, 1995). Note that colors do not strictly correspond to those in Figure 2C and bold italic text refers to unit above. Abbreviations: cl—clay; si—silt; ss—sandstone; cg—conglomerate.

Models of Metamorphism and Exhumation of the South Beishan HP Rocks

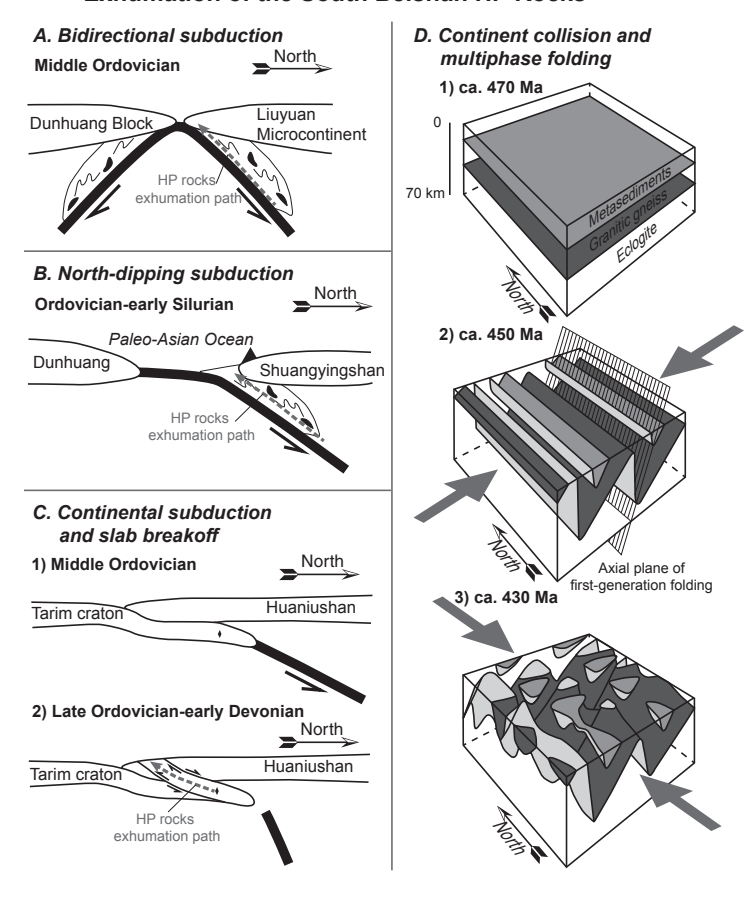


Figure 4. Models of metamorphism and exhumation of South Beishan high-pressure (HP) rocks. (A) Oceanic crust channel flow with bidirectional subduction (Liu et al., 2011). (B) Oceanic crust channel flow with north-dipping subduction until early Permian (Qu et al., 2011). (C) Wedge extrusion of partially subducted continental crust due to slab breakoff (Saktura et al., 2017). (D) Continental thickening and contraction-related mixing as a result of two-stage folding (Soldner et al., 2020b).

metamorphic unit are early Neoproterozoic (ca. 933–868 Ma) (Liu et al., 2011; Ye et al., 2013; Liu et al., 2015; Yuan et al., 2015; Wang et al., 2017; Zong et al., 2017; Soldner et al., 2020a).

Pressure-Temperature-Time Paths

Previously published P-T paths of the Gubaoquan HP rocks exhibit clockwise paths of isothermal decompression (Mei et al., 1999a; Yu et al., 1999; Liu et al., 2002; Qu et al., 2011; Soldner et al., 2020b), similar to those of HP rocks of the Sulu-Dabie, Alpine, and Norwegian ultrahigh-pressure (UHP) terranes (Chopin, 1984; Smith, 1984; Wang and Cong, 1999). Mei et al. (1999a) first reported the presence of eclogite in augen granitic gneiss in the Liuyuan area and constrained peak HP pressures of ~1.6–1.8 GPa and temperatures of ~700–800 °C. These P-T results are supported by later results presented by Liu et al. (2002), Qu et al. (2011), and Soldner et al. (2020b), who demonstrated that the eclogite blocks experienced peak pressures of ~1.2-2.1 GPa and temperatures of ~700-800 °C, without evidence of UHP metamorphism as postulated by Yu et al. (1999). The retrograde assemblage of the eclogite developed at pressures of ~0.6-1.2 GPa and temperatures of ~620-750 °C (Liu et al., 2002; Qu et al., 2011; Soldner et al., 2020b). The P-T data of Mei et al. (1999a), Yu et al. (1999), Liu et al. (2002), Qu et al. (2011), and Soldner et al. (2020b) also show decompression paths with constant or slightly decreasing temperature following peak pressure.

Geo- and Thermochronology

The protolith ages of eclogites determined from zircon grain core analyses are ca. 889–819 Ma and 1007 \pm 20 Ma (Yang et al., 2006; Liu et al., 2011; Qu et al., 2011; Soldner et al., 2020a). These eclogites subsequently experienced peak metamorphism ca. 467–465 Ma (Liu et al., 2011; Qu et al., 2011; Soldner et al., 2020b). Soldner et al. (2020b) obtained garnet Lu-Hf and Sm-Nd ages of 462.0 \pm 6.2 Ma and 452.8 \pm 3.0 Ma for eclogite and interpreted the ages to represent the timing of garnet crystallization during prograde and eclogite-facies peak metamorphism, respectively. Granitic gneiss has a protolith age of 920 \pm 14 Ma (Saktura et al., 2017) and a younger 40 Ar/ 39 Ar cooling age of 428.9 \pm 3.8 Ma, the latter interpreted to reflect the timing of exhumation (Qu et al., 2011). Gillespie et al. (2017) reported an apatite fission-track age of 125.4 \pm 9.9 Ma for granitic gneiss that was interpreted to be related to collision of the peri-Gondwanan Lhasa block with southern Eurasia or the contemporaneous Mongol-Okhotsk collisional event.

Protolith of the HP (Ultra)mafic Rocks

The protolith of the HP eclogite blocks exposed in the South Beishan orogen near Liuyuan could represent fragments of oceanic crust that were generated

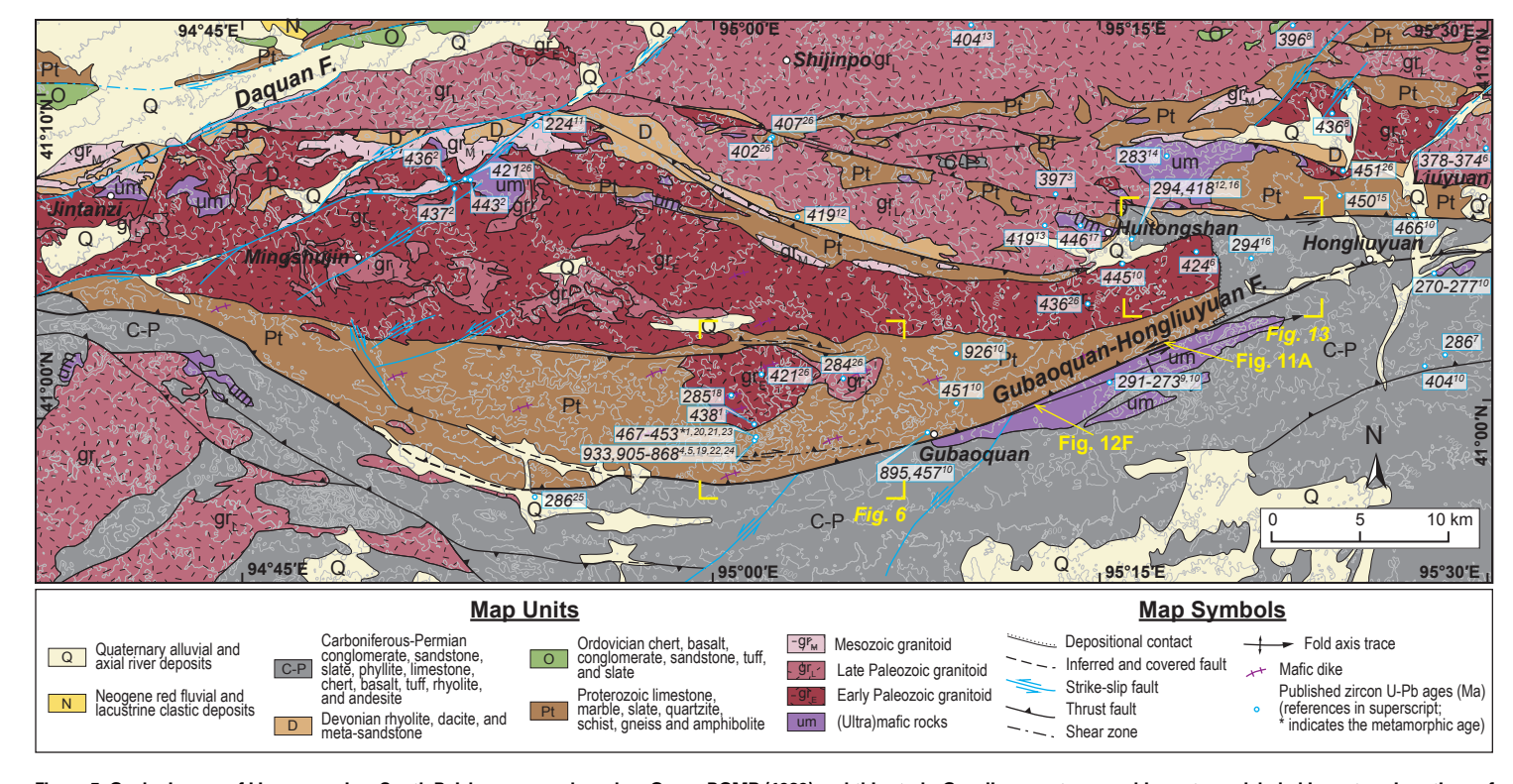


Figure 5. Geologic map of Liuyuan region, South Beishan orogen, based on Gansu BGMR (1989) and this study. Gray lines are topographic contours, labeled in meters. Locations of Figures 6, 11A, 12F, and 13 are shown. F—fault. Age sources: 1—Liu et al. (2011); 2—Li et al. (2015); 3—Li et al. (2011b); 4—Yuan et al. (2015); 5—Liu et al. (2015); 6—Mao et al. (2012a); 7—Mao et al. (2012b); 8—Zhao et al. (2007); 9—Zhang et al. (2011); 10—Wang et al. (2017); 11—Li et al. (2012); 12—Niu et al. (2020b); 13—Zhu et al. (2016); 14—Zhang (2014); 15—Cleven et al. (2018); 16—Niu et al. (2018a); 17—Yu et al. (2012); 18—Gao et al. (2020); 19—Soldner et al. (2020a); 20—Soldner et al. (2020b); 21—Qu et al. (2011); 22—Zong et al. (2017); 23—Saktura et al. (2017); 24—Ye et al. (2013); 25—Niu et al. (2018b); 26—Li et al. (2022).

along a mid-ocean ridge or seamount (Qu et al., 2011), mafic igneous rocks emplaced as dike swarms (Saktura et al., 2017), or older eclogitized lower crust (Soldner et al., 2020a, 2020b). The geochemical composition of eclogitic blocks shows typical enriched and normal mid-ocean-ridge basalt (E-MORB and N-MORB) signatures, which have been interpreted to reflect a subducted seamount and oceanic crust protolith (Qu et al., 2011). In contrast, a continental origin (Saktura et al., 2017; Soldner et al., 2020b) for the Gubaoquan eclogite has been proposed due to the Neoproterozoic protolith ages ranging from ca. 890 to 860 Ma (Liu et al., 2011; Qu et al., 2011; Saktura et al., 2017) and enigmatic geochemical compositions (Saktura et al., 2017). Eclogite and amphibolite blocks are entrained in a metasedimentary matrix formed by garnet-mica schist and meta-graywacke without the occurrence of ultramafic rocks or serpentinite, which may indicate a continental origin.

METHODS

To answer above-mentioned questions, we conducted geological mapping of the South Beishan HP rocks exposed near Liuyuan town (Fig. 5). Mapping was performed in the Gubaoquan area, which contains exposures of the HP rocks and strongly folded Carboniferous–Permian strata of the Huitongshan-Hongliuyuan area. In this study, we collected field and microstructural observations and geo- and thermochronological data from the HP rocks of the South Beishan orogen in the Gubaoquan and Huitongshan-Hongliuyuan areas (Fig. 5). Based on previous geological mapping, we focused our efforts on three key exposures: (1) HP eclogite; (2) strongly folded, Carboniferous–Permian strata; and (3) the Gubaoquan-Hongliuyuan fault zone. A total of 25 samples were collected for electron backscatter diffraction (EBSD) analysis,

TABLE 2. SUMMARY OF SAMPLE LOCATIONS AND ZIRCON GEOCHRONOLOGY RESULTS IN THE SOUTH BEISHAN REGION

Sample number	Rock type	Latitude (°N)	Longitude (°E)	Elevation (m)	Interpreted age (Ma)	MSWD	n	Method
LJ2020-45	Sandstone	41°04′54.04″	95°20′22.13″	1817	N.A.	N.A.	N.A.	Apatite (U-Th)/He
LJ2020-38	Monzogranite	41°01′10.79″	95°02′02.11"	1805	N.A.	N.A.	N.A.	Apatite (U-Th)/He
LJ2020-39	Mylonitic garnet amphibolite	40°59′50.54"	95°02′22.91″	1772	500.0 ± 3.4	0.91	16 out of 30	U-Pb zircon
LJ2020-40	Mylonitic garnet-bearing biotite gneiss	40°59′50.54"	95°02′22.91″	1772	512.1 ± 4.3	1.7	19 out of 30	U-Pb zircon, apatite (U-Th)/He
LJ2020-3	Mylonitic mica schist	40°59′41.55″	95°02′25.82″	1764	N.A.	N.A.	N.A.	EBSD
LJ2020-8	Granitic dike	40°59'41.55"	95°02′25.82″	1764	410 ± 16	4.8	5 out of 25	U-Pb zircon
LJ2020-33	Mylonitic granitoid	40°59′40.36″	95°04′53.86″	1763	1004 ± 29	2.3	8 out of 30	U-Pb zircon
LY1908-10	Mylonitic granitic gneiss	40°59'26.79"	95°02′16.22″	1794	N.A.	N.A.	N.A.	EBSD
LY1908-21	Mylonitic granitic gneiss	40°59'23.24"	95°02′17.32″	1777	N.A.	N.A.	N.A.	EBSD
LY1908-16	Mylonite	40°59'23.10"	95°02′14.46″	1766	N.A.	N.A.	N.A.	EBSD
LY1908-17-1	Mylonitic garnet-bearing plagioclase gneiss	40°59'22.69"	95°02′14.57"	1765	920 ± 11	5.3	32 out of 40	U-Pb zircon
LY1908-18	Mylonitic garnet-bearing plagioclase gneiss	40°59'22.69"	95°02′14.57"	1765	N.A.	N.A.	N.A.	EBSD
LY1908-26	Mylonitic plagioclase gneiss	40°59'21.46"	95°02′18.10″	1764	880.3 ± 5.7	1.2	24 out of 24	U-Pb zircon
LY1908-39	Eclogite	40°59′15.99″	95°02′19.89″	1748	N.A.	N.A.	N.A.	Apatite (U-Th)/He
LY1908-47	Mylonitic plagioclase gneiss	40°59′13.78″	95°02′18.72″	1747	N.A.	N.A.	N.A.	EBSD
LJ2020-32	Granitic dike	40°59'08.36"	95°04′27.25″	1752	887.9 ± 6.7	1.5	20 out of 25	U-Pb zircon
LJ2020-31	Mylonitic granitic dike	40°59'06.95"	95°04′23.54"	1756	943 ± 13	5.9	18 out of 30	EBSD, U-Pb zircon
LY1908-52	Felsic mylonite	40°59′04.73″	95°02′21.65″	1750	N.A.	N.A.	N.A.	EBSD
LY1908-93	Mylonitic granitoid	40°58′59.45"	95°03′57.66″	1750	915.3 ± 5.9	1.6	25 out of 25	U-Pb zircon
LY1908-60	Mylonitic granitoid	40°58′41.74″	95°02′26.80″	1730	N.A.	N.A.	N.A.	EBSD

Note: MSWD—mean square of weighted deviates; N.A.—not available; EBSD—electron backscatter diffraction, which can analyze the microtextures of mineral grains; n—number of selective zircon grains for weighted mean age: the values after "±" symbol in the interpreted age column represent the uncertainties of 1σ of the weighted ages.

> zircon U-Pb geochronology, and apatite (U-Th)/He thermochronology. Sampling locations are listed in Table 2 and detailed methodologies are described in the Methods section.

Microstructure and EBSD Analyses

Oriented samples were collected for microstructural and EBSD analyses to determine their mineralogy and their deformation mechanisms, temperatures, and kinematics. Semiquantitative deformation temperatures were obtained from petrographic analysis. EBSD analyses were performed to constrain quartz slip mechanisms, which vary as a function of primary temperature, water content, strain, and shear sense (Passchier and Trouw, 2005; Heilbronner and Tullis, 2006).

Before analysis, samples were cut, polished, and made into XZ-plane thin sections, where the "X" denotes the down-plunge direction of stretching lineation and the "Z" denotes the pole to the foliation pointing upward. Thin sections were polished for one hour using a Buehler Alpha and Beta polishing machine and Buehler MasterMet colloidal silica to remove near-surface crystal lattice damage. Data acquisition was performed using a ZEISS EVO-18 scanning electron microscope equipped with an HKL Nordlys EBSD detector at the Institute of Geology, Chinese Academy of Geological Sciences, Beijing. Operating conditions included an accelerating voltage of 15 kV and working distance of 18.4 mm. Scan areas were selected across quasi-homogeneous, multi-phase assemblages or quartz-rich domains or veins. Deformed fabrics in these areas appear to be uniform and parallel to the lineation directions. Step sizes were generally ~8-10 µm such that the smallest visible quartz grains in thin sections had at least four indexed pixels. We eliminated grains smaller than four pixels in the EBSD data and interpret them as analytical noise or polishing defects. We used Oxford Instruments Aztec 3.0 acquisition software for post-analysis processing of indexed EBSD data, including data smoothing, grain detection, map generation (e.g., Fig. S1 in the Supplemental Material¹), and plotting of pole figures of crystallographic axes (i.e., one point per grain, lower hemisphere, and equal area).

Quartz grains were reconstructed from indexed EBSD data (Fig. S1). Grain boundaries were defined by ≥10° misorientations. Subgrain boundaries were defined by 2°-10° misorientations. Acquired quartz lattice preferred orientation (LPO) statistics were used to interpret strain information such as shear sense and/or deformation temperatures (Law, 2014). The asymmetry of the

¹Supplemental Material. Table S1: LA-ICP-MS results for zircon U-Pb geochronology and standard procedure. Text S1: Experiment procedure for apatite (U-Th)/He in this study. Figure S1: Thin-section images of samples analyzed in this study. Figure S2:Thermal history modeling of apatite (U-Th)/ He for all samples under different initial constraints using the QTQt program. Please visit https:// doi.org/10.1130/GEOS.S.21391323 to access the supplemental material, and contact editing@ geosociety.org with any questions.

c-axis skeleton with respect to the reference frames (Z direction) were used to determine the sense of shear (Law, 1990).

Zircon U-Pb Geochronology

Zircon U-Pb dating of metamorphic and igneous samples was performed to determine their ages of crystallization and metamorphism. Zircon grains separated from whole-rock samples using standard procedures were handpicked from heavy-mineral yields using a binocular microscope and mounted in epoxy resin with standard zircons at the Institute of the Hebei Regional Geology and Mineral Survey, Langfang, China. We used zircon standards GJ1 (238U/206Pb age of 604.4 ± 4.7 Ma; Jackson et al., 2004) and 91500 (238U/206Pb age of 1064 Ma; Horn et al., 2000). Cathodoluminescence (CL) imaging was employed to observe internal textures of zircon grains and select appropriate spots for U-Pb dating at Beijing Geoanalysis Co., Ltd., Beijing, China. Zircon U-Pb dating was conducted using an Agilent 7500a inductively coupled plasma-mass spectrometer (ICP-MS) combined with a 193 nm excimer ArF laser-ablation system at the Key Laboratory of Continental Collision and Plateau Uplift, Institute of Tibetan Plateau Research, Chinese Academy of Sciences, Beijing, Considering zircon grain sizes and signal stability, we used 30 µm ablation pits for all grains. U-Pb analyses were performed following the procedure of Xie et al. (2008) (Table S1 [see footnote 1]).

Zircon ages presented are ²⁰⁶Pb/²³⁸U ages for grains younger than 1000 Ma and ²⁰⁷Pb/²⁰⁶Pb ages for grains older than 1000 Ma (Ludwig, 2003). The fractionation correction and results were calculated using GLITTER 4.0 (Macquarie University, Sydney, Australia; http://gemoc.mq.edu.au/glitter/home.html). A common Pb correction was applied following the method described by Andersen (2002). If multiple concordant age populations existed, the weighted mean ages of the populations were interpreted as the inherited, crystallization, and metamorphism age of the sample with consideration of internal grain textures in CL images and Th/U ratios. Uncertainties of individual analyses are listed at the 1σ level and plotted at the 2σ level. All analytical and systematic uncertainties of the weighted mean ages are reported at the 95% confidence level. Age calculations and concordia plots were made using Isoplot 3.0 (Ludwig, 2003). Geochronologic data are presented in Table S1.

Apatite (U-Th)/He Thermochronology

The (U-Th)/He thermochronology method has been widely employed to temporally constrain shallow-crustal geological processes including exhumation of orogenic belts, fault motion, and topographic evolution (Kirby et al., 2002; Boyce et al., 2006; Tian et al., 2014b; Shi et al., 2018b; Zuza et al., 2019; Haproff et al., 2020; Pickering et al., 2020). In this work, we used apatite (U-Th)/He thermochronology (AHe) to understand the

exhumation-related thermal history of the HP rocks of the South Beishan orogen. The closure temperature of the AHe system ranges from ~70–80 °C to ~40 °C (Farley et al., 1996; Stockli et al., 2000; Farley, 2002; Farley and Stockli, 2002; Flowers et al., 2009; Gautheron et al., 2009), which tracks rock cooling through ~1–3 km crustal depths depending on cooling rate and the local geothermal gradient.

Apatite grains were separated from four whole-rock samples using traditional mineral separation techniques at the Institute of the Hebei Regional Geology and Mineral Survey, Langfang, China. Analyses were conducted in the ⁴⁰Ar/⁵⁹Ar and (U-Th)/He Geochronology Laboratory at the Institute of Geology and Geophysics, Chinese Academy of Sciences, Beijing, using an Alphachron MK II noble gas quadrupole mass spectrometer for He extraction and Thermo Fisher X-Series II ICP-MS for U and Th isotopic measurements (Wu et al., 2016c, 2019, 2021). Three to five euhedral apatite grains free of visible inclusions and internal fractures per sample were selected and measured using a microscope. MK-1 apatite (Wu et al., 2019, 2021) was used as a standard. Details on the AHe analytical procedure are described by Wu et al. (2016b, 2019) (Text S1 [see footnote 1]).

RESULTS

Structural Observations

Gubaoquan Area

The HP metamorphic unit is composed of mylonitic quartzo-feldspathic gneiss, mylonitic granitic gneiss, paragneiss, and (retrograded) eclogite and amphibolite (Fig. 6). These rocks are mylonitized and exposed as blocks within a finer-grained metasedimentary matrix. A large (~400 m long and 100 m wide) eclogite lens and smaller eclogite and amphibolite lenses occur within paragneiss and granitic gneiss (Fig. 7). Foliation developed in mechanically less-competent granitic gneiss and paragneiss wraps around the more competent eclogite and amphibolite blocks (Fig. 7).

Based on observed overprinting relationships and geometric patterns of fabric elements, structures related to the emplacement of the HP unit are divided into four deformation episodes (D_1 – D_4). D_1 structures are distributed in the mylonitic granitoid (Fig. 8), which forms the wall rock of the HP unit. D_2 structures are preserved in the HP unit and along its contacts with wall rocks (Fig. 9). D_3 structures were observed only in the HP unit at a single outcrop (Fig. 10). D_4 structures are ubiquitous in the study area (Fig. 7). The foliation (S_1) and stretching lineation (L_1) of D_1 deformation are subparallel to S_2 and L_2 of D_2 deformation due to later D_4 deformation.

The D_1 deformation is characterized by penetrative mylonitic foliation (S_1) defined by the alignment of flaky biotite and muscovite grains and flattened quartz and feldspar grains in gneissic rocks (Figs. 8B and 8C). D_1 structures are well developed in the wall rocks of the HP unit. Throughout most of the

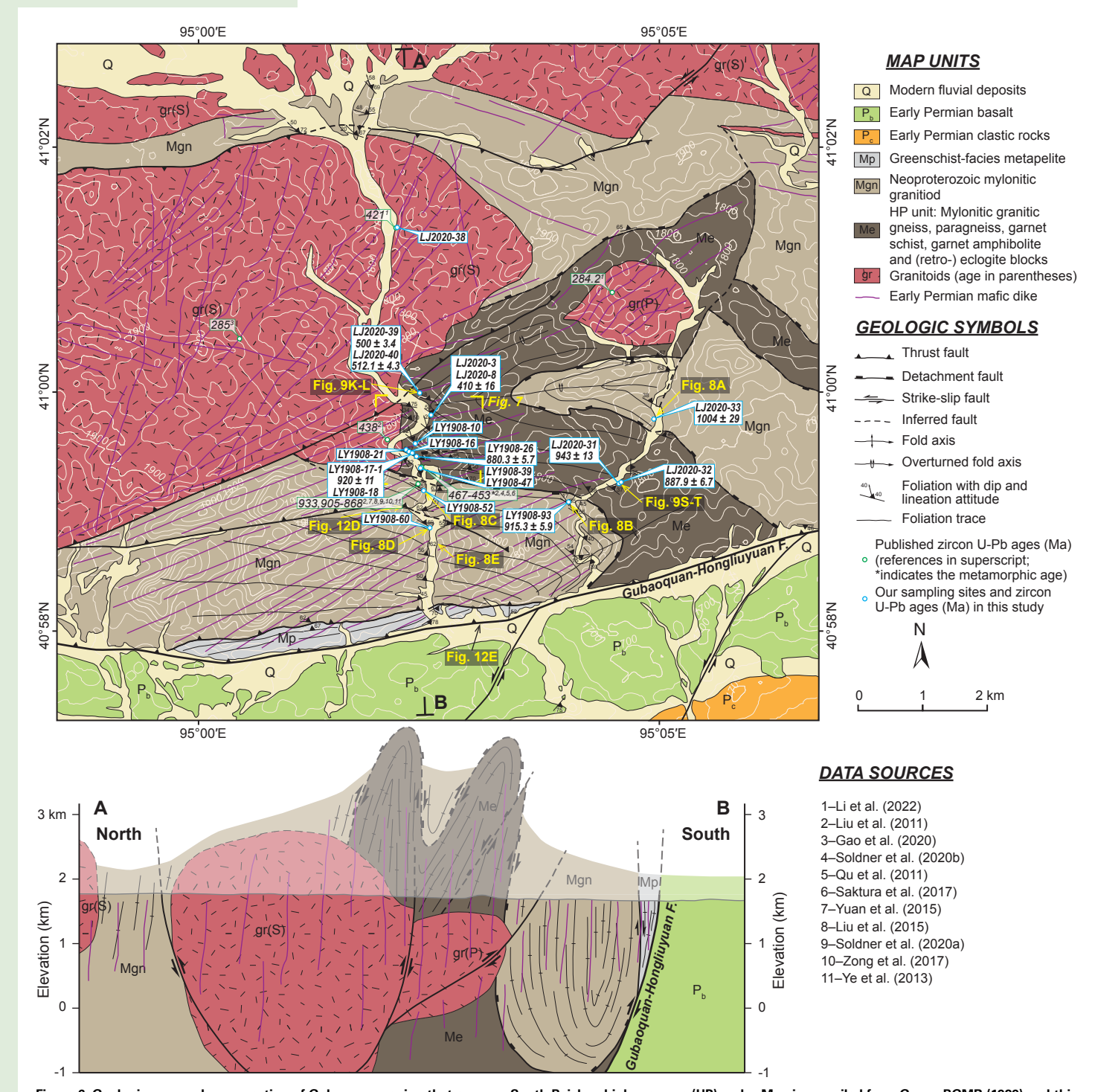


Figure 6. Geologic map and cross section of Gubaoquan region that exposes South Beishan high-pressure (HP) rocks. Map is compiled from Gansu BGMR (1989) and this study. Locations of geo- and thermochronological samples collected as part of this study are shown. Beige lines are topographic contours, labeled in meters. Locations of Figure 7 and related field photographs (Figs. 8, 9, and 12) are shown. S and P in parentheses in map and cross section indicate Silurian and Permian, respectively. Muted colors at top part of cross section represent erosional unit. F—fault.

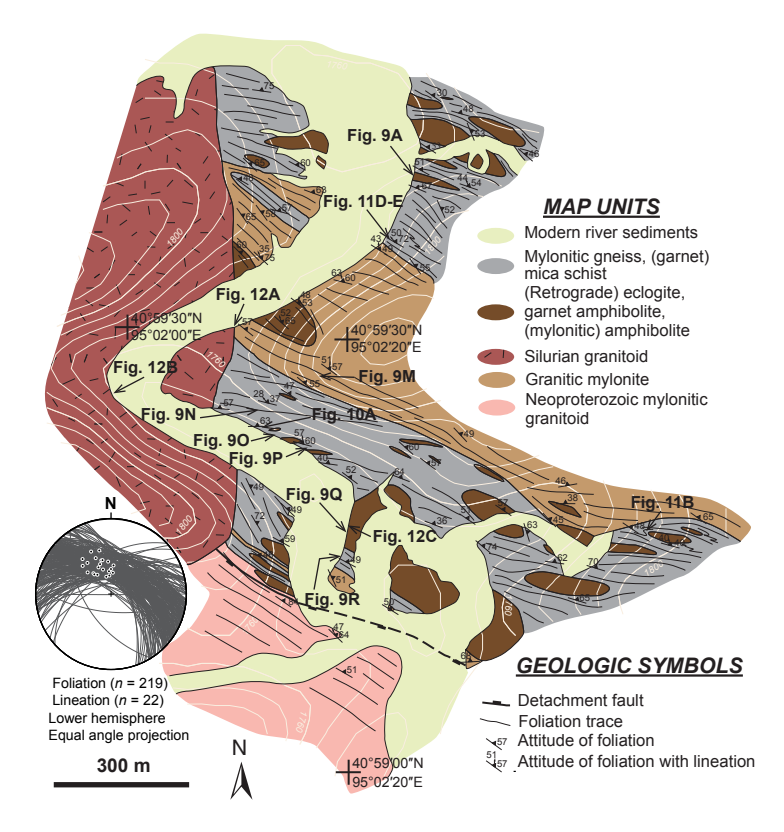


Figure 7. Geologic map showing spatial distribution of South Beishan high-pressure rocks. Inset stereonet plot shows orientations of S_2 foliation and L_2 stretching lineation. Beige lines are topographic contours, labeled in meters. Locations of field photographs (Figs. 9–12) are shown.

study area, S_1 foliation surfaces dip steeply to the north. Poorly developed mineral stretching lineation (L₁) plunges to the north (Figs. 8B–8E). In the eastern part of the Gubaoquan area (Fig. 6), S_1 foliation surfaces are folded by overprinting D₄ deformation. Abundant D₁ kinematic indicators including sigmoidal feldspar grains, S-C fabrics, and domino-type fractures in feldspar grains suggest top-to-the-south shear (Figs. 8B–8E).

The D_2 deformation is characterized by widespread mylonites within the HP unit and their wall rocks (Figs. 6, 7, and 9). Fabric elements include mylonitic foliation (S_2), stretching lineation (L_2), outcrop-scale folds, asymmetric porphyroclasts, and fault-bounded lenses (Figs. 9A–9J). Mylonitic foliation surfaces (S_2) are defined by flattened amphibole, garnet, and mica grains in metasedimentary rocks and (ultra)mafic rocks and alternating mica- and quartz-feldspar-rich layers in mylonitic orthogneiss (Figs. 9K–9M). Within S_2 foliation

surfaces, elongated mica, quartz, feldspar, amphibole, and garnet grains define L_2 stretching lineation (Fig. 9G). S_2 foliation surfaces strike west-northwest to north-northwest and are folded by D_4 deformation such that dips vary from ~40° to 80° (Figs. 6, 7, and 9B). L_2 lineation trends northwest to north-northwest and plunges ~30°–80° (Figs. 6, 7, and 9B). S_2 foliation surfaces are subparallel to S_1 , but L_2 lineation is parallel to the strike of S_2 foliation, suggesting strike-slip kinematics (Figs. 7 and 9B). D_2 kinematic indicators including feldspar porphyroclasts, asymmetric folds, and sigmoidal feldspar grains and (ultra) mafic blocks demonstrate top-to-the-south shear (Figs. 9F, 9H–9J, and 9R–9T).

The D_3 deformation is characterized by an ~3-m-wide shear zone locally exposed within the HP unit (Fig. 10A). S_2 foliation surfaces are overprinted by S_3 shear-zone foliation. S_3 foliation surfaces are defined by alternating mica-and quartz and/or feldspar-rich layers in mylonite. S_3 foliation surfaces strike northeast and dip ~70° to the northwest. D_3 kinematic indicators including asymmetric folds and S-C fabrics demonstrate southeast-side-up shear (Figs. 10A–10C).

Regional folding of the previous S_1 and S_2 foliation formed east-trending, macroscopic D_4 antiforms and synforms (Fig. 6). Folds are upright to south vergent and open to tight, and display rounded to sharp hinges, depending on rock type, at outcrop to kilometer scales (Figs. 6 and 11A–11E). Axial planes strike to the east and dip to the north, implying generation via north-south-oriented contraction with lateral slip. Macroscopic fold hinge zones contain axial-planar, subvertical, east-trending parasitic folds within which S_2 foliation surfaces are folded and oriented subparallel to S_4 axial planes (Figs. 11B–11E).

All metamorphic rocks and structures are intruded and/or truncated by undeformed Silurian granitoids (ca. 438 Ma) and granitic dikes (Figs. 6 and 12A–12C), suggesting that timings of deformation are older than granitoid crystallization (Liu et al., 2011). Metamorphic rocks and granitic intrusions are intruded by east- to east-northeast–striking, subvertical early Permian mafic dikes (Figs. 12A–12C) (Zhang et al., 2015). West-southwest–striking, north-dipping brittle thrust faults that largely occur along river valleys crosscut metamorphic rocks, Silurian intrusions, and early Permian mafic dikes (Figs. 6 and 12D). These thrust faults have been interpreted to be related to late Mesozoic intracontinental transpression (Gillespie et al., 2017; Wang et al., 2017) or late Cenozoic reactivation of pre-existing structures (Cunningham, 2013; Yang et al., 2021a).

Huitongshan-Hongliuyuan Area

The Huitongshan-Hongliuyuan area exposes Carboniferous–Permian strata and major north- to northwest-dipping faults that record sedimentation and deformation histories related to the subduction of Liuyuan oceanic lithosphere (Fig. 13). In the southernmost part of this area, the north-dipping Gubaoquan-Hongliuyuan thrust fault (labeled F1 on Fig. 13) is expressed as an ~50–200-m-wide zone of cataclasite that contains down-dip striations (Figs. 12E and 12F). The footwall of the Gubaoquan-Hongliuyuan fault is composed

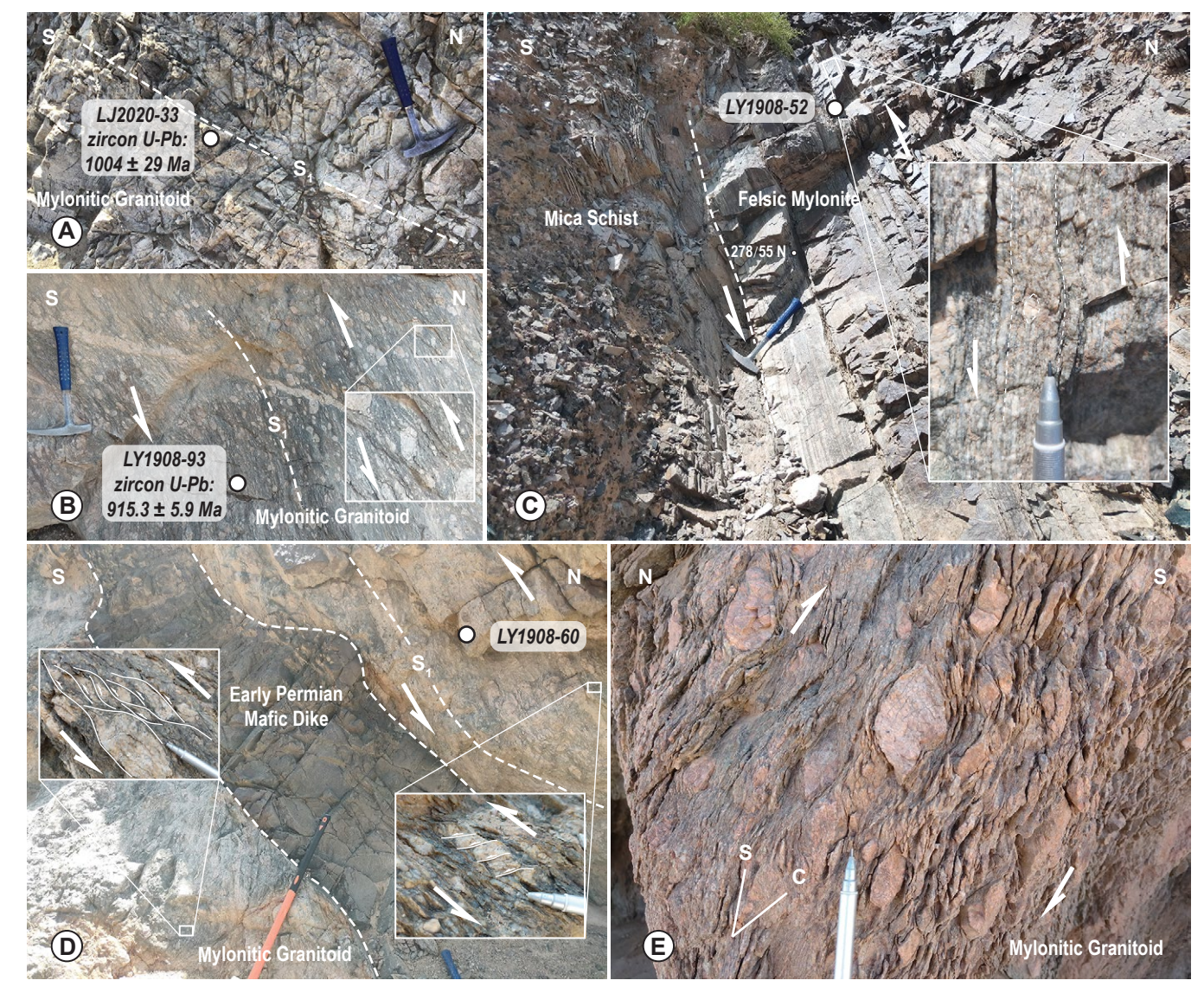


Figure 8. Field photographs of representative structures and sampling locations within wall rock of high-pressure (HP) unit. Photograph locations shown are in Figure 6. (A–B) Neoproterozoic mylonitic granitoid sample LJ2020-33 (A) and strongly foliated Neoproterozoic mylonitic granitoid sample LY1908-93 (B). Note S, foliation (white dashed line) dips to the north, and millimeter- to centimeter-scale, asymmetric feldspar porphyroclasts are indicative of top-to-the-south shear. (C) Strongly foliated felsic mylonite (sample LY1908-52) and mica schist adjacent to contact between HP rocks and its wall rocks; well-developed quartz ribbons and feldspar clasts are indicative of top-to-the-south shear. (D) Early Permian undeformed mafic dike intruding Neoproterozoic mylonitic granitoid (sample LY1908-60). Asymmetric porphyroclasts, domino structure, and duplexing of feldspar clasts (outlined in insets) are indicative of top-to-the-south shear. (E) S-C fabric in mylonitic granitoid indicative of top-to-the-south shear. Note format of bedding and foliation attitude is strike/dip and dip quadrant.

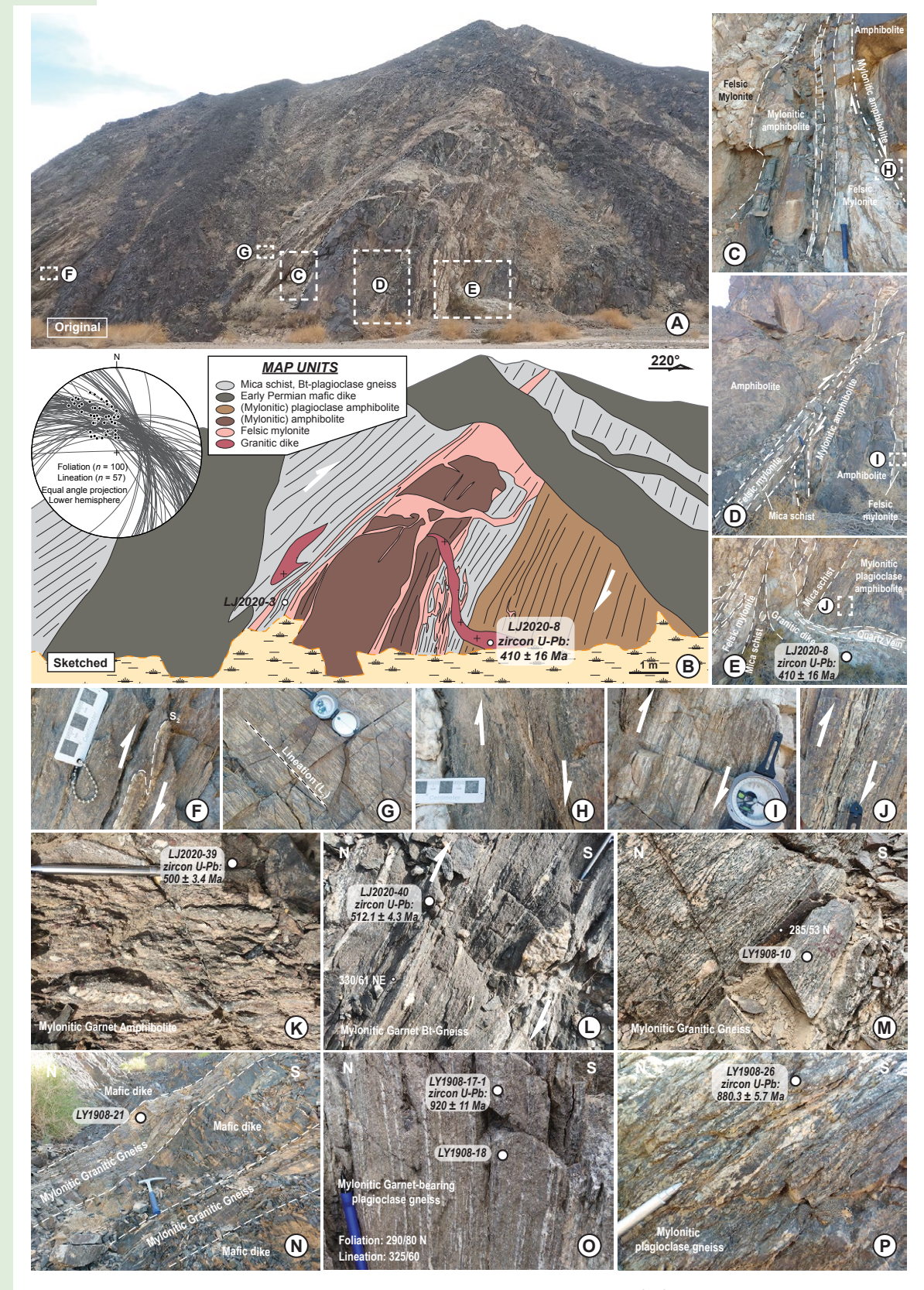


Figure 9. Field photographs of representative structures and sampling locations of high-pressure (HP) unit. Photograph locations are shown in Figures 6 and 7. (A–J) Amphibolite outcrop (A–B) with locations of larger-scale images (C–G); see C–E for locations of H–J. Meter-scale amphibolite boudin is surrounded by mylonitic mica schist and plagioclase gneiss, which are intruded by felsic mylonite. Location of sample LJ2020-3 is shown in B. Inset stereonet plot shows orientations of S₂ foliation and L₂ stretching lineation. Mylonitic kinematic indicators show dextral top-to-the-southwest shear. Mylonitic rocks are intruded by undeformed Devonian granitic dikes (sample LJ2020-8), both of which are intruded by early Permian meter-scale mafic dikes. (K–Q) Samples LJ2020-39, LJ2020-40, LY1908-10, LY1908-21, LY1908-17-1, LY1908-18, LY1908-26, and LY1908-39. (Continued on following page.)

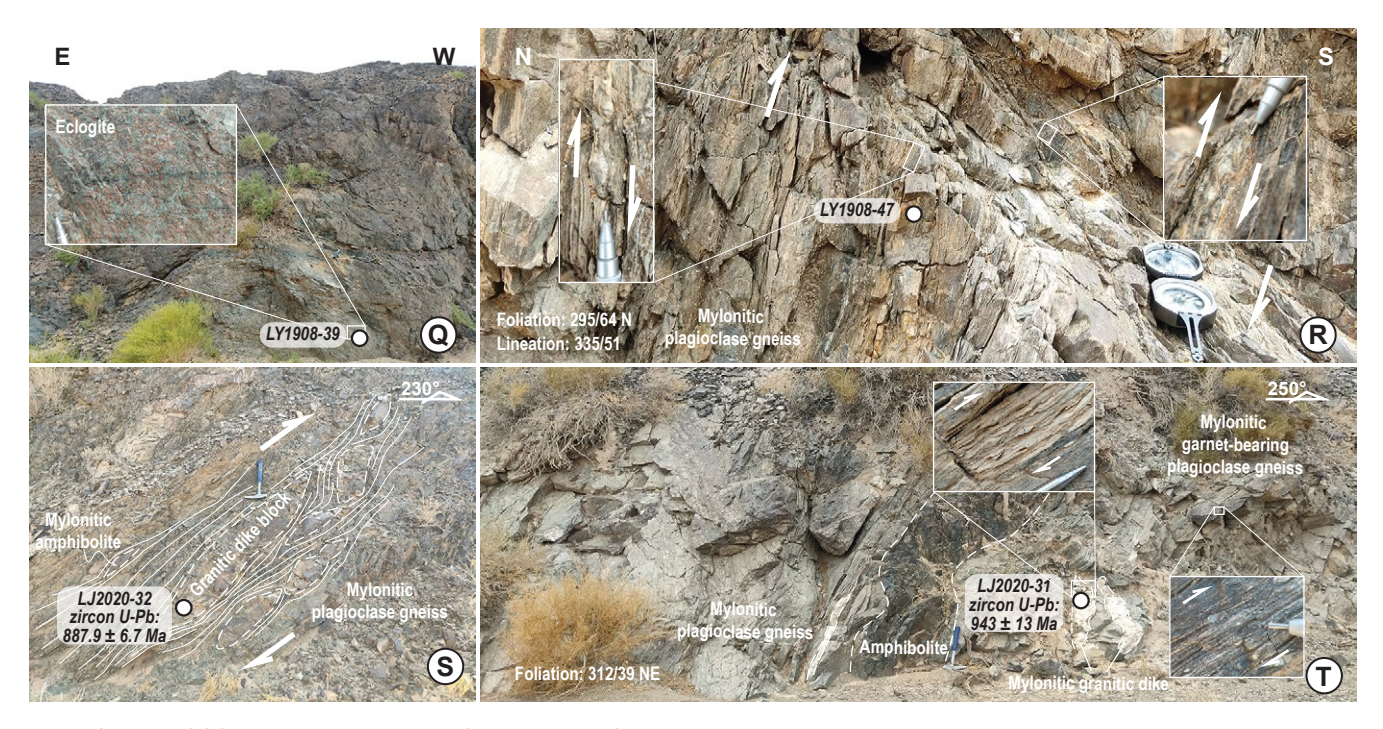


Figure 9 (Continued). (R) Mylonitic plagioclase gneiss (sample LY1908-47) adjacent to contact between HP rocks and wall rocks. Asymmetric feldspar porphyroclasts indicate top-to-the-south shear. (S) Neoproterozoic granitic dike boudins (sample LJ2020-32) surrounded by mylonitic plagioclase gneiss. Duplexing of boudins and S-C fabrics indicate top-to-the-south shear. (T) Amphibolite boudins and mylonitic granitic dikes (sample LJ2020-31) mixed with mylonitic (garnet) plagioclase gneiss. Asymmetric and δ-type feldspar porphyroclasts indicate top-to-the-south shear. Note format of bedding and foliation attitudes is strike/dip and dip quadrant. Bt—biotite.

of early to middle Permian volcanic rocks, whereas the hanging wall consists of Neoproterozoic metamorphic rocks and Carboniferous–Permian shallow-marine and volcaniclastic strata that are duplicated by thrust faults (Fig. 13). To the north, a thrust fault designated F2 juxtaposes Carboniferous rift-related strata in its hanging wall atop Permian rift-related strata in its footwall (Fig. 13). Hanging-wall and footwall rocks are tightly folded into pairs of northeast-trending antiforms and synforms (Fig. 13). Axial planes dip to the northwest. Subhorizontal fold hinge lines suggest that thrusting was directed toward the southeast. The F2 thrust fault links with the Gubaoquan-Hongliuyuan fault in the south and a left-slip thrust fault designated F3 in the north (Fig. 13). The F3 left-slip thrust fault juxtaposes Neoproterozoic metamorphic rocks intruded by Paleozoic intrusions in its hanging wall atop Devonian–Permian volcanoclastic strata in its footwall. In the central part of the Huitongshan-Hongliuyuan area, a low-angle detachment fault designated F4 on Figure 13 juxtaposes Silurian granitoids and Neoproterozoic metamorphic rocks against upper Devonian

and lower-middle Carboniferous supracrustal strata. In general, this fold-and-thrust system resembles a thick-skinned belt based on the involvement of Precambrian crystalline rocks, Paleozoic magmatic intrusions, and strongly folded and faulted supracrustal strata.

Microstructural Observations and EBSD Results

Here we describe our microstructural observations and EBSD results for nine samples of the Liuyuan HP rocks of the South Beishan orogen. All samples are dominated by quartz and feldspar grains and other minor minerals. In our sample descriptions, we do not differentiate feldspar types because plagioclase and alkali feldspars tend to deform similarly (e.g., Hirth and Tullis, 1992; Shigematsu and Tanaka, 2000; Tsurumi et al., 2003; Passchier and Trouw, 2005; Heilbronner and Tullis, 2006; Law, 2014). Figure 14 shows representative



Figure 10. (A) Mylonitic shear zone on either side of granitic dike is intruded by mafic dike. S₃ mylonitic foliation dips to the north. Locations of B and C are shown. (B–C) Asymmetric folded quartz vein and S-C fabric indicate top-to-the-south shear. Note format of bedding and foliation attitudes is strike/dip and dip quadrant.

photomicrographs from the nine samples. Microstructural characteristics of ductile deformation related to exhumation of the Liuyuan HP rocks are presented in Table 3.

Sample LY1908-60 is a mylonitic granitoid collected within the wall-rock unit along the southern exposure of the HP unit (Figs. 8D and 14A). The sample is strongly lineated and foliated and consists of feldspar (~60%), quartz (~30%), and mica (~5%). Mica and quartz form S₁ foliation and L₁ stretching lineation. Quartz grains exhibit core and mantle structure and grain boundaries indicative of dynamic recrystallization via subgrain rotation (SGR). Feldspar grains contain brittle fractures that are filled with recrystallized mica and quartz grains. Microscopic kinematic indicators are abundant including mica fish and shear bands. In addition, the recrystallized quartz grains exhibit undulose extinction related to later deformation episodes (D₄). Recrystallized quartz grains in quartz aggregates are oriented oblique to the shear bands. Kinematic indicators suggest top-to-the-south shear. The LPO pattern of quartz grains shows dominant [c]-axis maxima oblique to foliation near the primitive circle, suggestive of basal <a>> slip at temperatures of ~300-400 °C. In addition, the observed asymmetry (off the [z]-axis) suggests north-side-up shear, which is consistent with kinematics observed in the field (Figs. 8D and 15A).

Sample LY1908-52 is a felsic mylonite collected from the wall-rock unit near the southern margin of the HP metamorphic unit, ~500 m to the north of sample LY1908-60 (Figs. 8C and 14B). Sample LY1908-52 is strongly stretched and flattened and contains a similar mineral assemblage as sample LY1908-60. Elongated feldspar grains define the stretching lineation, and aligned

quartz-composition layers and mica layers define foliation. Quartz subgrains exhibit undulose extinction and strongly serrated quartz boundaries, indicative of dynamic SGR and bulging (BLG) recrystallization. Feldspar grains exhibit deformed mechanical twinning and evidence of BLG recrystallization. The different microstructural characteristics in quartz and feldspar grains suggest superposition of several deformation events with different temperature conditions. The feldspar mechanical twinning reflects higher-temperature deformation than the quartz ductile deformation. This sample experienced stronger deformation compared to the wall rock of the HP metamorphic block due to its position closer to the HP unit. Microscopic kinematic indicators such as mica fish and oblique recrystallized quartz ribbons suggest top-to-the-south shear. The LPO pattern of quartz grains shows dominant [c]-axis maxima in halfway from the primitive circle to the Y-axis, suggesting rhomb <a>> slip at temperatures of ~400–500 °C (Fig. 15B).

Sample LJ2020-3 is mylonitic mica schist collected from the HP metamorphic unit (Figs. 9B and 14C). The sample consists of quartz and mica interlayers that are isoclinally folded, possibly related to either late-stage D_4 deformation or D_2 progressive deformation. The limbs of microfolds are stretched and thinned, and microfold hinge zones are thickened. The boundaries between mica and quartz layers define S_2 foliation. Chessboard quartz aggregates and strongly serrated quartz grain boundaries are indicative of high-temperature dynamic recrystallization via grain boundary migration (GBM). The LPO pattern of quartz grains shows dominant [c]-axis maxima in halfway from the primitive circle to the Y-axis (between the Z-axis and Y-axis), suggesting mixed

Uninterpreted

Figure 11. Field photographs of representative structures in Gubaoquan area. Photograph locations are shown in Figures 5 and 7. (A) Folds within Neoproterozoic metamorphic rocks. Inset stereonet plot shows orientations of foliation and fold axial planes and hinge lines. Orange dashed line near bottom of image represents boundary between exposed rocks and modern river deposits. (B-C) Folds within mylonitic plagioclase gneiss. S₄ defines fold axial planes. (D-E) Isoclinal folded mylonitic plagioclase gneiss, felsic gneiss, and amphibolite boudins. White dashed line shows S₂ foliation, and orange line shows north-dipping S₄ axial planes. Note format of bedding and foliation attitudes is strike/dip and dip quadrant. F.-fault.



Figure 12. (A–C) Early Permian mafic dikes intruding Neoproterozoic high-pressure rocks and Silurian granodiorite, and a late Silurian granitic dike. (D) Faulted valley and breccia in mylonitic granitoid. (E–F) Fault-related rocks of Gubaoquan-Hongliuyuan fault zone. Note format of bedding and foliation attitudes is strike/dip and dip quadrant.

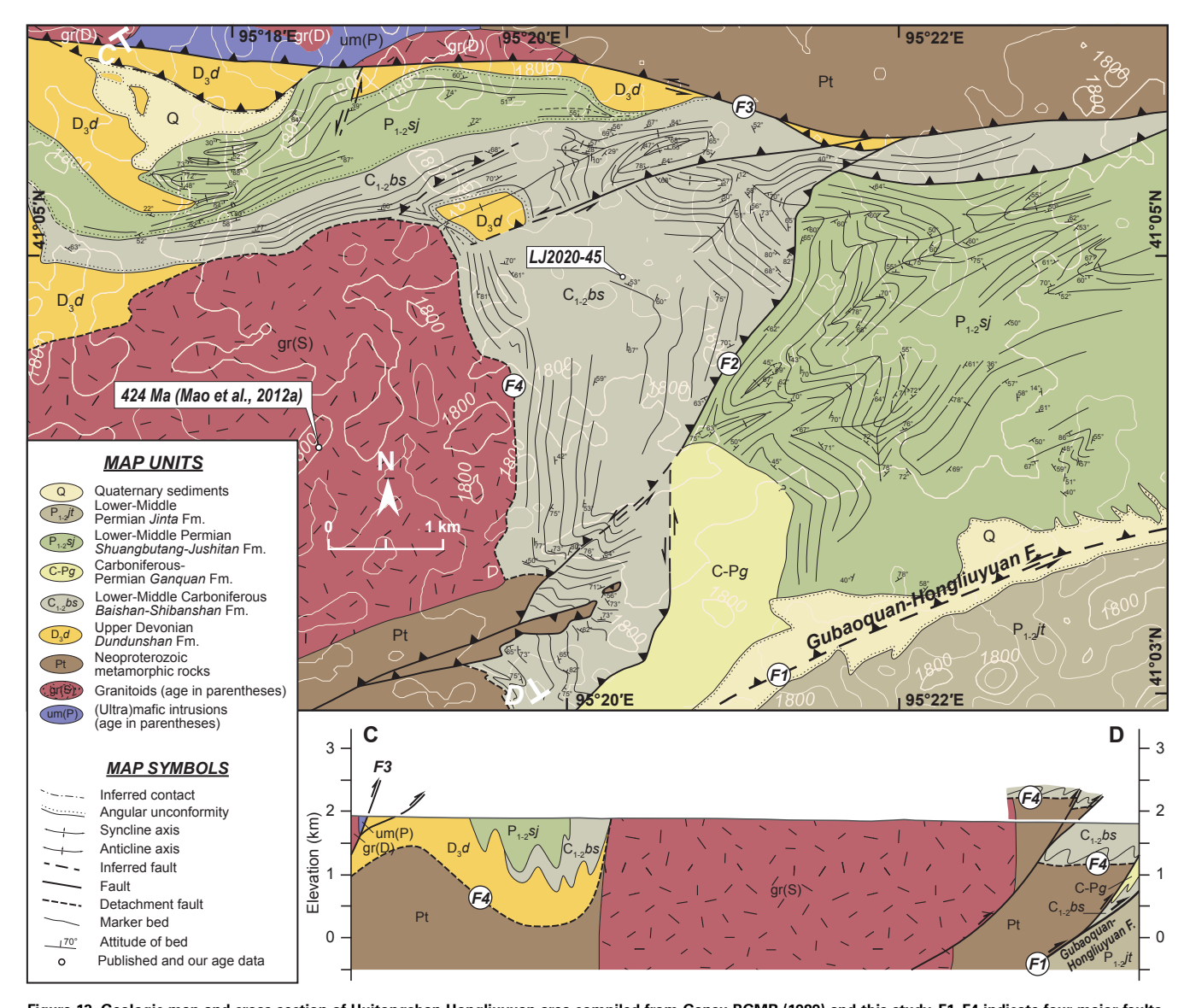


Figure 13. Geologic map and cross section of Huitongshan-Hongliuyuan area compiled from Gansu BGMR (1989) and this study. F1–F4 indicate four major faults in the Huitongshan-Hongliuyuan area. Beige lines are topographic contours, labeled in meters. S, D, and P in parentheses in map figure and cross section indicate Silurian, Devonian, and Permian, respectively. F.—fault.

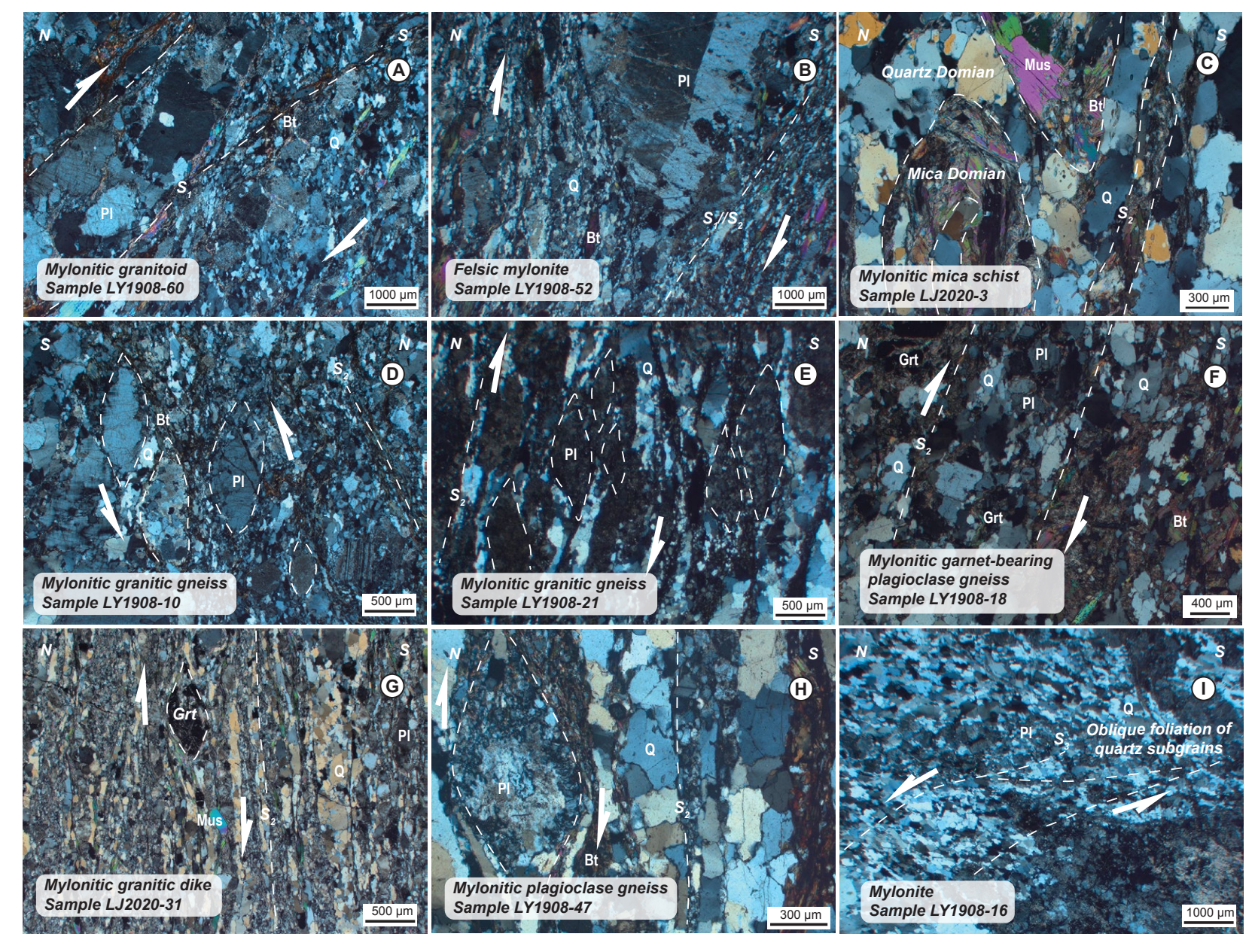


Figure 14. Photomicrographs in crossed-polarized light showing representative microstructures. Q-quartz; Bt-biotite; Pl-plagioclase; Mus-muscovite; Grt-garnet.

TABLE 3. SUMMARY OF MICROSCOPIC STRUCTURAL CHARACTERISTICS AND ELECTRON BACKSCATTER DIFFRACTION (EBSD) DATA*

Sample	Rock type	Foliat	ion	Line	ation		Microscopic structural characteristics	Qua	artz CPO pattern
number		Dip direction (°)	Dip (°)	Trend (°)	Plunge (°)	Shear sense	Microscopic textures ^{†,§}	Shear sense	Slip systems
LJ2020-3	Mylonitic mica schist	19	54	340	44	N.A.	Q: GBM and ribboned grain aggregates, folded banded quartz, and mica compositional layers	Coaxial	Mixed rhomb <a> and basal <a>
LY1908-10	Mylonitic granitic gneiss	15	53	359	45	Top-up-S	PI: BLG and intracrystalline fracture; Q: SGR	N.A.	Prism <c></c>
LY1908-21	Mylonitic granitic gneiss	15	60	355	45	Top-up-S	Q: GBM, SGR, and undulose extinction; Bt: orientation	Coaxial	Basal <a>
LY1908-16	Mylonite	330	70	315	67	Top- down-N	Q: SGR, compositional layering, and undulose extinction	Top-to-N	Mixed basal <a> and rhomb <a>
LY1908-18	Mylonitic garnet- bearing plagioclase gneiss	20	80	325	60	Top-up-S	Pl: mechanical twinning; Q: GBM and undulose extinction	N.A.	Weak CPO
LY1908-47	Mylonitic plagioclase gneiss	25	64	335	51	Top-up-S	PI: BLG; Q: SGR and BLG; Bt: orientation and mica fish	Top-to-S	Mixed prism <a>, rhomb <a>, and basal <a>
LJ2020-31	Mylonitic granitic dike	65	39	34	24	Top-up-S	PI: BLG and mechanical twinning; Mus: mica fish and orientation; Grt: brittle fracture; Q: SGR, BLG, ribboned grain aggregates, and undulose extinction	N.A.	Mixed prism <a> and rhomb <a>
LY1908-52	Felsic mylonite	8	55	3	51	Top-up-S	PI: BLG and mechanical twinning; Q: SGR, BLG, and undulose extinction	Top-to-S	Rhomb <a>
LY1908-60	Mylonitic granitoid	12	62	18	56	Top-up-S	PI: intracrystalline fracture; Mus: orientation; Q: SGR and undulose extinction	Top-to-S	Basal <a>

^{*}For some typical microstructural features of deformation mechanisms, see Hirth and Tullis (1992), Shigematsu and Tanaka (2000), Stipp et al. (2002), and Heilbronner and Tullis (2006).

basal <a> slip at low temperatures and rhomb <a> activity at temperatures of \sim 400–500 °C (Fig. 15C).

Sample LY1908-10 is a mylonitic granitic gneiss collected from the HP metamorphic unit (Figs. 9M and 14D). The mineral assemblage consists of feldspar, recrystallized quartz, and minor mica. Quartz grains show evidence of SGR recrystallization. Feldspar grains contain intracrystalline brittle fractures and show evidence of BLG recrystallization. The recrystallized feldspar subgrains distributed along fracture surfaces show that brittle fracturing occurred before the BLG recrystallization. Asymmetric feldspar porphyroclasts indicate topto-the-south shear. The LPO pattern of quartz grains shows dominant [c]-axis maxima slightly inclined from the foliation, suggestive of prism <c> slip at relatively high temperatures and/or enhanced water content (Fig. 15D).

Sample LY1908-21 is a mylonitic granitic gneiss collected from the HP metamorphic unit (Figs. 9N and 14E). The sample contains feldspar, quartz ribbons, and deformed mica along with the cleavage domains that define S_2 foliation and L_2 stretching lineation. Quartz subgrains exhibit late-stage undulose extinction and early-stage strongly serrated boundaries indicative of SGR and GBM

recrystallization, which suggest that the later lower-temperature deformation events (D_3-D_4) were superposed on the early higher-temperature deformation fabrics (D_2) . Asymmetric, mantled feldspar porphyroclasts indicate top-to-the-south shear. The LPO pattern of quartz grains shows dominant [c]-axis maxima near the primitive circle, suggesting basal <a> slip at relatively low temperatures (Fig. 15E).

Sample LY1908-18 is a mylonitic garnet-bearing plagioclase gneiss collected from the HP metamorphic unit (Figs. 9O and 14F). The sample contains feldspar, quartz, mica, and garnet. S_2 foliation and L_2 stretching lineation are defined by layers and rods of mica, quartz, and feldspar. Quartz grains exhibit latestage undulose extinction and evidence of early-stage GBM recrystallization. Mechanical twinning in feldspar grains was observed. The LPO pattern of quartz grains shows distributed [c]-axis maxima, suggesting a weak crystallization preferred orientation (CPO) (Fig. 15F).

Sample LJ2020-31 is a mylonitic granitic dike collected from the HP metamorphic unit near sample LJ2020-32 (Figs. 9T and 14G). Sample LJ2020-31 contains garnet and alternating mica- and quartz and/or feldspar-rich layers

[†]Q—quartz; PI—plagioclase; Bt—biotite; Mus—muscovite; Grt—garnet.

[§]GBM—grain-boundary migration recrystallization; BLG—bulging recrystallization; SGR—subgrain recrystallization.

Note: N.A.—not available; CPO—crystallization preferred orientation.

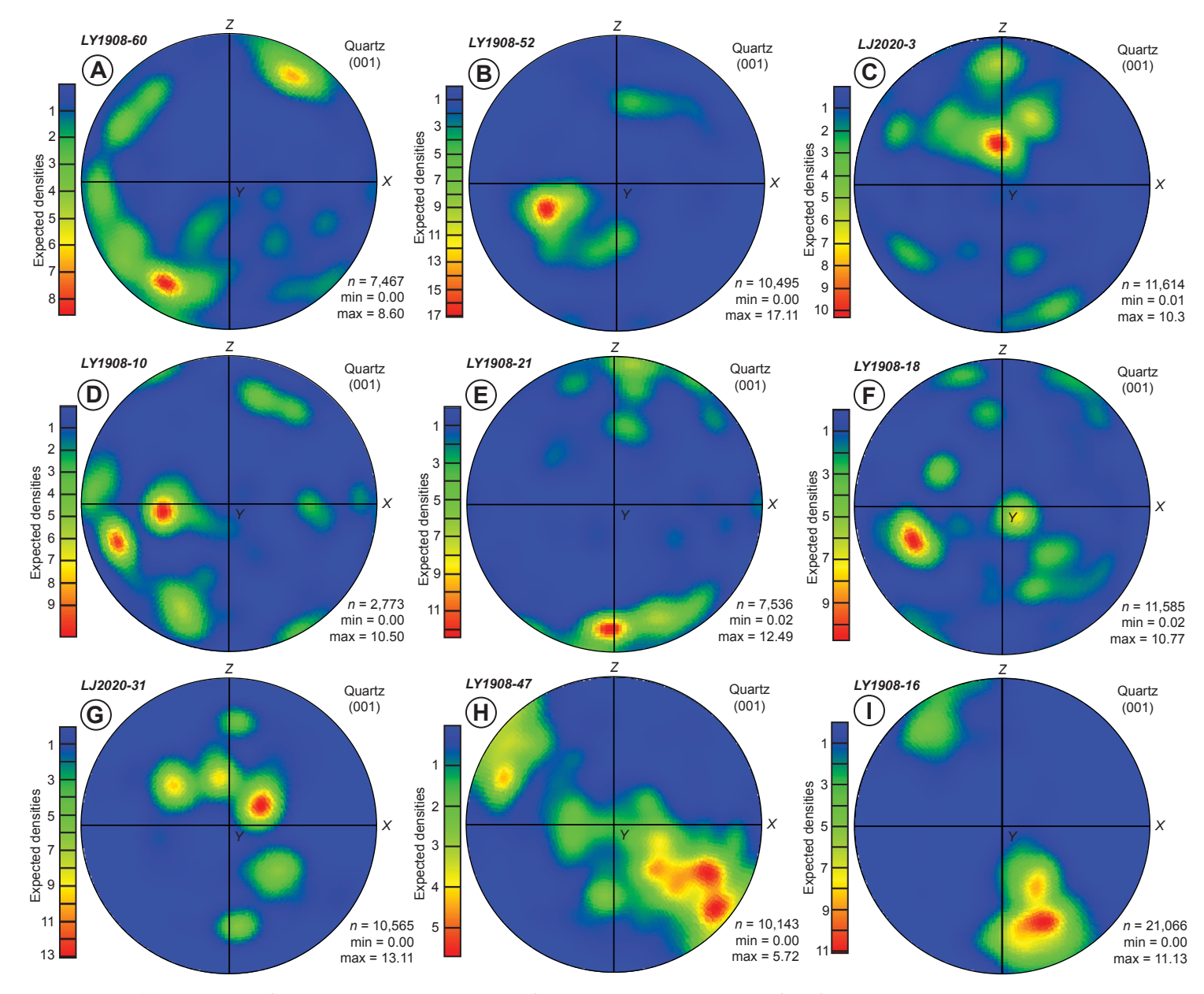


Figure 15. Quartz [c]-axis pole figures (lower hemisphere, equal-area projection) from electron backscatter diffraction (EBSD) analyses. Min and max refer to minimum and maximum expected densities for [c]-axis poles.

and rods that define S_2 foliation and L_2 stretching lineation, respectively. Feldspar grains exhibit mechanical twinning and evidence of BLG recrystallization. Quartz grains exhibit undulose extinction. Garnet grains contain brittle fractures. Asymmetric tails of garnet and mica fish indicate top-to-the-south shear. The LPO pattern of quartz grains shows dominant [c]-axis maxima in halfway from the primitive circle to the *Y*-axis, suggesting mixed prism <a> and rhomb <a> slip (Fig. 15G).

Sample LY1908-47 is a mylonitic plagioclase gneiss collected from the detachment shear zone between the HP metamorphic unit and wall-rock unit (Figs. 9R and 14H). The sample contains feldspar and alternating mica- and quartz-rich layers that define S_2 foliation. Feldspar grains exhibit evidence of BLG recrystallization, whereas quartz grains exhibit lower-temperature deformation fabrics evidenced by SGR and BLG recrystallization. Asymmetric feldspar porphyroclasts and mica fish indicate top-to-the-south shear. The LPO pattern of quartz grains shows dominant [c]-axis maxima oblique to the foliation and distributed from the primitive circle to the *Y*-axis, suggesting a mixing prism <a>, rhomb <a>, and basal <a> slip (Fig. 15H).

Sample LY1908-16 is a mylonite collected from the HP metamorphic unit (Figs. 10A and 14l). The sample contains feldspar, recrystallized quartz, and minor mica. Striped quartz aggregates define S_3 foliation. Quartz grains exhibit late-stage undulose extinction and early-stage evidence of SGR recrystallization. Oblique foliation surfaces formed by quartz subgrains indicate south-side-up shear, which is consistent with field observations. The LPO pattern of quartz grains shows dominant [c]-axis maxima oblique to the foliation and halfway from the primitive circle to the *Y*-axis (near the primitive circle), suggesting mixed basal <a> and rhomb <a> slip at medium to low temperatures. The observed quartz asymmetry (off the [z]-axis) suggests south-side-up shear, which is consistent with the observed kinematics in the field (Figs. 10 and 15l).

In summary, the combination of dominant basal <a>> slip of quartz LPOs, deformation temperatures evidenced by quartz SGR recrystallization, and brittle fractures in feldspar indicate that D₁ deformation occurred at low temperatures of ~300-400 °C (Hirth and Tullis, 1992; Lloyd and Freeman, 1994; Stipp et al., 2002; Passchier and Trouw, 2005). Microtextural kinematic indicators suggest north-side-up shear, which is consistent with the guartz LPOs. Most samples from the HP metamorphic unit show medium to high temperatures $(\sim 500-600 \, ^{\circ}\text{C})$ (Okudaira et al., 1995; Stipp et al., 2002; Toy et al., 2008). D₂ deformation fabrics have been overprinted by later medium- to low-temperature deformation fabrics (e.g., Shigematsu and Tanaka, 2000; Heilbronner and Tullis, 2006). Evidence of subsolidus quartz recrystallization and LPOs suggest that north-side-up shear occurred along the tectonic contact between the HP metamorphic unit and wall-rock unit. The dominant guartz LPOs and guartz recrystallization textures indicate that D₃ deformation occurred at medium temperatures (~400-450 °C) (Neumann, 2000). Kinematic indicators and quartz LPOs suggest south-side-up shear. D₁ deformation may have occurred at lower temperatures (>300 °C), as evidenced by quartz extinction and microfolds (e.g., Stipp et al., 2002; Passchier and Trouw, 2005).

Zircon U-Pb Ages

Nine samples were collected from the South Beishan orogen and analyzed, including two mylonitic granitoid samples from the wall-rock unit and seven samples of the HP metamorphic unit (Fig. 6). Concordia diagrams and relative probability plots depicting age results of single-shot zircon analyses are shown in Figure 16. Detailed geochronologic data are provided in Table S1 (see footnote 1).

Sample LJ2020-39 was collected from mylonitic garnet-bearing amphibolite of the HP metamorphic unit (Fig. 9K). Analyses of 30 zircon grains including cores and rims yield ages between ca. 487 Ma (U-Pb) and ca. 1533 Ma (Pb-Pb) that are clustered in three age populations (Fig. 16A). We interpret that the weighted mean age of 500 ± 3.4 Ma (mean square of weighted deviates [MSWD] = 0.91) from the youngest population of 16 analyses represents a metamorphic age of the amphibolite experienced in the Cambrian. These 16 analyses were performed on zircon grain rims and yield relatively low Th/U values (<0.1) (Fig. 17). Furthermore, these spots display unclear zoning and dark-gray CL image (Fig. 16A). The two older age populations with weighted mean ages of $1359 \pm 66 \text{ Ma}$ (MSWD = 0.042; n = 4) and $1488 \pm 39 \text{ Ma}$ (MSWD = 1.5; n = 5) are interpreted to be the protolith age of the amphibolite and inherited zircon ages, respectively. These analyses were performed on zircon grain cores and yield relatively high Th/U values (>0.1) (Fig. 17). Most age spots display CL-bright image and well-preserved oscillatory zoning (Fig. 16A). Younger ages between ca. 1400 Ma and ca. 600 Ma may be the result of Pb loss, given that fluid infiltration and mineral modification could have occurred within the deformed and metamorphosed rock.

Sample LJ2020-40 was collected from mylonitic garnet-bearing biotite gneiss located ~2 m from sample LJ2020-39 (Fig. 9L). Analyses of 30 zircon grains including cores and rims yield ages between ca. 501 Ma (U-Pb) and ca. 1493 Ma (Pb-Pb) that are clustered in two age populations (Fig. 16B). The younger population of 19 analyses has a weighted mean age of 512.1 \pm 4.3 Ma (MSWD = 1.7), which is interpreted to be a metamorphic age of the biotite gneiss. The 19 analyses were performed on zircon grain rims and yield relatively low Th/U values (<0.1) (Fig. 17). These spots display a CL-dark image and unclear zoning (Fig. 16B). The older population of seven analyses yields a weighted mean age of 1429 \pm 39 Ma (MSWD = 4.7), which is interpreted to represent the protolith age of the biotite gneiss. These analyses were performed on zircon grain cores and yield relatively high Th/U values (>0.1) (Fig. 17). Some cores display well-preserved oscillatory zoning; however, most are blurred (Fig. 16B).

Sample LJ2020-8 was collected from an undeformed granitic dike that intrudes the HP metamorphic unit (Fig. 9E). Analyses of 25 zircon grains yield weighted mean ages between ca. 397 Ma (U-Pb) and ca. 1589 Ma (Pb-Pb) that are clustered in three age populations (Fig. 16C). The youngest population of five analyses has a weighted mean age of 410 ± 16 Ma (MSWD = 4.8), which is interpreted to be the crystallization age of the granitic dike. These analyses were performed on zircon grains with clear oscillatory zoning and CL-bright

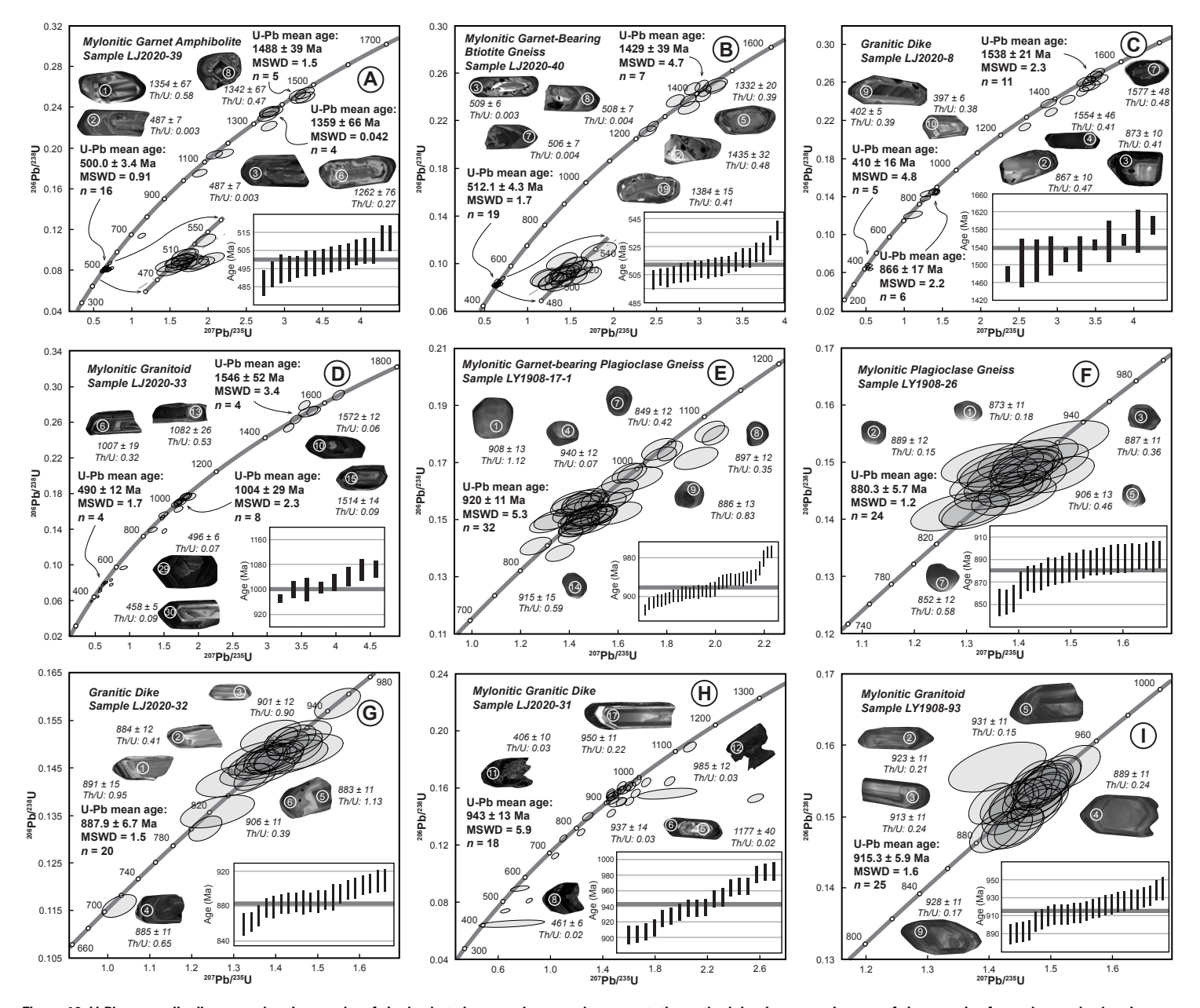


Figure 16. U-Pb concordia diagrams showing results of single-shot zircon analyses, and representative cathodoluminescence images of zircon grains for each sample showing age (in Ma) and Th/U ratio. Error ellipses are 2σ. Circles represent ~30 μm analyzed spots for U-Pb dating. Insets show weighted mean age for selected zircon grains. MSWD—mean square of weighted deviates.

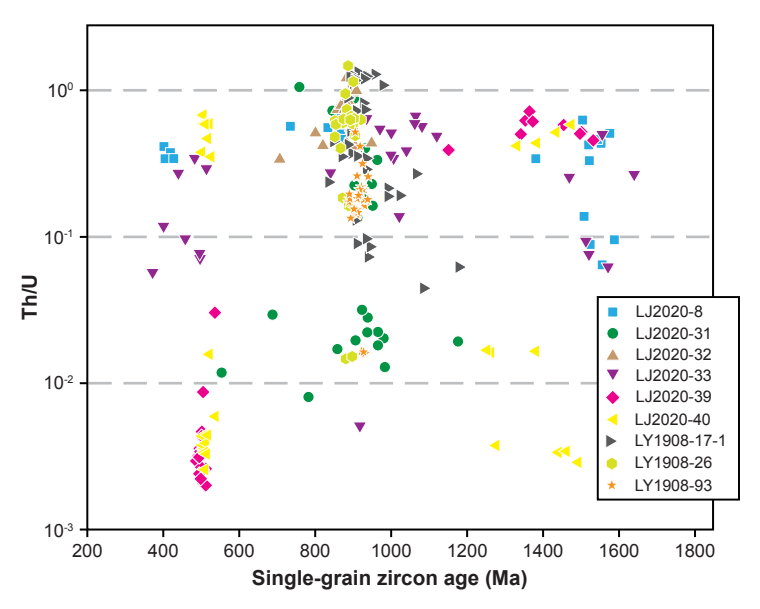


Figure 17. Th/U versus age diagram of zircon grains of samples in this study.

image that yield relatively high Th/U values (>0.1) (Figs. 16C and 17). The two older populations with weighted mean ages of 866 \pm 17 Ma (MSWD = 2.2; n = 6) and 1538 \pm 21 Ma (MSWD = 2.3; n = 11) are interpreted to be inherited zircon grains and are consistent with the ages of wall rocks. Some cores display well-preserved oscillatory zoning, but others are blurred (Fig. 16C). The occurrence of abundant inherited zircon grains may be the result of remelting of original rock or represent the crystallization ages of wall rocks.

Sample LJ2020-33 was collected from mylonitic granitoid, which is the wall rock of the HP metamorphic unit (Fig. 8A). Analyses of 30 zircon grains yield ages between ca. 372 Ma (U-Pb) and ca. 1641 Ma (Pb-Pb) that are clustered in three age populations (Fig. 16D). The youngest population of four analyses has a weighted mean age of 490 \pm 12 Ma (MSWD = 1.7), which is interpreted to be a metamorphic age of the granitoid. These four analyses were performed on zircon grain rims that yield relatively low Th/U values (<0.1) (Fig. 17). These age spots display a CL-dark and unclear internal textures (Fig. 16D). Assuming that the oldest age population with a weighted mean age of 1546 \pm 52 Ma (MSWD = 3.4; n = 4) reflects inheritance, the middle age population with a weighted mean of 1004 \pm 29 Ma (MSWD = 2.3; n = 8) may best represent the crystallization age of the granitoid. These analyses were performed on zircon grains with clear oscillatory zoning (Fig. 16D) that yield relatively high Th/U values (>0.1) (Fig. 17). The remaining discordant single-grain ages may be the result of Pb loss during a later metamorphic event.

Sample LY1908-17-1 was collected from mylonitic garnet-bearing plagioclase gneiss located within the HP metamorphic unit (Fig. 90). Analyses of 40 zircon grains yield concordant ages between ca. 836 Ma (U-Pb) and ca. 1086 Ma (Pb-Pb) (Fig. 16E). These zircon grains in CL images display CL-dark image and unclear internal textures. The weighted mean age of 32 concordant analyses is 920 ± 11 Ma (MSWD = 5.3), which is interpreted to be the protolith age of the gneiss based on high Th/U values (>0.1) (Fig. 17).

Sample LY1908-26 was collected from mylonitic plagioclase gneiss located ~20 m from sample LY1908-17-1 (Fig. 9P). Analyses of 24 zircon grains yield concordant U-Pb ages between ca. 852 Ma and ca. 921 Ma (Fig. 16F). CL images of these grains display CL-dark image and blurred internal textures. The weighted mean age of the concordant analyses is 880.3 ± 5.7 Ma (MSWD = 1.2), which is interpreted to be the protolith age of the gneiss based on high Th/U values (>0.1) (Fig. 17).

Sample LJ2020-32 was collected from an imbricated granitic dike within the HP metamorphic unit (Fig. 9S). Analyses of 25 zircon grains yield concordant U-Pb ages between ca. 801 Ma and ca. 949 Ma (Fig. 16G). The weighted mean of 20 analyses is 887.9 \pm 6.7 Ma (MSWD = 1.5), which is interpreted to be the crystallization age of the granitic dike. These analyses were performed on zircon grains with clear oscillatory zoning that yield relatively high Th/U values (>0.1) (Figs. 16G and 17).

Sample LJ2020-31 was collected from a mylonitic granitic dike located ~10 m from sample LJ2020-32 (Fig. 9T). Analyses of 30 zircon grains yield concordant ages between ca. 554 Ma (U-Pb) and ca. 1177 Ma (Pb-Pb) (Fig. 16H). The weighted mean age of 18 analyses is 943 ± 13 Ma (MSWD = 5.9), which is interpreted to be the crystallization age of the granitic dike. These concordant age spots display well-preserved oscillatory zoning and CL-bright image (Fig. 16H). One zircon grain core age of 1177 ± 40 Ma is interpreted to be inherited based on the spot location and low Th/U value of 0.02. The remaining discordant and younger ages from grain spots with CL-dark image and blurred internal textures may be a product of Pb loss during a later metamorphic event (Fig. 16H).

Sample LY1908-93 was collected from mylonitic granitoid in the wall rock of the HP unit (Fig. 8B). Analyses of 25 zircon grains yield concordant U-Pb ages between ca. 889 Ma and ca. 940 Ma (Fig. 16I). The weighted mean age of the concordant analyses is 915.3 \pm 5.9 Ma (MSWD = 1.6), which is interpreted to be the crystallization age of the granitoid. These analyses were performed on zircon grains with clear oscillatory zoning that yield relatively high Th/U values (>0.1) (Fig. 17).

In summary, zircon grains of nine samples collected from the South Beishan orogen record its Mesoproterozoic–Devonian magmatic-metamorphic evolution. Most zircon grains have Mesoproterozoic crystallization ages (ca. 1546–1359 Ma) and contain clear zircon oscillatory zoning and high Th/U values (>0.1) (Figs. 16 and 17). These age results suggest that Mesoproterozoic basement rocks occur in the South Beishan orogen. Early Neoproterozoic (ca. 1004–866 Ma) zircon grains are subdivided into magmatic and metamorphic origins according to their internal texture and Th/U values (Figs. 16 and 17),

which is consistent with previous studies (e.g., Liu et al., 2015; Yuan et al., 2015; Zong et al., 2017). Cambrian (ca. 512–490 Ma) metamorphism is recorded in the South Beishan orogen based on the occurrence of metamorphic zircon grains (samples LJ2020-33, LJ2020-39, and LJ2020-40) that have dim zircon internal textures and low Th/U values (<0.1) (Figs. 16 and 17). The early Devonian (410 Ma; sample LJ2020-8) granitic intrusion shows evidence of crustal remelting, including inherited zircons of early Neoproterozoic and Mesoproterozoic wall rocks (Fig. 16C).

Apatite (U-Th)/He Ages and Thermal History Modeling

Apatite (U-Th)/He (AHe) ages can be complicated by radiation damage to the apatite crystal lattice (Flowers et al., 2009; Gautheron et al., 2009; Flowers and Kelley, 2011), which increases with effective uranium concentration (eU). Radiation damage can inhibit the diffusion of α particles and result in an excess of α particles within the crystal lattice so that the measured age is positively correlated with the concentration of eU. Thus, a positive correlation of AHe age and eU concentration implies the effect of radiation damage (Flowers et al., 2009; Flowers and Kelley, 2011). The AHe results (Table 4) show that the eU in all grains ranges from 0 to 100 ppm (Fig. 18A), with no obvious correlation between AHe ages and eU. Furthermore, the equivalent radius of apatite grains, half of the distance across the hexagonal prism, from each sample is >40 μ m (Fig. 18B), which meets the experimental requirements, and there was no obvious correlation between AHe ages and equivalent radius. Based

on our age characteristics, the apatite grains are not significantly affected by radiation damage, and thus the obtained mean AHe ages represent the timing during which the samples cooled through an effective closure temperature range of ~70–80 °C (Stockli et al., 2000; Farley, 2002; Farley and Stockli, 2002; Flowers et al., 2009).

We collected four representative samples for apatite (U-Th)/He thermochronology. Sample LJ2020-45 is a sandstone collected from the Carboniferous strata in the Huitongshan-Hongliuyuan area (Fig. 13), which yields AHe ages between 114.63 ± 6.40 Ma and 90.80 ± 4.90 Ma (Table 4). Sample LJ2020-38 is a Silurian monzogranite collected from the Gubaoquan area (Fig. 6), which yields AHe ages between 194.14 ± 10.67 Ma and 113.19 ± 6.18 Ma (Table 4). Sample LJ2020-40 is a mylonitic garnet biotite gneiss collected from the Gubaoquan area (Fig. 6), which yields AHe ages between 252.11 ± 14.12 Ma and 133.90 ± 7.44 Ma (Table 4). Sample LY1908-39 is an eclogite collected from the Gubaoquan area (Fig. 6), which yields AHe ages between 178.37 ± 12.52 Ma and 83.19 ± 5.36 Ma (Table 4). Imperfect grains or unnoticed inclusions may have led to some of the observed age dispersion (Fig. 18A).

The AHe ages for all samples collected from the South Beishan orogen are between ca. 83 and ca. 252 Ma (Table 4). These AHe ages are younger than the known deposition and crystallization ages of the samples. This indicates that all samples experienced cooling through temperatures associated with AHe closure.

To explore possible thermal histories for our samples from the South Beishan orogen, AHe ages were incorporated in inverse modeling using the QTQt program (Gallagher, 2012). The nominal closure temperature values of 40–80 °C

TABLE 4. RESULTS OF SINGLE-GRAIN APATITE (U-Th)/He DATING IN THIS STUDY*

Sample number	U	Th	⁴He	Th/U	[eU]	Length	Width	R _s	Mass	$F_{\tau}^{\#}$	Raw age	Error	Corrected age	Error
(grain number)	(ppm)	(ppm)	(nmol/g)		(ppm) [†]	(µm)	(µm)	(µm)§	(µg)		(Ma)	(1σ)	(Ma)	(1σ)
LJ2020-45(1)	91.76	12.77	44.5676	0.14	94.76	144	116	55.9	4.03	0.76	87.23	2.16	114.63	6.40
LJ2020-45(2)	49.06	19.27	24.1552	0.41	53.58	189	127	64.3	6.44	0.79	83.58	2.01	106.20	5.89
LJ2020-45(3)	29.34	10.22	15.4511	0.36	31.74	286	181	92.7	19.69	0.85	90.22	2.11	106.14	5.86
LJ2020-45(4)	10.52	37.46	6.8777	3.68	19.33	170	100	51.8	3.53	0.72	65.74	1.34	90.80	4.90
LJ2020-38(1)	10.34	17.90	7.7186	1.79	14.54	212	101	54.8	4.58	0.74	98.04	2.19	131.77	7.22
LJ2020-38(2)	15.70	30.93	10.0959	2.04	22.97	159	96	49.4	3.05	0.72	81.27	1.78	113.19	6.18
LJ2020-38(3)	15.74	29.73	11.8594	1.95	22.72	165	101	52.3	3.57	0.73	96.40	2.11	131.69	7.19
LJ2020-38(4)	15.01	26.75	15.6624	1.84	21.29	155	88	45.9	2.50	0.70	135.51	3.10	194.14	10.67
LJ2020-40(1)	20.90	2.58	24.4105	0.13	21.50	270	150	78.5	12.63	0.83	208.24	5.25	252.11	14.12
LJ2020-40(2)	14.55	0.68	11.3926	0.05	14.71	286	177	91.1	18.83	0.85	142.93	3.63	168.35	9.44
LJ2020-40(3)	14.71	0.41	9.1251	0.03	14.80	303	180	93.0	30.40	0.85	114.08	2.76	133.90	7.44
LJ2020-40(4)	10.58	0.86	11.1683	0.08	10.78	249	180	89.0	16.77	0.85	190.33	4.80	225.24	12.61
LY1908-39(1)	0.29	1.42	0.2166	5.00	0.63	155	131	62.6	5.61	0.77	63.81	2.59	83.19	5.36
LY1908-39(2)	1.22	2.81	0.7074	2.38	1.88	142	105	52.0	3.32	0.73	69.44	2.04	95.12	5.52
LY1908-39(3)	0.10	0.84	0.2251	8.92	0.29	223	139	71.5	9.09	0.79	140.73	6.93	178.37	12.52
LY1908-39(4)	0.22	1.26	0.2296	5.87	0.52	151	140	64.9	6.15	0.77	81.84	2.76	105.74	6.38

^{*}For geological information of samples, see Table 2.

[†]Effective uranium content [eU] = [U] + $0.235 \times [Th]$ (Flowers et al., 2009).

[§]Radius of a sphere with the equivalent surface area-to-volume ratio as cylindrical crystals (Meesters and Dunai, 2002).

^{*}The α-ejection correction (Farley et al., 1996) calculated using mass-weighted average radii.

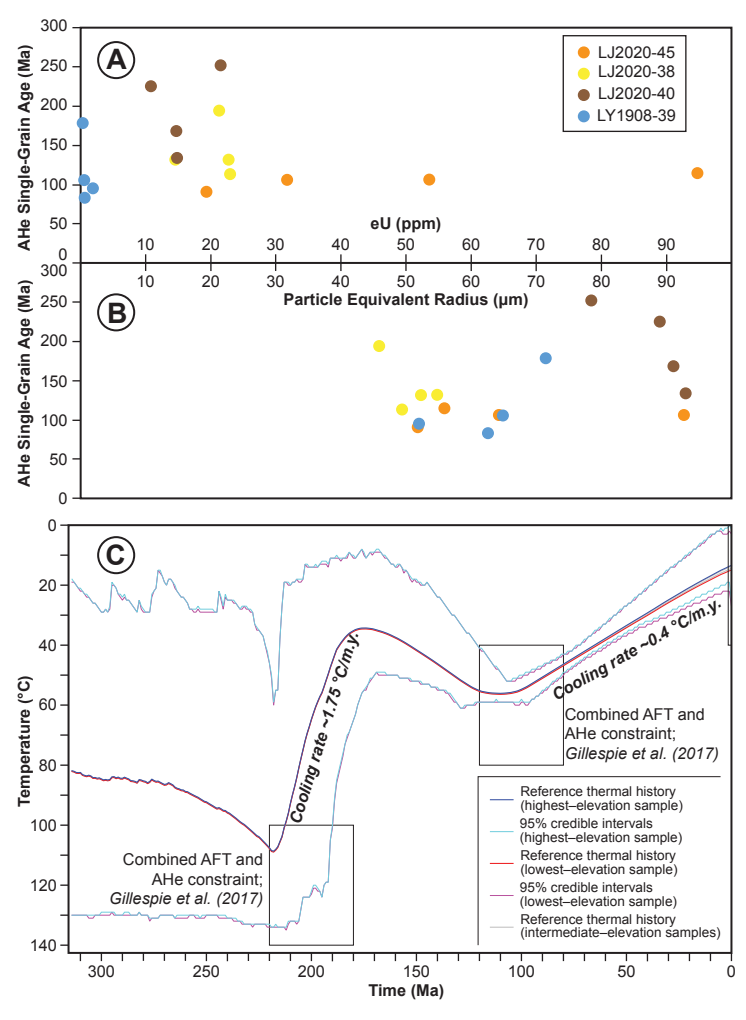


Figure 18. (A) Plot of apatite (U-Th)/He thermochronology (AHe) ages versus effective uranium concentration (eU); each point represents single grain aliquot. (B) Plot of AHe ages versus equivalent radius of apatite grains that is half of the distance across the hexagonal prism. (C) AHe thermal history model output representing average of all models sampled. Model was computed using QTQt software (Gallagher, 2012). AFT—apatite fission-track.

for AHe were used to constrain the temperature-time path (Gleadow and Duddy, 1981). In the modeling, we used the radiation damage accumulation and annealing model RDAAM of Flowers et al. (2009). Thermal history model inputs are listed in Table 5. Because there is no record of regional magmatism and/or hydrothermal activity since the Jurassic, the cooling history can

be linked with the regional exhumation history. For the modeling, all the preset constraints are given large uncertainties to give the modeling sufficient freedom to search for viable thermal histories based on available data. See Gallagher (2012) for details regarding the thermal modeling approach. Under the preset constraints, the final modeling results display similar thermal histories when the temperature and time ranges are adjusted for all samples or single samples (Fig. S2 [see footnote 1]). Results of thermal history modeling (Fig. 18C) show three distinct cooling and heating phases: (1) a late Triassic to early Jurassic (ca. 220–180 Ma) relatively rapid phase that occurred at a rate of ~1.75 °C/m.y.; (2) a middle Jurassic to early Cretaceous (ca. 180–120 Ma) reheating phase; and (3) and a late Cretaceous to present (≤100 Ma) phase of protracted cooling at a rate of ~0.4 °C/m.y.

DISCUSSION

Tectonic Setting of the HP Metamorphic Rocks

Key timing constraints on the formation and exhumation of the HP rocks are obtained according to our new and previous chronological results. The HP rocks retain clear traces of Mesoproterozoic (ca. 1.55-1.36 Ga; such as samples LJ2020-8, LJ2020-33, LJ2020-39, and LJ2020-40) Beishan basement origin, which may be related to Mesoproterozoic magmatism across the southern Central Asian Orogenic System (He et al., 2015; Yuan et al., 2019; Li et al., 2022). In addition, early Neoproterozoic (ca. 1024-866 Ma) magmatism is preserved in the South Beishan orogen (Liu et al., 2015; Yuan et al., 2015; Soldner et al., 2020a) based on protolith ages of the HP rocks and the surrounding rocks (e.g., samples LJ2020-33, LY1908-17-1, LY1908-26, and LY1908-93) (Saktura et al., 2017; Soldner et al., 2020b; de Vries et al., 2022). Amphibolite- to eclogite-facies metamorphism occurred in the South Beishan orogen during the Cambrian-Ordovician (ca. 512-453 Ma; samples LJ2020-33, LJ2020-39, and LJ2020-40), including peak metamorphism ca. 465 Ma (Mei et al., 1999a; Yu et al., 1999; Yang et al., 2006; Liu et al., 2011; Qu et al., 2011; Saktura et al., 2017; Soldner et al., 2020b; de Vries et al., 2022). The South Beishan orogen experienced extension-related magmatism during the Ordovician-Silurian based on the widespread occurrence of arc magmatic rocks and (ultra)mafic intrusions (Li et al., 2022). The presence of an undeformed granitic pluton (ca. 438 Ma) and granitic dikes (ca. 424-410 Ma) that intrude the HP rocks suggests that deformation and metamorphism of the HP rocks and adjacent wall-rock unit occurred earlier than the petrogenesis of the granitoids and veins (Liu et al., 2011; Saktura et al., 2017; this study). The HP rocks and wall-rock unit were exhumed to mid-crustal levels ca. 428.9 Ma based on a biotite 40Ar/39Ar age (Qu et al., 2011).

Our field observations and results of geo- and thermochronology combined with previous constraints show that the Liuyuan HP metamorphic unit of the South Beishan orogen originated as a mixture of continental crust and mafic materials without oceanic fragments (Fig. 7). Silurian (ultra)mafic rocks in the study area are composed of gabbro, pyroxenite, peridotite, and serpentinite

TABLE 5. THERMAL HISTORY	MODEL INPLIT FOR	SIMILI ATIONS OF THE	ΔPATITE (I I-Th)/Ha	(AHe) DATA

Apatite (U-Th)/He data	
Samples and data used in simulations	
Data type	Data source
AHe single grain ages, U, Th, and He contents. and individual shape parameters	This study (Table 4)
Treatment: All samples were input in QTQt software (Gallagher, 2012) as an integral to simulate the thermal history	
Additional geologic information	
Assumption	Explanation and source
Initial condition begins at high temperature of 100–140 °C at 180–220 Ma	Available AHe data indicated complete apatite annealing at this high temperature range, and previous apatite fission-track thermal histories indicate a reasonable time range (Gillespie et al., 2017).
AHe ages were set through the temperature range of 40–80 °C at 80–120 Ma	Previous AHe ages and apatite fission-track thermal histories give preliminary temperature and time constraints (Gillespie et al., 2017).
At surface temperature of 20 ± 20 °C by 0 Ma	Average surface temperature is an end-member minimum estimate.

ultramafic rocks and intrude surrounding rocks (Fig. 5), so these (ultra)mafic rocks are considered to be a product of later crustal extension and not part of an ophiolitic mélange (Li et al., 2022). These rocks may have been emplaced in the continental crust with arc-magmatic activity, as evidenced by the exposure of Neoproterozoic crystalline rocks and widespread early Paleozoic arc-related rocks (Fig. 5). Published P-T results show that the HP rocks experienced peak temperatures and pressures of ~700-800 °C and ~1.6-2.1 GPa (>60 km depth), respectively (Fig. 19) (Mei et al., 1999a; Yu et al., 1999; Liu et al., 2002; Qu et al., 2011; Soldner et al., 2020b). Peak HP metamorphism occurred at ca. 465 Ma (Liu et al., 2011; Qu et al., 2011; Soldner et al., 2020b), which is older than the timing of regional arc magmatism (ca. 440-350 Ma) across the Beishan orogen (Li et al., 2022). The time interval between protolith formation (ca. 1000-800 Ma) and peak metamorphism (ca. 465 Ma) of the HP rocks is more than 400 m.y. Subsequent exhumation of the HP rocks to mid-crustal depths of ~10-15 km was relatively slow with cooling rates of ~11 °C/m.y. over a time span of >10 m.y. (Fig. 19) (Liu et al., 2011; Qu et al., 2011; Soldner et al., 2020b). Protracted cooling of the HP rocks occurred over hundreds of millions of years at mid-crustal depths (Fig. 19). The exposed contact between the HP unit and lower-grade metamorphic wall rocks is represented by the D₂ detachment fault that is isoclinally folded.

Based on these findings, we discuss the tectonic setting of metamorphism and subsequent exhumation of the Liuyuan HP rocks according to the predictions of existing tectonic models for the HP metamorphism (Fig. 1; Table 1). First, our results are inconsistent with the oceanic subduction model, which predicts HP metamorphism coeval with arc magmatism, the occurrence of

oceanic materials, an interval between protolith and peak metamorphism ages no greater than 200 m.y., and relatively low-temperature peak metamorphic conditions (England and Holland, 1979; Song et al., 2015; Zhang and Wang, 2020). None of these predictions match our observations for the South Beishan HP metamorphic rocks. Second, our results are inconsistent with the channel flow and wedge extrusion sub-models for continental subduction, which predict a duration of a few million years for exhumation of the HP metamorphic rocks to the near surface (Chemenda et al., 1995, 1996, 1997; Ernst and Liou, 1995; Jolivet et al., 2005; Ring et al., 2007; Wang et al., 2014a, 2018a; Feng et al., 2021). Finally, we rule out the diapiric ascent, thrust stacking, and pure-shear thickening sub-models for continental subduction, as these models are inconsistent with our observations of the tectonic contact between HP metamorphic rocks and low-grade mid-crustal rocks (Okay and Şengör, 1992; Dewey et al., 1993; Nie et al., 1994; Hacker et al., 2005).

Instead, our results suggest that the metamorphism and exhumation of the HP rocks of the South Beishan orogen may have been related to continental collision and subsequent crustal extension (Fig. 20) (e.g., Avigad and Garfunkel, 1991; Fassoulas et al., 1994; Bond et al., 2007). The continent-continent collision model for the petrogenesis of the HP rocks coincides with trends of paleo–crustal thickness over time and the occurrence of deformed and metamorphosed HP and surrounding rocks (Fig. 20A) (Li et al., 2022). The exhumation of the HP rocks is consistent with previous findings regarding the paleo–crustal thickness variations of the Beishan orogen, which thinned from >60 km to ~40 km after ca. 450 Ma (Li et al., 2022), and the deposition of extension-related Late Ordovician–Silurian bimodal volcano-sedimentary

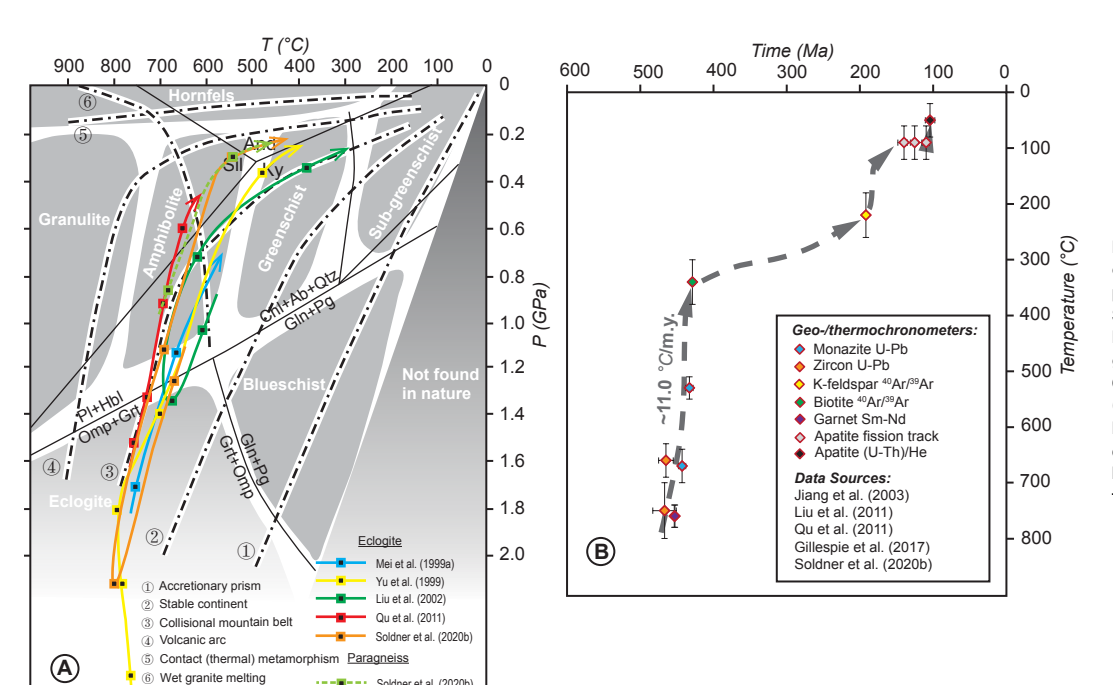


Figure 19. (A) Pressure-temperature (P-T) paths of high-pressure (HP) metamorphic rocks exposed in Gubaoquan region. And-andalusite; Sil-sillimanite: Kv-kvanite: Pl-plagioclase: Hbl-hornblende; Omp-omphacite; Grtgarnet; Gln-glaucophane; Pg-paragonite; Chl-chlorite; Ab-albite; Qtz-quartz. (B) Temperature-time path of HP rocks. Horizontal error bars of age data represent uncertainties of measured ages, and vertical error bars represent closure temperatures of different thermochronometers adopted by these samples.

deposits (Gansu BGMR, 1997) (Fig. 20B). This crustal extension and thinning event may be the result of the northward rollback of the subducted south-dipping Paleo-Asian oceanic slab, which is supported by the widespread distribution of arc-type granitic and extension-related (ultra)mafic intrusions throughout the South Beishan orogen (Fig. 20B) (Li et al., 2022).

--- Soldner et al. (2020b)

Emplacement and Exhumation Histories of the HP Metamorphic Rocks

We observed high-grade, eclogite-bearing metamorphic rocks juxtaposed against low-grade mylonitic granitoid, which, combined with geo- and thermochronological results and previous constraints (Table 6), allowed us to develop a tectonic model for the emplacement and exhumation histories of the Liuyuan HP rocks (Fig. 21). First, regional north-south-oriented contraction generated the D_1 structures in the middle crust ca. 500–450 Ma (Table 6; Fig. 21A), including S₁ penetrative foliation in Neoproterozoic mylonitic granitoid (Fig. 8). D₁ deformation occurred at temperatures of ~300-400 °C. This contraction also resulted in metamorphism of the HP unit in the deep crust that was >60 km crustal thickness at the time. Neoproterozoic mafic rocks that intruded the crust were metamorphosed ca. 470-450 Ma at amphibolite- to eclogite-facies conditions of >700 °C and >1.2 GPa (Fig. 19).

Exhumation of the HP rocks occurred following the ca. 450 Ma transition from regional contraction to extension (Li et al., 2022). Regional lithospheric extension in the South Beishan orogen controlled the mid-crustal emplacement of high-grade metamorphic rocks, development of D₂ structures, and intrusion of granitic dikes and arc-related granitoids. D₂ extensional structures include a regional, southeast-dipping detachment shear zone (Fig. 21B) with low-grade and deformed Neoproterozoic mylonitic granitoid in its hanging wall (Ye et al., 2013; Liu et al., 2015; Yuan et al., 2015; Zong et al., 2017; Soldner et al., 2020a; Li et al., 2022). HP rocks in the footwall of the detachment shear zone were exhumed during normal-sense slip after ca. 450 Ma (Fig. 21B). Slip along the detachment shear zone in the middle crust occurred at temperatures of ~500-600 °C. Crustal thinning and lower-crustal flow resulted in heat advection, partial melting, and intrusion of granitic dikes during footwall exhumation after ca. 450 Ma. Some lag time likely occurred between the onset of extension and lower-crustal flow and partial melting (Saktura et al., 2017; this study). D₃ structures recorded in the South Beishan orogen may be a late-stage response to exhumation.

Following exhumation of the HP rocks to mid-crustal levels, regional north-south-oriented contraction folded previous structures including the detachment shear zone (Fig. 21C). This contraction occurred before ca. 438 Ma based on the crystallization age of an undeformed granitoid intrusion that

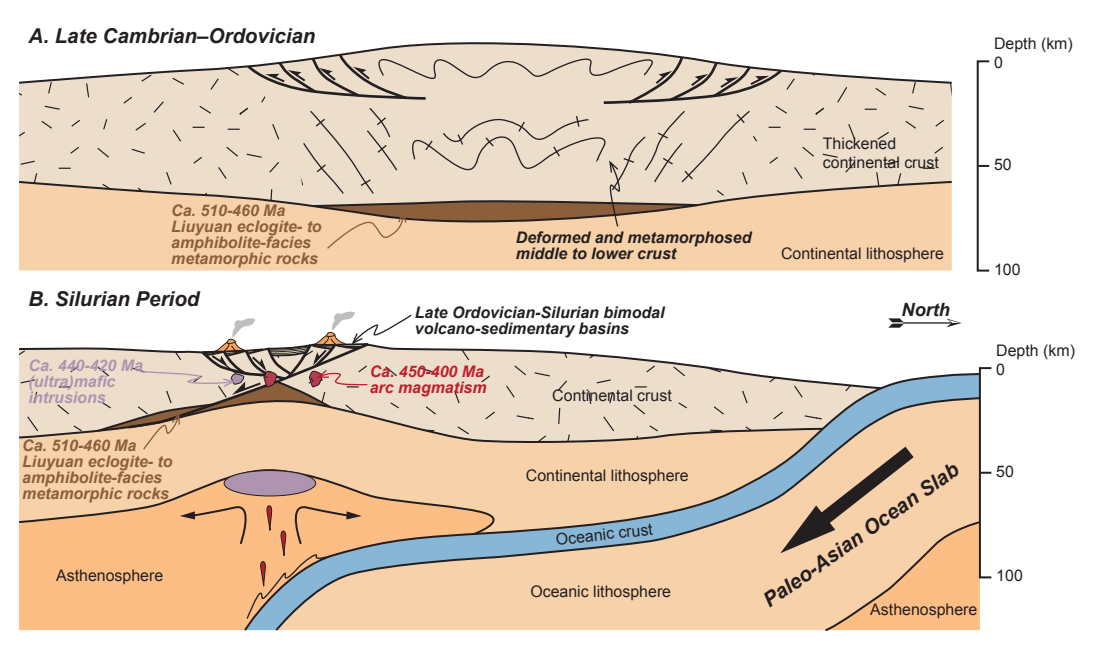


Figure 20. (A) Tectonic model for formation of high-pressure (HP) rocks during continent-continent collision. (B) Tectonic model for Liuyuan HP rocks exhumed from deep to midcrustal depths.

crosscuts older structures (Liu et al., 2011). Folds associated with this contractional phase are east-west trending and open to isoclinal and highlighted by north-dipping isoclinal-folded limbs of the older detachment shear zone (Fig. 6). Contraction was coeval with the emplacement of ca. 445–421 Ma plutons (Liu et al., 2011; Mao et al., 2012a; Li et al., 2015; Zhu et al., 2016; Wang et al., 2017) in the Liuyuan area (Fig. 5), which would have increased crustal buoyancy and promoted isostatic doming.

Following ca. 430 Ma, the Liuyuan HP rocks resided in the middle to upper crust until ca. 200 Ma (Figs. 19B and 18C) when rapid Late Triassic to Early Jurassic cooling occurred from ~100 to 40 °C at a rate of ~1.75 °C/m.y. within ~40 m.y.

(Fig. 18C). This cooling episode is interpreted to be related to hanging-wall exhumation during thrusting, possibly associated with Mesozoic closure of the Tethyan and Paleo-Asian Ocean domains (Zheng et al., 1996; Yin and Harrison, 2000). Subsequent Middle Jurassic to Early Cretaceous reheating (Fig. 18C) may have been related to Cretaceous extension in northern Tibet and the northern North China craton (Davis et al., 2001, 2002; Yang et al., 2021b; Wang et al., 2022). Following this reheating phase, the Liuyuan HP rocks experienced protracted cooling and exhumation at a rate of ~0.4 °C/m.y., which reflects an absence of major tectonic activity in the South Beishan orogen, coupled with minimal precipitation and erosion (e.g., Jepson et al., 2021) since ca. 100 Ma.

TABLE 6. SUMMARY OF KEY TIMING CONSTRAINTS, DEFORMATION FABRICS, INFERRED STRAIN TEMPERATURES, AND INTERPRETED TECTONIC EVENTS AFFECTING THE EMPLACEMENT OF THE HIGH-PRESSURE (HP) METAMORPHIC ROCKS

Timing constraints	Temperature	Deformation		Inferred events	Representative figures and samples	
		Micro-observations	Field	Shear sense		
			observations			
Ca. 500-450 Ma	~300–400 °C	Quartz SGR; feldspar brittle	D ₁	Top-up-S shear	S-N contraction and crust thickening	Figs. 8, 14, and 15; sample LY1908-60
After ca. 450 Ma	~500–600 °C	Quartz GBM; feldspar BLG	D_2	Top-up-S shear	NW-SE extension and emplacement of the HP rocks	Figs. 9, 14, and 15; sample LY1908-47
	~400–450 °C	Quartz SGR	D_3	Top-down-N shear		Figs. 10, 14I, and 15I; sample LY1908-16
Older than 438 Ma	>300 °C	Quartz ductile	D_4	E-trending folding	S-N contraction and regional folding	Figs. 6 and 11

Note: BLG-bulging recrystallization; SGR-subgrain rotation recrystallization; GBM-grain boundary migration recrystallization. D₁-D₄—four identified episodes deformation structures in field outcrops.

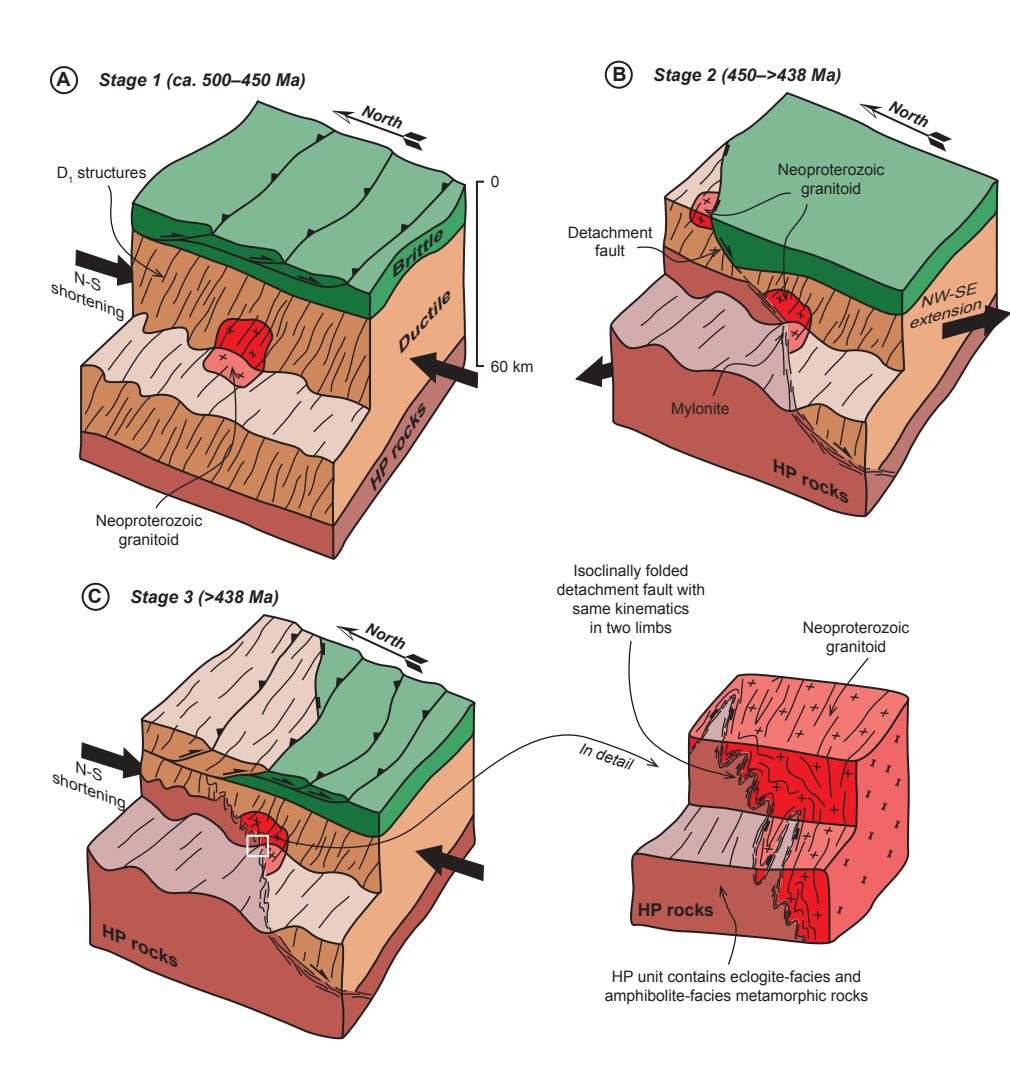


Figure 21. Proposed structural interpretation for emplacement of Liuyuan high-pressure (HP) metamorphic rocks at >60 km depth and subsequent exhumation to midcrustal depths.

Generally, surface uplift and erosion moving rocks laterally away from the uplift axis provide a means of bringing the HP assemblages to their final exposure, which may be the dominant exhumation mechanism in mountain belts where convergence has ceased (Duchêne et al., 1997).

CONCLUSIONS

New structural and geo- and thermochronological data from the South Beishan orogen has led to the following key findings:

- (1) Zircon grains from Neoproterozoic metamorphic rocks yield crystallization ages of ca. 1.55–1.36 Ga, which suggest that Mesoproterozoic basement occurs in the South Beishan orogen.
- (2) The South Beishan orogen experienced early Neoproterozoic (ca. 970–866 Ma) tectono-magmatism, which suggests that Himalayan-style tectonic activity occurred along the southern margin of the Central Asian Orogenic System.
- (3) Early Paleozoic (ca. 500–450 Ma) Liuyuan HP rocks in the South Beishan orogen experienced eclogite- to amphibolite-facies metamorphism in thickened continental crust (>60 km thick) based on peak P-T conditions, exhumation

- and cooling rates, residence time in the middle crust, metamorphic rock assemblages, time between protolith formation and peak metamorphism, and temporal-spatial relationships with recorded arc magmatism.
- (4) Three deformation events controlled metamorphism and exhumation of the Liuyuan HP metamorphic rocks. First, north-south-oriented crustal shortening resulted in ca. 500-450 Ma burial and metamorphism of the HP rocks. Second, northwest-southeast-oriented lithospheric extension resulted in exhumation of the HP rocks in the footwall of a regional detachment shear zone from the deep crust (>60 km depth) to the middle crust after ca. 450 Ma. Lastly, north-south-oriented shortening before ca. 438 Ma folded older structures including the detachment shear zone.
- (5) Middle Mesozoic contraction in the South Beishan orogen may have been related to the closure of the Tethyan and Paleo-Asian Ocean domains. A subsequent late Mesozoic crustal extension may have induced further exhumation of the HP rocks.

ACKNOWLEDGMENTS

We greatly appreciate editorial handing by Editor Andrea Hampel. Constructive comments from the Associate Editor Jason W. Ricketts and three anonymous reviewers greatly improved this paper. This research was supported by grants from the Second Tibetan Plateau Scientific Expedition and Research Program (grant 2019QZKK0708), the China Geological Survey (grants DD20160083 and DD20190011), the Basic Science Center for Tibetan Plateau Earth System (grant 41988101-01), and the Tectonics Program of the U.S. National Science Foundation (EAR-1914503 and EAR-2210074). Ye Wang and Hongxu Chen from the Chinese Academy of Geological Sciences are thanked for their assistance in the field. Chunru Hou from China University of Geosciences (Beijing) and Yiping Zhang, Maohui Ge, Heng Zhao, and Beihang Zhang from the Chinese Academy of Geological Sciences are acknowledged for experimental assistance. We are grateful to Dr. Yahui Yue for her assistance with zircon U-Pb analysis.

REFERENCES CITED

- Agard, P., Yamato, P., Jolivet, L., and Burov, E., 2009, Exhumation of oceanic blueschists and eclogites in subduction zones: Timing and mechanisms: Earth-Science Reviews, v. 92, p. 53-79, https://doi.org/10.1016/i.earscirev.2008.11.002.
- Andersen, T., 2002, Correction of common lead in U-Pb analyses that do not report 204Pb: Chemical Geology, v. 192, p. 59-79, https://doi.org/10.1016/S0009-2541(02)00195-X.
- Avigad, D., and Garfunkel, Z., 1991, Uplift and exhumation of high-pressure metamorphic terrains: The example of the Cycladic blueschist belt (Aegean Sea): Tectonophysics, v. 188, p. 357-372, https://doi.org/10.1016/0040-1951(91)90464-4.
- Baziotis, I., Proyer, A., Mposkos, E., Windley, B.F., and Boukouvala, I., 2019, Exhumation of the high-pressure northwestern Cyclades, Aegean: New P-T constraints, and geodynamic evolution: Lithos, v. 324-325, p. 439-453, https://doi.org/10.1016/j.lithos.2018.11.027.
- Beane, R.J., and Connelly, J.N., 2000, 40Ar/39Ar, U-Pb, and Sm-Nd constraints on the timing of metamorphic events in the Maksyutov Complex, southern Ural Mountains: Journal of the Geological Society, v. 157, p. 811-822, https://doi.org/10.1144/jgs.157.4.811.
- Bond, C.E., Butler, R.W.H., and Dixon, J.E., 2007, Co-axial horizontal stretching within extending orogens: The exhumation of HP rocks on Syros (Cyclades) revisited, in Ries, A.C., Butler, R.W.H., and Graham, R.H., eds., Deformation of the Continental Crust: The Legacy of Mike Coward: Geological Society of London Special Publication 272, p. 203-222, https://doi.org/10.1144 /GSL.SP.2007.272.01.12.
- Boutelier, D., Chemenda, A., and Jorand, C., 2004, Continental subduction and exhumation of high-pressure rocks: Insights from thermo-mechanical laboratory modelling: Earth and Planetary Science Letters, v. 222, p. 209-216, https://doi.org/10.1016/j.epsl.2004.02.013.

- Boyce, J.W., Hodges, K.V., Olszewski, W.J., Jercinovic, M.J., Carpenter, B.D., and Reiners, P.W., 2006, Laser microprobe (U-Th)/He geochronology: Geochimica et Cosmochimica Acta, v. 70, p. 3031-3039, https://doi.org/10.1016/j.gca.2006.03.019.
- Briggs, S.M., Yin, A., Manning, C.E., Chen, Z.L., Wang, X.F., and Grove, M., 2007, Late Paleozoic tectonic history of the Ertix Fault in the Chinese Altai and its implications for the development of the Central Asian Orogenic System: Geological Society of America Bulletin, v. 119, p. 944-960, https://doi.org/10.1130/B26044.1.
- Briggs, S.M., Yin, A., Manning, C.E., Chen, Z.L., and Wang, X.F., 2009, Tectonic development of the southern Chinese Altai Range as determined by structural geology, thermobarometry, ⁴⁰Ar/³⁹Ar thermochronology, and Th/Pb ion-microprobe monazite geochronology: Geological Society of America Bulletin, v. 121, p. 1381-1393, https://doi.org/10.1130/B26385.1.
- Brun, J.-P., and Faccenna, C., 2008, Exhumation of high-pressure rocks driven by slab rollback: Earth and Planetary Science Letters, v. 272, p. 1-7, https://doi.org/10.1016/j.epsl.2008.02.038.
- Burov, E., Francois, T., Yamato, P., and Wolf, S., 2014, Mechanisms of continental subduction and exhumation of HP and UHP rocks; Gondwana Research, v. 25, p. 464-493, https://doi .org/10.1016/j.gr.2012.09.010.
- Buslov, M.M., Watanabe, T., Saphonova, I.Y., Iwata, K., Travin, A., and Akiyama, M., 2002, A Vendian-Cambrian island arc system of the Siberian continents in Gorny Altai (Russia, Central Asia): Gondwana Research, v. 5, p. 781-800, https://doi.org/10.1016/S1342-937X(05)70913-8.
- Butler, J.P., Beaumont, C., and Jamieson, R.A., 2013, The Alps 1: A working geodynamic model for burial and exhumation of (ultra)high-pressure rocks in Alpine-type orogens: Earth and Planetary Science Letters, v. 377-378, p. 114-131, https://doi.org/10.1016/j.epsl.2013.06.039.
- Chatzaras, V., Xypolias, P., and Doutsos, T., 2006, Exhumation of high-pressure rocks under continuous compression: A working hypothesis for the southern Hellenides (central Crete, Greece): Geological Magazine, v. 143, p. 859-876, https://doi.org/10.1017/S0016756806002585.
- Chemenda, A.I., Mattauer, M., Malavieille, J., and Bokun, A.N., 1995, A mechanism for syn-collisional rock exhumation and associated normal faulting: Results from physical modelling: Earth and Planetary Science Letters, v. 132, p. 225-232, https://doi.org/10.1016/0012-821X(95)00042-B.
- Chemenda, A.I., Mattauer, M., and Bokun, A.N., 1996, Continental subduction and a mechanism for exhumation of high-pressure metamorphic rocks; New modelling and field data from Oman: Earth and Planetary Science Letters, v. 143, p. 173-182, https://doi.org/10.1016/0012 -821X(96)00123-9.
- Chemenda, A., Matte, P., and Sokolov, V., 1997, A model of Palaeozoic obduction and exhumation of high-pressure/low-temperature rocks in the southern Urals: Tectonophysics, v. 276, p. 217-227. https://doi.org/10.1016/S0040-1951(97)00057-7.
- Chen, C., Xiu, D., Pan, Z.L., Zhang, H., Zhang, J.L., Li, Q.Z., and Zhuan, S.P., 2017, Early Paleozoic crustal extensional tectonic regime in the central part of Beishan orogenic belt: New evidence from geochronology and geochemistry of gabbro in Shibanjing: Acta Geologica Sinica, v. 91, no. 8, p. 1661-1673 (in Chinese with English abstract).
- Chen, J.P., Liao, Q.A., Luo, T., Zhang, X.H., Guo, D.B., Zhu, H.L., and Liu, X.M., 2013, Zircon U-Pb geochronology and genesis study on the mafic complex from diabase-type iron deposit in Cihai, Beishan area: Geological Science and Technology Information, v. 32, no. 4, p. 76-83 (in Chinese with English abstract).
- Chen, S., Guo, Z.J., Qi, J.F., Zhang, Y.Y., Pe-Piper, G., and Piper, D.J.W., 2016, Early Permian volcano-sedimentary successions, Beishan, NW China; Peperites demonstrate an evolving rift basin: Journal of Volcanology and Geothermal Research, v. 309, p. 31-44, https://doi .org/10.1016/j.jvolgeores.2015.11.004.
- Chen, X.H., Dong, S.W., Shi, W., Ding, W.C., Zhang, Y.P., Li, B., Shao, Z.G., and Wang, Y., 2022, Construction of the continental Asia in Phanerozoic: A review: Acta Geologica Sinica (English edition), v. 96, p. 26-51, https://doi.org/10.1111/1755-6724.14867.
- Chopin, C., 1984, Coesite and pure pyrope in high-grade blueschists of the Western Alps: A first record and some consequences: Contributions to Mineralogy and Petrology, v. 86, p. 107-118, https://doi.org/10.1007/BF00381838.
- Cleven, N., Lin, S.F., Guilmette, C., Xiao, W.J., and Davis, B., 2015, Petrogenesis and implications for tectonic setting of Cambrian suprasubduction-zone ophiolitic rocks in the central Beishan orogenic collage, Northwest China: Journal of Asian Earth Sciences, v. 113, p. 369-390, https:// doi.org/10.1016/j.jseaes.2014.10.038.
- Cleven, N.R., Lin, S.F., Xiao, W.J., Davis, D.W., and Davis, B., 2018, Successive arc accretion in the southern Central Asian orogenic belt, NW China: Evidence from two Paleozoic arcs with offset magmatic periods: Geological Society of America Bulletin, v. 130, p. 537-557, https:// doi.org/10.1130/B31434.1.

- Cloos, M., and Shreve, R.L., 1988, Subduction-channel model of prism accretion, mélange formation, sediment subduction, and subduction erosion at convergent plate margins: 1. Background and description: Pure and Applied Geophysics, v. 128, p. 455–500, https://doi.org/10.1007//BF00874548
- Cunningham, D., 2013, Mountain building processes in intracontinental oblique deformation belts: Lessons from the Gobi Corridor, Central Asia: Journal of Structural Geology, v. 46, p. 255–282, https://doi.org/10.1016/j.jsg.2012.08.010.
- Davies, J.H., and von Blanckenburg, F., 1995, Slab breakoff: A model of lithosphere detachment and its test in the magmatism and deformation of collisional orogens: Earth and Planetary Science Letters, v. 129, p. 85–102, https://doi.org/10.1016/0012-821X(94)00237-S.
- Davis, G.A., Zheng, Y.D., Wang, C., Darby, B.J., Zhang, C.H., and Gehrels, G., 2001, Mesozoic tectonic evolution of the Yanshan fold and thrust belt, with emphasis on Hebei and Liaoning provinces, northern China, in Hendrix, M.S., and Davis, G.A., eds., Paleozoic and Mesozoic Tectonic Evolution of Central and Eastern Asia: From Continental Assembly to Intracontinental Deformation: Geological Society of America Memoir 194, p. 171–197, https://doi.org/10.1130 /0-8137-1194-0.171.
- Davis, G.A., Darby, B.J., Zheng, Y.D., and Spell, T.L., 2002, Geometric and temporal evolution of an extensional detachment fault, Hohhot metamorphic core complex, Inner Mongolia, China: Geology, v. 30, p. 1003–1006, https://doi.org/10.1130/0091-7613(2002)030<1003 :GATEOA>2.0.CO;2.
- de Vries, J., Lin, S.F., van Staal, C., and Yakymchuk, C., 2022, A structural-metamorphic study of the Gubaoquan eclogites and enveloping rock units in the Beishan Orogenic Collage, NW China, with emphasis on the structural evolution, nature of juxtaposition and exhumation: International Journal of Earth Sciences, v. 111, p. 2603–2632, https://doi.org/10.1007/s00531 -022-02192-3.
- Dewey, J.F., Ryan, P.D., and Andersen, T.B., 1993, Orogenic uplift and collapse, crustal thickness, fabrics and metamorphic phase changes: The role of eclogites, in Prichard, H.M., Alabaster, T., Harris, N.B.W., and Neary, C.R. eds., Magmatic Processes and Plate Tectonics: Geological Society of London Special Publication 76, p. 325–343, https://doi.org/10.1144/GSL.SP.1993.076.01.16.
- Ding, W.C., Li, T.D., Chen, X.H., Chen, J.P., Xu, S.L., Zhang, Y.P., Li, B., and Yang, Q., 2020, Intracontinental deformation and tectonic evolution of the West Junggar Orogenic Belt, Central Asia: Evidence from remote sensing and structural geological analyses: Geoscience Frontiers, v. 11, p. 651–663, https://doi.org/10.1016/j.gsf.2019.08.001.
- Dobretsov, N.L., and Buslov, M.M., 2004, Serpentinitic mélanges associated with HP and UHP rocks in Central Asia: International Geology Review, v. 46, p. 957–980, https://doi.org/10.2747/0020 -6814.46.11.957.
- Duchêne, S., Lardeaux, J.-M., and Albarède, F., 1997, Exhumation of eclogites: Insights from depth-time path analysis: Tectonophysics, v. 280, p. 125–140, https://doi.org/10.1016/S0040 -1951(97)00143-1.
- Dumitru, T.A., and Hendrix, M.S., 2001, Fission-track constraints on Jurassic folding and thrusting in southern Mongolia and their relationship to the Beishan thrust belt of northern China, in Hendrix, M.S., and Davis, G.A., eds., Paleozoic and Mesozoic Tectonic Evolution of Central and Eastern Asia: From Continental Assembly to Intracontinental Deformation: Geological Society of America Memoir 194, p. 215–229, https://doi.org/10.1130/0-8137-1194-0.215.
- Eide, E.A., 1995, A model for the tectonic history of HP and UHPM regions in east central China, in Coleman, R.G., and Wang, X.M., eds., Ultrahigh Pressure Metamorphism: Cambridge, UK, Cambridge University Press, p. 391–426, https://doi.org/10.1017/CB09780511573088.012.
- England, P.C., and Holland, T.J.B., 1979, Archimedes and the Tauern eclogites: The role of buoyancy in the preservation of exotic eclogite blocks: Earth and Planetary Science Letters, v. 44, p. 287–294, https://doi.org/10.1016/0012-821X(79)90177-8.
- Erdman, M.E., and Lee, C.-T.A., 2014, Oceanic- and continental-type metamorphic terranes: Occurrence and exhumation mechanisms: Earth-Science Reviews, v. 139, p. 33–46, https://doi.org/10.1016/j.earscirev.2014.08.012.
- Ernst, W.G., 1999, Metamorphism, partial preservation, and exhumation of ultrahigh-pressure belts: Island Arc, v. 8, p. 125–153, https://doi.org/10.1046/j.1440-1738.1999.00227.x.
- Ernst, W.G., and Liou, J.G., 1995, Contrasting plate-tectonic styles of the Qinling-Dabie-Sulu and Franciscan metamorphic belts: Geology, v. 23, p. 353–356, https://doi.org/10.1130/0091-7613 (1995)023<0353:CPTSOT>2.3.CO;2.
- Farley, K.A., 2002, (U-Th)/He dating: Techniques, calibrations, and applications: Reviews in Mineralogy and Geochemistry, v. 47, p. 819–844, https://doi.org/10.2138/rmg.2002.47.18.

- Farley, K.A., and Stockli, D.F., 2002, (U-Th)/He dating of phosphates: Apatite, monazite, and xenotime: Reviews in Mineralogy and Geochemistry, v. 48, p. 559–577, https://doi.org/10.2138 /rmg.2002.48.15.
- Farley, K.A., Wolf, R.A., and Silver, L.T., 1996, The effects of long alpha-stopping distances on (U-Th)/He ages: Geochimica et Cosmochimica Acta, v. 60, p. 4223–4229, https://doi.org/10.1016/S0016-7037/96100193-7.
- Fassoulas, C., Kilias, A., and Mountrakis, D., 1994, Postnappe stacking extension and exhumation of high-pressure/low-temperature rocks in the island of Crete, Greece: Tectonics, v. 13, p. 127–138, https://doi.org/10.1029/93TC01955.
- Feng, P., Wang, L., Brown, M., Johnson, T.E., Kylander-Clark, A., and Piccoli, P.M., 2021, Partial melting of ultrahigh-pressure eclogite by omphacite-breakdown facilitate drive exhumation of deeply-subducted crust: Earth and Planetary Science Letters, v. 554, 116664, https://doi .org/10.1016/j.epsl.2020.116664.
- Flowers, R.M., and Kelley, S.A., 2011, Interpreting data dispersion and "inverted" dates in apatite (U-Th)/He and fission-track datasets: An example from the US midcontinent: Geochimica et Cosmochimica Acta, v. 75, p. 5169–5186, https://doi.org/10.1016/j.gca.2011.06.016.
- Flowers, R.M., Ketcham, R.A., Shuster, D.L., and Farley, K.A., 2009, Apatite (U-Th)/He thermochronometry using a radiation damage accumulation and annealing model: Geochimica et Cosmochimica Acta, v. 73, p. 2347–2365, https://doi.org/10.1016/j.gca.2009.01.015.
- Gallagher, K., 2012, Transdimensional inverse thermal history modelling for quantitative thermochronology: Journal of Geophysical Research, v. 117, B02408, https://doi.org/10 .1029/2011JB008825.
- Gansu BGMR (Gansu Bureau of Geology and Mineral Resources), 1989, Regional geology of Gansu Province: Beijing, China, Geological Publishing House (in Chinese with brief English introduction), 692 p.
- Gansu BGMR (Gansu Bureau of Geology and Mineral Resources), 1997, Stratigraphy (lithostratic) of Gansu Province: Wuhan, China University of Geosciences Press (in Chinese), 314 p.
- Gao, F., Jian, K.K., Li, N., Du, B., Zhao, D.C., and Yi, P.F., 2018a, Zircon U-Pb dating and geochemistry of Jijiquan pluton in the eastern section of Beishan orogenic belt and their tectonic implications: Northwestern Geology, v. 51, no. 3, p. 26–37 (in Chinese with English abstract).
- Gao, F., Jian, K.K., He, Y.F., Li, N., Yi, P.F., Liu, X.W., and Tang, L., 2018b, Genesis and metallogenic epoch constraints of Luzuizi antimony deposit of Beishan, Inner Mongolia: Mineral Exploration, v. 9, no. 9, p. 1644–1654 (in Chinese with English abstract).
- Gao, J., and Klemd, R., 2003, Formation of HP-LT rocks and their tectonic implications in the western Tianshan orogen, NW China: Geochemical and age constraints: Lithos, v. 66, p. 1–22, https://doi.org/10.1016/S0024-4937(02)00153-6.
- Gao, W.B., Qian, Z.Z., Xu, G., Duan, J., Shi, Z., Ma, B.P., and Yang, T., 2020, Geochemical characteristics of Gubaoquan dolerite dykes in Beishan area of Gansu, China and their geological significance: Journal of Earth Sciences and Environment, v. 42, no. 5, p. 622–636 (in Chinese with English abstract).
- Gautheron, C., Tassan-Got, L., Barbarand, J., and Pagel, M., 2009, Effect of alpha-damage annealing on apatite (U-Th)/He thermochronology: Chemical Geology, v. 266, p. 157–170, https://doi.org/10.1016/j.chemgeo.2009.06.001.
- Gerya, T.V., Stöckhert, B., and Perchuk, A.L., 2002, Exhumation of high-pressure metamorphic rocks in a subduction channel: A numerical simulation: Tectonics, v. 21, 1056, https://doi.org/10.1029/2002TC001406.
- Gillespie, J., Glorie, S., Xiao, W.J., Zhang, Z.Y., Collins, A.S., Evans, N., McInner, B., and De Grave, J., 2017, Mesozoic reactivation of the Beishan, southern Central Asian Orogenic Belt: Insights from low-temperature thermochronology: Gondwana Research, v. 43, p. 107–122, https://doi.org/10.1016/j.gr.2015.10.004.
- Gilotti, J.A., and Krogh Ravna, E.J., 2002, First evidence for ultrahigh-pressure metamorphism in the North-East Greenland Caledonides: Geology, v. 30, p. 551–554, https://doi.org/10.1130/0091-7613(2002)030<0551:FEFUPM>2.0.CO;2.
- Gleadow, A.J.W., and Duddy, I.R., 1981, A natural long-term track annealing experiment for apatite: Nuclear Tracks, v. 5, p. 169–174, https://doi.org/10.1016/0191-278X(81)90039-1.
- Graham, S.A., Hendrix, M.S., Johnson, C.L., Badamgarav, D., Badarch, G., Amory, J., Porter, M., Barsbold, R., Webb, L.E., and Hacker, B.R., 2001, Sedimentary record and tectonic implications of Mesozoic rifting in southeast Mongolia: Geological Society of America Bulletin, v. 113, p. 1560–1579, https://doi.org/10.1130/0016-7606(2001)113-1560:SRATIO>-2.0.CO;2.
- Guillot, S., Hattori, K., Agard, P., Schwartz, S., and Vidal, O., 2009, Exhumation processes in oceanic and continental subduction contexts: A review, in Lallemand, S., and Funiciello, F., eds.,

- Subduction Zone Geodynamics: Berlin, Heidelberg, Springer Verlag, p. 175–205, https://doi.org/10.1007/978-3-540-87974-9_10.
- Guo, Z.J., Zhang, Z.C., Zhang, C., Liu, C., Zhang, Y., Wang, J., and Chen, W.M., 2008, Lateral growth of the Altyn Tagh strike-slip fault at the north margin of the Qinghai-Tibet Plateau: Late Cenozoic strike-slip faults and the crustal stability in the Beishan area, Gansu, China: Geological Bulletin of China, v. 27, no. 10, p. 1678-1686 (in Chinese with English abstract).
- Hacker, B., Luffi, P., Lutkov, V., Minaev, V., Ratschbacher, L., Plank, T., Ducea, M., Patino-Douce, A., McWilliams, M., and Metcalf, J., 2005, Near-ultrahigh pressure processing of continental crust: Miocene crustal xenoliths from the Pamir: Journal of Petrology, v. 46, p. 1661–1687, https://doi.org/10.1093/petrology/egi030.
- Hacker, B.R., Gerya, T.V., and Gilotti, J.A., 2013, Formation and exhumation of ultrahigh–pressure terranes: Elements, v. 9, p. 289–293, https://doi.org/10.2113/gselements.9.4.289.
- Haproff, P.J., Odlum, M.L., Zuza, A.V., Yin, A., and Stockli, D.F., 2020, Structural and thermochronologic constraints on the Cenozoic tectonic development of the northern Indo-Burma Ranges: Tectonics, v. 39, https://doi.org/10.1029/2020TC006231.
- He, Z.Y., Sun, L.X., Mao, L.J., Zong, K.Q., and Zhang, Z.M., 2015, Zircon U-Pb and Hf isotopic study of gneiss and granodiorite from the southern Beishan orogenic collage: Mesoproterozoic magmatism and crustal growth: Chinese Science Bulletin, v. 60, p. 389–399, https://doi. org/10.1360/N972014-00898 (in Chinese with English abstract).
- Heilbronner, R., and Tullis, J., 2006, Evolution of c axis pole figures and grain size during dynamic recrystallization: Results from experimentally sheared quartzite: Journal of Geophysical Research, v. 111, B10202, https://doi.org/10.1029/2005JB004194.
- Heubeck, C., 2001, Assembly of central Asia during the middle and late Paleozoic, in Hendrix, M.S., and Davis, G.A., eds., Paleozoic and Mesozoic Tectonic Evolution of Central and Eastern Asia: From Continental Assembly to Intracontinental Deformation: Geological Society of America Memoir 194, p. 1–22, https://doi.org/10.1130/0-8137-1194-0.1.
- Horn, I., Rudnick, R.L., and McDonough, W.F., 2000, Precise elemental and isotope ratio determination by simultaneous solution nebulization and laser ablation-ICP-MS: Application to U-Pb geochronology—Erratum: Chemical Geology, v. 167, p. 405–425, https://doi.org/10.1016/S0009-2541(00)00229-1.
- Hirth, G., and Tullis, J., 1992, Dislocation creep regimes in quartz aggregates: Journal of Structural Geology, v. 14, p. 145–159, https://doi.org/10.1016/0191-8141(92)90053-Y.
- Hou, Q.Y., Wang, Z., Liu, J.B., Wang, J., and Li, D.F., 2012, Geochemistry characteristics and SHRIMP dating of Yueyashan ophiolite in Beishan Orogen: Geoscience, v. 26, p. 1008–1018 (in Chinese with English abstract).
- Hsü, K.J., and Chen, H.H., 1999, Geologic Atlas of China: An Application of the Tectonic Facies Concept to the Geology of China: New York, Elsevier, 262 p.
- Hu, X.Z., Zhao, G.C., Hu, X.Y., Liao, Y.F., and Cheng, H.F., 2015, Geological characteristics, formation epoch and geotectonic significance of the Yueyashan ophiolitic tectonic mélange in Beishan area, Inner Mongolia: Geological Bulletin of China, v. 34, p. 425–436 (in Chinese with English abstract).
- Husson, L., Brun, J.-P., Yamato, P., and Faccenna, C., 2009, Episodic slab rollback fosters exhumation of HP-UHP rocks: Geophysical Journal International, v. 179, p. 1292–1300, https://doi.org/10.1111/j.1365-246X.2009.04372.x.
- Jackson, S.E., Pearson, N.J., Griffin, W.L., and Belousova, E.A., 2004, The application of laser ablation-inductively coupled plasma-mass spectrometry to in situ U-Pb zircon geochronology: Chemical Geology, v. 211, p. 47–69, https://doi.org/10.1016/j.chemgeo.2004.06.017.
- Jahn, B.M., Wu, F.Y., and Hong, D.W., 2000, Important crustal growth in the Phanerozoic: Isotopic evidence of granitoids from east-central Asia: Journal of Earth System Science, v. 109, p. 5–20, https://doi.org/10.1007/BF02719146.
- Jepson, G., Carrapa, B., Gillespie, J., Feng, R., DeCelles, P.G., Kapp, P., Tabor, C.R., and Zhu, J., 2021, Climate as the great equalizer of continental-scale erosion: Geophysical Research Letters, v. 48, https://doi.org/10.1029/2021GL095008.
- Jiang, S.H., Nie, F.J., Chen, W., Liu, Y., Bai, D.M., Liu, X.Y., and Zhang, S.H., 2003, Discovery of Yanshanian K-feldspar granite in Huitongshan copper deposit, Gansu Province, and its implication: Mineralium Deposita, v. 22, no. 2, p. 185–190 (in Chinese with English abstract).
- Jin, X., Zhang, Y.X., Whitney, D.L., Zhang, K.J., Raia, N.H., Hamelin, C., Hu, J.C., Lu, L., Zhou, X.Y., and Khalid, S.B., 2021, Crustal material recycling induced by subduction erosion and subduction-channel exhumation: A case study of central Tibet (western China) based on P-Tt paths of the eclogite-bearing Baqing metamorphic complex: Geological Society of America Bulletin, v. 133, p. 1575–1599, https://doi.org/10.1130/B35638.1.

- Johnson, C.L., Webb, L.E., Graham, S.A., Hendrix, M.S., and Badarch, G., 2001, Sedimentary and structural records of late Mesozoic high-strain extension and strain partitioning, East Gobi basin, southern Mongolia, in Hendrix, M.S., and Davis, G.A., eds., Paleozoic and Mesozoic Tectonic Evolution of Central and Eastern Asia: From Continental Assembly to Intracontinental Deformation: Geological Society of America Memoir 194, p. 413–433, https://doi .org/10.1130/0-8137-1194-0.413.
- Jolivet, L., Daniel, J.M., Truffert, C., and Goffé, B., 1994, Exhumation of deep crustal metamorphic rocks and crustal extension in arc and back-arc regions: Lithos, v. 33, p. 3–30, https://doi .org/10.1016/0024-4937(94)90051-5.
- Jolivet, L., Raimbourg, H., Labrousse, L., Avigad, D., Leroy, Y., Austrheim, H., and Andersen, T.B., 2005, Softening trigerred by eclogitization, the first step toward exhumation during continental subduction: Earth and Planetary Science Letters, v. 237, p. 532–547, https://doi .org/10.1016/j.epsl.2005.06.047.
- Kirby, E., Reiners, P.W., Krol, M.A., Whipple, K.X., Hodges, K.V., Farley, K.A., Tang, W.K., and Chen, Z.L., 2002, Late Cenozoic evolution of the eastern margin of the Tibetan Plateau: Inferences from ⁴⁰Ar/⁵⁰Ar and (U-Th)/He thermochronology: Tectonics, v. 21, p. 1-1–1-20, https:// doi.org/10.1029/2000TC001246.
- Krohe, A., and Mposkos, E., 2002, Multiple generations of extensional detachments in the Rhodope Mountains (northern Greece): Evidence of episodic exhumation of high-pressure rocks, in Blundell, D.J., Neubauer, F., and von Quadt, A., eds., The Timing and Location of Major Ore Deposits in an Evolving Orogen: Geological Society of London Special Publication 204, p. 151–178. https://doi.org/10.1144/GSL.SP2002.204.01.10.
- Kurz, W., and Froitzheim, N., 2002, The exhumation of eclogite-facies metamorphic rocks—A review of models confronted with examples from the Alps: International Geology Review, v. 44, p. 702–743, https://doi.org/10.2747/0020-6814.44.8.702.
- Kurz, W., Neubauer, F., and Dachs, E., 1998, Eclogite meso- and microfabrics: Implications for the burial and exhumation history of eclogites in the Tauern Window (eastern Alps) from P-T-d paths: Tectonophysics, v. 285, p. 183–209, https://doi.org/10.1016/S0040-1951 (97)00188-1.
- Lardeaux, J.M., Ledru, P., Daniel, I., and Duchene, S., 2001, The Variscan French Massif Central— A new addition to the ultra-high pressure metamorphic 'club': Exhumation processes and geodynamic consequences: Tectonophysics, v. 332, p. 143–167, https://doi.org/10.1016/S0040 -1951(00)00253-5.
- Law, R.D., 1990, Crystallographic fabrics: A selective review of their applications to research in structural geology, in Knipe, R.J., and Rutter, E.H., eds., Deformation Mechanisms, Rheology and Tectonics: Geological Society of London Special Publication 54, p. 335–352, https://doi.org/10.1144/GSL.SP.1990.054.01.30.
- Law, R.D., 2014, Deformation thermometry based on quartz c-axis fabrics and recrystallization microstructures: A review: Journal of Structural Geology, v. 66, p. 129–161, https://doi.org/10.1016/j.jsg.2014.05.023.
- Li, J., Wu, C., Chen, X.H., Zuza, A.V., Haproff, P.J., Yin, A., and Shao, Z.G., 2022, Tectonic evolution of the Beishan orogen in central Asia: Subduction, accretion, and continent-continent collision during the closure of the Paleo-Asian Ocean: Geological Society of America Bulletin, https:// doi.org/10.1130/B36451.1 (in press).
- Li, M., Xin, H.T., Tian, J., Meng, X.F., Pan, Z.L., Chen, C., and Liang, G.Q., 2020, Composition, age and polarity of Gongpoquan arc and its tectonic significance in Beishan orogen: Earth Science, v. 45, p. 2393–2412 (in Chinese with English abstract).
- Li, S., Wang, T., Tong, Y., Hong, D.W., and Ouyang, Z.X., 2009, Identification of the Early Devonian Shuangfengshan A-type granites in Liuyuan area of Beishan and its implications to tectonic evolution: Acta Petrologica et Mineralogica, v. 28, no. 5, p. 407–422 (in Chinese with English abstract).
- Li, S., Wang, T., Tong, Y., Wang, Y.B., Hong, D.W., and Ouyang, Z.X., 2011b, Zircon U-Pb age, origin and its tectonic significances of Huitongshan Devonian K-feldspar granites from Beishan orogen, NW China: Acta Petrologica Sinica, v. 27, no. 10, p. 3055–3070 (in Chinese with English abstract).
- Li, S., Wang, T., Wilde, S.A., Tong, Y., Hong, D.W., and Guo, Q.Q., 2012, Geochronology, petrogenesis and tectonic implications of Triassic granitoids from Beishan, NW China: Lithos, v. 134–135, p. 123–145, https://doi.org/10.1016/j.lithos.2011.12.005.
- Li, X.F., Zhang, C.L., Li, L., Bao, Z.A., Zhang, B.L., and Wei, Q., 2015, Formation age, geochemical characteristics of the Mingshujing pluton in Beishan area of Gansu Province and its geological significance: Acta Petrologica Sinica, v. 31, no. 9, p. 2521–2538 (in Chinese with English abstract).

- Li, Z.H., Xu, Z.Q., and Gerya, T.V., 2011a, Flat versus steep subduction: Contrasting modes for the formation and exhumation of high- to ultrahigh-pressure rocks in continental collision zones: Earth and Planetary Science Letters, v. 301, p. 65–77, https://doi.org/10.1016/j .epsl.2010.10.014.
- Liang, J.W., Feng, Z.W., Ding, J.G., Ma, X.J., Tao, W.X., Liu, Y.L., Yu, Z.K., Jiang, L.Q., and Chang, X.B., 2020, Research on sedimentary characteristics and tectonic setting of Devonian Sangejing Formation in Beishan, Gansu Province: Chinese Journal of Geology, v. 55, no. 4, p. 1012–1024 (in Chinese with English abstract).
- Liang, X., Wang, G.H., Yang, B., Ran, H., Zheng, Y.L., Du, J.X., and Li, L.G., 2017, Stepwise exhumation of the Triassic Lanling high-pressure metamorphic belt in Central Qiangtang, Tibet: Insights from a coupled study of metamorphism, deformation, and geochronology: Tectonics, v. 36, p. 652–670, https://doi.org/10.1002/2016TC004455.
- Liao, J., Malusà, M.G., Zhao, L., Baldwin, S.L., Fitzgerald, P.G., and Gerya, T., 2018, Divergent plate motion drives rapid exhumation of (ultra)high pressure rocks: Earth and Planetary Science Letters, v. 491, p. 67–80, https://doi.org/10.1016/j.epsl.2018.03.024.
- Liou, J.G., Tsujimori, T., Zhang, R.Y., Katayama, I., and Maruyama, S., 2004, Global UHP meta-morphism and continental subduction/collision: The Himalayan model: International Geology Review, v. 46, p. 1–27, https://doi.org/10.2747/0020-6814.46.1.1.
- Liu, Q., Zhao, G.C., Sun, M., Eizenhöfer, P.R., Han, Y.G., Hou, W.Z., Zhang, X.R., Wang, B., Liu, D.X., and Xu, B., 2015, Ages and tectonic implications of Neoproterozoic ortho- and paragneisses in the Beishan Orogenic Belt, China: Precambrian Research, v. 266, p. 551–578, https://doi. org/10.1016/j.precamres.2015.05.022.
- Liu, X.C., Wu, G.G., Chen, B.L., and Shu, B., 2002, Metamorphic history of eclogites from Beishan, Gansu Province: Acta Geoscientia Sinica, v. 23, no. 1, p. 25–29 (in Chinese with English abstract).
- Liu, X.C., Chen, B.L., Jahn, B.M., Wu, G.G., and Liu, Y.S., 2011, Early Paleozoic (ca. 465 Ma) eclogites from Beishan (NW China) and their bearing on the tectonic evolution of the southern Central Asian Orogenic Belt: Journal of Asian Earth Sciences, v. 42, p. 715–731, https://doi.org/10.1016/j.jseaes.2010.10.017.
- Liu, X.Y., and Wang, Q., 1995, Tectonics of orogenic belts in Beishan Mts., western China and their evolution: Dixue Yanjiu, v. 28, p. 37–48 (in Chinese with English abstract).
- Liu, Y.J., Li, W.M., Feng, Z.Q., Wen, Q.B., Neubauer, F., and Liang, C.Y., 2017, A review of the Paleozoic tectonics in the eastern part of Central Asian Orogenic Belt: Gondwana Research, v. 43, p. 123–148, https://doi.org/10.1016/j.gr.2016.03.013.
- Liu, Y.Y., Perchuk, A.L., and Philippot, P., 2019, Eclogites from the Marun-Keu Complex, Polar Urals, Russia: A record of hot subduction and sub-isothermal exhumation, in Zhang, L.F., Zhang, Z.M., Schertl, H.-P. and Wei, C.J., eds., HP-UHP Metamorphism and Tectonic Evolution of Orogenic Belts: Geological Society of London of Special Publication 474, p. 255–274, https:// doi.org/10.1144/SP474.6.
- Lloyd, G.E., and Freeman, B., 1994, Dynamic recrystallization of quartz under greenschist conditions: Journal of Structural Geology, v. 16, p. 867–881, https://doi.org/10.1016/0191-8141(94)90151-1.
- Long, S.P., Kohn, M.J., Kerswell, B.C., Starnes, J.K., Larson, K.P., Blackford, N.R., and Soignard, E., 2020, Thermometry and microstructural analysis imply protracted extensional exhumation of the Tso Morari UHP nappe, northwestern Himalaya: Implication for models of UHP exhumation: Tectonics, v. 39, https://doi.org/10.1029/2020TC006482.
- Ludwig, K.R., 2003, Isoplot 3.00; Berkeley Geochronology Center Special Publication 4, 70 p.
- Malatesta, C., Crispini, L., Federico, L., Capponi, G., and Scambelluri, M., 2012, The exhumation of high pressure ophiolites (Voltri Massif, Western Alps): Insights from structural and petrologic data on metagabbro bodies: Tectonophysics, v. 568–569, p. 102–123, https://doi.org/10.1016/j.tecto.2011.08.024.
- Malusà, M.G., Faccenna, C., Garzanti, E., and Polino, R., 2011, Divergence in subduction zones and exhumation of high pressure rocks (Eocene Western Alps): Earth and Planetary Science Letters, v. 310, p. 21–32, https://doi.org/10.1016/j.epsl.2011.08.002.
- Mancktelow, N.S., 1995, Nonlithostatic pressure during sediment subduction and the development and exhumation of high pressure metamorphic rocks: Journal of Geophysical Research, v. 100, p. 571–583, https://doi.org/10.1029/94JB02158.
- Mao, Q.G., Xiao, W.J., Fang, T.H., Wang, J.B., Han, C.M., Sun, M., and Yuan, C., 2012a, Late Ordovician to early Devonian adakites and Nb-enriched basalts in the Liuyuan area, Beishan, NW China: Implications for early Paleozoic slab-melting and crustal growth in the southern Altaids: Gondwana Research, v. 22, p. 534–553, https://doi.org/10.1016/j.gr.2011.06.006.
- Mao, Q.G., Xiao, W.J., Windley, B.F., Han, C.M., Qu, J.F., Ao, S.J., Zhang, J.E., and Guo, Q.Q., 2012b, The Liuyuan complex in the Beishan, NW China: A Carboniferous–Permian ophiolitic

- fore-arc sliver in the southern Altaids: Geological Magazine, v. 149, p. 483–506, https://doi.org/10.1017/S0016756811000811.
- Marques, F.O., Mandal, N., Ghosh, S., Ranalli, G., and Bose, S., 2018, Channel flow, tectonic over-pressure, and exhumation of high-pressure rocks in the Greater Himalayas: Solid Earth, v. 9, p. 1061–1078, https://doi.org/10.5194/se-9-1061-2018.
- Meesters, A.G.C.A., and Dunai, T.J., 2002, Solving the production-diffusion equation for finite diffusion domains of various shapes: Part I. Implications for low-temperature (U-Th)/He thermochronology: Chemical Geology, v. 186, p. 333–344, https://doi.org/10.1016/S0009-2541 (01)00422-3
- Mei, H.L., Yu, H.F., Li, Q., Lu, S.N., Li, H.M., Zuo, Y.C., Zuo, G.C., Ye, D.J., and Liu, J.C., 1999a, The first discovery of eclogite and Palaeoproterozoic granitoids in the Beishan area, northwestern Gansu Province, China: Chinese Science Bulletin, v. 44, no. 4, p. 356–361, https://doi .org/10.1007/BF02885491 (in Chinese).
- Mei, H.L., Li, H.M., Lu, S.N., Yu, H.F., Zuo, Y.C., and Li, Q., 1999b, The age and origin of the Liuyuan Granitoid, northwestern Gansu: Acta Petrologica et Mineralogica, v. 18, no. 1, p. 14–17 (in Chinese with English abstract).
- Meng, F.C., Fan, Y.Z., Shmelev, V.R., and Kulikova, K.V., 2020, Constraints of eclogites from the Marun-Keu metamorphic complex on the tectonic history of the Polar Urals (Russia): Journal of Asian Earth Sciences, v. 187, https://doi.org/10.1016/j.jseaes.2019.104087.
- Meng, Q.T., Zhang, Z.P., Dong, H.K., and Xu, C., 2021, Chronology, geochemical characteristics and tectonic significance of Aminwusu ophiolite in the Beishan area, Inner Mongolia: Geology and Exploration, v. 57, no. 1, p. 122–135 (in Chinese with English abstract).
- Neumann, B., 2000, Texture development of recrystallised quartz polycrystals unravelled by orientation and misorientation characteristics: Journal of Structural Geology, v. 22, p. 1695–1711, https://doi.org/10.1016/S0191-8141(00)00060-2.
- Nie, S.Y., Yin, A., Rowley, D.B., and Jin, Y.G., 1994, Exhumation of the Dabie Shan ultra-high-pressure rocks and accumulation of the Songpan-Ganzi flysch sequence, central China: Geology, v. 22, p. 999–1002, https://doi.org/10.1130/0091-7613(1994)022<0999:EOTDSU>2.3.CO;2.
- Nielsen, S.G., and Marschall, H.R., 2017, Geochemical evidence for mélange melting in global arcs: Science Advances, v. 3, https://doi.org/10.1126/sciadv.1602402.
- Niu, W.C., Xin, H.T., Duan, L.F., Zhao, Z.L., Zhang, G.Z., Ren, B.F., and Zhang, Y., 2020a, Geochemical characteristics, zircon U-Pb age of SSZ ophiolite in the Baiheshan area of the Beishan orogenic belt, Inner Mongolia, and its indication for the evolution of the Paleo-Asian Ocean: Geological Bulletin of China, v. 39, no. 9, p. 1317–1329 (in Chinese with English abstract).
- Niu, Y.Z., Lu, J.C., Liu, C.Y., Xu, W., Shi, J.Z., and Song, B., 2018a, Geochronology and distribution of the Upper Carboniferous–Lower Permian Ganquan Formation in the Beishan Region, northwestern China and its tectonic implication: Geological Review, v. 64, no. 4, p. 1131–1148 (in Chinese with English abstract).
- Niu, Y.Z., Lu, J.C., Liu, C.Y., Song, B., Shi, J.Z., and Xu, W., 2018b, Chronostratigraphy and regional comparison of marine Permian System in the Beishan Region, North China: Acta Geologica Sinica, v. 92, no. 6, p. 1131–1148 (in Chinese with English abstract).
- Niu, Y.Z., Song, B., Zhou, J.L., Xu, W., Shi, J.Z., Zhang, Y.X., and Lu, J.C., 2020b, Lithofacies and chronology of volcano-sedimentary sequence in the southern Beishan Region, Central Asian Orogenic Belt and its paleogeographical implication: Acta Geologica Sinica, v. 94, no. 2, p. 615–633 (in Chinese with English abstract).
- Niu, Y.Z., Shi, G.R., Wang, J.Q., Liu, C.Y., Zhou, J.L., Lu, J.C., Song, B., and Xu, W., 2021, The closing of the southern branch of the Paleo-Asian Ocean: Constraints from sedimentary records in the southern Beishan Region of the Central Asian Orogenic Belt, NW China: Marine and Petroleum Geology, v. 124, https://doi.org/10.1016/j.marpetgeo.2020.104791.
- Okay, A.I., and Şengör, A.M.C., 1992, Evidence for intracontinental thrust-related exhumation of the ultra-high-pressure rocks in China: Geology, v. 20, p. 411–414, https://doi.org/10.1130/0091-7613(1992)020<0411:EFITRE>2.3.CO;2.
- Okudaira, T., Takeshita, T., Hara, I., and Ando, J., 1995, A new estimate of the conditions for transition from basal <a> to prism [c] slip in naturally deformed quartz: Tectonophysics, v. 250, p. 31–46, https://doi.org/10.1016/0040-1951(95)00039-4.
- Ota, T., Utsunomiya, A., Uchio, Y., Isozaki, Y., Buslov, M.M., Ishikawa, A., Maruyama, S., Kitajima, K., Kaneko, Y., Yamamoto, H., and Katayama, I., 2007, Geology of the Gorny Altai subduction-accretion complex, southern Siberia: Tectonic evolution of an Ediacaran–Cambrian intra-oceanic arc-trench system: Journal of Asian Earth Sciences, v. 30, p. 666–695, https:// doi.org/10.1016/j.jseaes.2007.03.001.
- Osozawa, S., and Pavlis, T., 2007, The high P/T Sambagawa extrusional wedge, Japan: Journal of Structural Geology, v. 29, p. 1131–1147, https://doi.org/10.1016/j.jsg.2007.03.014.

- Osozawa, S., and Wakabayashi, J., 2015, Late stage exhumation of HP metamorphic rocks, progressive localization of strain, and changes in transport direction, Sambagawa belt, Japan: Journal of Structural Geology, v. 75, p. 1–16, https://doi.org/10.1016/j.isg.2015.03.006.
- Parkinson, C.D., Katayama, I., Liou, J.G., and Maruyama, S., 2002, The Diamond-Bearing Kokchetav Massif, Kazakhstan: Petrochemistry and Tectonic Evolution of a Unique Ultrahigh-Pressure Metamorphic Terrane: Tokyo, Universal Academy Press, 527 p.
- Passchier, C.W., and Trouw, R.A.J., 2005, Microtectonics (2nd edition): Berlin, Heidelberg, Springer, 366 p., https://doi.org/10.1007/3-540-29359-0.
- Pickering, J., Matthews, W., Enkelmann, E., Guest, B., Sykes, C., and Koblinger, B.M., 2020, Laser ablation (U-Th-Sm)/He dating of detrital apatite: Chemical Geology, v. 548, https://doi.org/10.1016/j.chemgeo.2020.119683.
- Platt, J.P., 1986, Dynamics of orogenic wedges and the uplift of high-pressure metamorphic rocks: Geological Society of America Bulletin, v. 97, p. 1037–1053, https://doi.org/10.1130 /0016-7606(1986)97<1037:DOOWAT>2.0.CO;2.
- Qu, J.F., Xiao, W.J., Windley, B.F., Han, C.M., Mao, Q.G., Ao, S.J., and Zhang, J.E., 2011, Ordovician eclogites from the Chinese Beishan: Implications for the tectonic evolution of the southern Altaids: Journal of Metamorphic Geology, v. 29, p. 803–820, https://doi.org/10.1111/j.1525 -1314.2011.00942.x.
- Ring, U., Will, T., Glodny, J., Kumerics, C., Gessner, K., Thomson, S., Güngör, T., Monié, P., Okrusch, M., and Drüppel, K., 2007, Early exhumation of high-pressure rocks in extrusion wedges: Cycladic blueschist unit in the eastern Aegean, Greece, and Turkey: Tectonics, v. 26, https://doi.org/10.1029/2005TC001872.
- Saktura, W.M., Buckman, S., Nutman, A.P., Belousova, E.A., Yan, Z., and Aitchison, J.C., 2017, Continental origin of the Gubaoquan eclogite and implications for evolution of the Beishan Orogen, Central Asian Orogenic Belt, NW China: Lithos, v. 294–295, p. 20–38, https://doi.org/10.1016/j.lithos.2017.10.004.
- Schwarzenbach, E.M., Zhong, X., Caddick, M.J., Schmalholz, S.M., Menneken, M., Hecht, L., and John, T., 2021, On exhumation velocities of high-pressure units based on insights from chemical zoning in garnet (Tianshan, NW China): Earth and Planetary Science Letters, v. 570, 117065, https://doi.org/10.1016/j.epsl.2021.117065.
- Şengör, A.M.C., 1984, The Cimmeride Orogenic System and the Tectonics of Eurasia: Geological Society of America Special Paper 195, 74 p., https://doi.org/10.1130/SPE195.
- Şengör, A.M.C., Natal'in, B.A., and Burtman, V.S., 1993, Evolution of the Altaid tectonic collage and Palaeozoic crustal growth in Eurasia: Nature, v. 364, p. 299–307, https://doi.org/10.1038/364299a0.
- Şengör, A.M.C., Natal'in, B.A., Sunal, G., and van der Voo, R., 2018, The tectonics of the Altaids: Crustal growth during the construction of the continental lithosphere of Central Asia between ~750 and ~130 Ma ago: Annual Review of Earth and Planetary Sciences, v. 46, p. 439–494, https://doi.org/10.1146/annurev-earth-060313-054826.
- Shaanxi IGS (Shaanxi Institute of Geological Survey), 2014, Geological map of Xingxingxia sheet, People's Republic of China (scale 1:250,000): Beijing, China, Geology Press, 371 p. (in Chinese).
- Shatsky, V.S., Jagoutz, E., and Ryboshlykov, Y.V., 1996, Eclogites of the North Muya block: Evidence for Vendian collision of the Baikal-Muya ophiolite belt: Doklady Rossiya Academia Nauka, v. 350, p. 677–680.
- Shi, W., Dong, S.W., and Hu, J.M., 2020, Neotectonics around the Ordos Block, North China: A review and new insights: Earth-Science Reviews, v. 200, https://doi.org/10.1016/j.earscirev.2019.102969.
- Shi, W.B., Wang, F., Yang, L.K., Wu, L., and Zhang, W.B., 2018b, Diachronous growth of the Altyn Tagh Mountains: Constraints on propagation of the Northern Tibetan Margin from (U-Th)/ He dating: Journal of Geophysical Research: Solid Earth, v. 123, p. 6000–6018, https://doi.org/10.1029/2017JB014844.
- Shi, Y.R., Zhang, W., Kröner, A., Li, L.L., and Jian, P., 2018a, Cambrian ophiolite complexes in the Beishan area, China, southern margin of the Central Asian Orogenic Belt: Journal of Asian Earth Sciences, v. 153, p. 193–205, https://doi.org/10.1016/j.jseaes.2017.05.021.
- Shigematsu, N., and Tanaka, H., 2000, Dislocation creep of fine-grained recrystallized plagioclase under low-temperature conditions: Journal of Structural Geology, v. 22, p. 65–79, https://doi .org/10.1016/S0191-8141(99)00132-7.
- Smith, D.C., 1984, Coesite in clinopyroxene in the Caledonides and its implications for geodynamics: Nature, v. 310, p. 641–644, https://doi.org/10.1038/310641a0.
- Soldner, J., Yuan, C., Schulmann, K., Štípská, P., Jiang, Y.D., Zhang, Y.Y., and Wang, X.Y., 2020a, Grenvillean evolution of the Beishan Orogen, NW China: Implications for development of an active Rodinian margin: Geological Society of America Bulletin, v. 132, p. 1657–1680, https:// doi.org/10.1130/B35404.1.

- Soldner, J., Štípská, P., Schulmann, K., Yuan, C., Anczkiewicz, R., Sala, D., Jiang, Y.D., Zhang, Y.Y., and Wang, X.Y., 2020b, Coupling of P. T-t-Dhistories of eclogite and metagreywacke—Insights to late Ordovician–Silurian crustal folding events recorded in the Beishan Orogen (NW China): Journal of Metamorphic Geology, v. 38, p. 555–591, https://doi.org/10.1111/jmg.12531.
- Song, D.F., Xiao, W.J., Han, C.M., and Tian, Z.H., 2014, Polyphase deformation of a Paleozoic forearc–arc complex in the Beishan orogen, NW China: Tectonophysics, v. 632, p. 224–243, https://doi.org/10.1016/j.tecto.2014.06.030.
- Song, S.G., Wang, M.J., Wang, C., and Niu, Y.L., 2015, Magmatism during continental collision, subduction, exhumation and mountain collapse in collisional orogenic belts and continental net growth: A perspective: Science China Earth Sciences, v. 58, p. 1284–1304, https://doi .org/10.1007/s11430-015-5102-x (in Chinese with English abstract).
- Starr, P.G., Broadwell, K.S., Dragovic, B., Scambelluri, M., Haws, A.A., Caddick, M.J., Smye, A.J., and Baxter, E.F., 2020, The subduction and exhumation history of the Voltri Ophiolite, Italy: Evaluating exhumation mechanisms for high-pressure metamorphic massifs: Lithos, v. 376–377, 105767, https://doi.org/10.1016/j.lithos.2020.105767.
- Stipp, M., Stünitz, H., Heilbronner, R., and Schmid, S.M., 2002, The eastern Tonale fault zone: A 'natural laboratory' for crystal plastic deformation of quartz over a temperature range from 250 to 700 °C: Journal of Structural Geology, v. 24, p. 1861–1884, https://doi.org/10.1016/S0191-8141(02)00035-4.
- Stockli, D.F., Farley, K.A., and Dumitru, T.A., 2000, Calibration of the apatite (U-Th)/He thermochronometer on an exhumed fault block, White Mountains, California: Geology, v. 28, p. 983–986, https://doi.org/10.1130/0091-7613(2000)28<983:COTAHT>2.0.CO:2.
- Sun, L.X., Zhang, J.H., Ren, B.F., Niu, W.C., Ren, Y.W., and Zhang, K., 2017, Geochemical characteristics and U-Pb age of Baiyunshan ophiolite mélange in the Beishan orogenic belt and their geological implications: Acta Petrologica et Mineralogica, v. 36, no. 2, p. 131–147 (in Chinese with English abstract).
- Sun, X.C., Wang, H.T., Li, T.G., Wei, H.F., Xu, L., and Wang, X.W., 2021, LA-ICP-MS zircon U-Pb ages of the granodiorites from Shuangfengshan in Beishan Mountain, Gansu Province, and its tectonic significance: Acta Petrologica et Mineralogica, v. 40, no. 2, p. 171–184 (in Chinese with English abstract).
- Tagiri, M., Yano, T., Bakirov, A., Nakajima, T., and Uchiumi, S., 1995, Mineral parageneses and metamorphic P-T paths of ultrahigh-pressure eclogites from Kyrghystan Tien-Shan: Island Arc, v. 4, p. 280–292, https://doi.org/10.1111/j.1440-1738.1995.tb00150.x.
- Tian, Y.T., Kohn, B.P., Gleadow, A.J.W., and Hu, S.B., 2014b, A thermochronological perspective on the morphotectonic evolution of the southeastern Tibetan Plateau: Journal of Geophysical Research: Solid Earth, v. 119, p. 676–698, https://doi.org/10.1002/2013JB010429.
- Tian, Z.H., Xiao, W.J., Windley, B.F., Lin, L.N., Han, C.M., Zhang, J.E., Wan, B., Ao, S.J., Song, D.F., and Feng, J.Y., 2014a, Structure, age, and tectonic development of the Huoshishan-Niujuanzi ophiolitic mélange, Beishan, southernmost Altaids: Gondwana Research, v. 25, p. 820–841, https://doi.org/10.1016/j.gr.2013.05.006.
- Tian, Z.H., Xiao, W.J., Windley, B.F., Huang, P., Zhang, J.E., Ao, S.J., Zhang, Z.Y., Song, D.F., and Liu, F.L., 2021, Two key switches in regional stress field during multi-stage deformation in the Carboniferous—Triassic southernmost Altaids (Beishan, NW China): Response to oroclinerelated roll-back processes: Geological Society of America Bulletin, v. 133, p. 2591–2611, https://doi.org/10.1130/B35898.1.
- Togonbaeva, A., Takasu, A., Bakirov, A.A., Sakurai, T., Tagiri, M., Bakirov, A.B., and Sakiev, K., 2009, CHIME monazite ages of garnet-chloritoid-talc schists in the Makbal Complex, Northern Kyrgyz Tien-Shan: First report of the age of the UHP metamorphism: Journal of Mineralogical and Petrological Sciences, v. 104, p. 77–81, https://doi.org/10.2465/jmps.081022e.
- Toy, V.G., Prior, D.J., and Norris, R.J., 2008, Quartz fabrics in the Alpine Fault mylonites: Influence of pre-existing preferred orientations on fabric development during progressive uplift: Journal of Structural Geology, v. 30, p. 602–621, https://doi.org/10.1016/j.jsg.2008.01.001.
- Tsurumi, J., Hosonuma, H., and Kanagawa, K., 2003, Strain localization due to a positive feedback of deformation and myrmekite-forming reaction in granite and aplite mylonites along the Hatagawa Shear Zone of NE Japan: Journal of Structural Geology, v. 25, p. 557–574, https:// doi.org/10.1016/S0191-8141(02)00048-2.
- Vincent, S.J., and Allen, M.B., 2001, Sedimentary record of Mesozoic intracontinental deformation in the eastern Junggar Basin, northwest China: Response to orogeny at the Asian margin, in Hendrix, M.S., and Davis, G.A., eds., Paleozoic and Mesozoic Tectonic Evolution of Central and Eastern Asia: From Continental Assembly to Intracontinental Deformation: Geological Society of America Memoir 194, p. 341–360, https://doi.org/10.1130/0-8137-1194-0.341.

- Wang, G.Q., Li, X.M., Xu, X.Y., Yu, J.Y., and Wu, P., 2014b, Zircon U-Pb chronological study of the Hongshishan ophiolite in the Beishan area and their tectonic significance: Acta Petrologica Sinica, v. 30, no. 6, p. 1685–1694 (in Chinese with English abstract).
- Wang, G.Q., Li, X.M., Xu, X.Y., Yu, J.Y., Wu, P., and Ji, B., 2021, Research status and progress of Paleozoic ophiolites in Beishan orogenic belt: Geological Bulletin of China, v. 40, no. 1, p. 71–81 (in Chinese with English abstract).
- Wang, J.X., Zhang, K.X., Jin, J.S., Song, B.W., Yu, Y., Wang, L.J., Wang, S.D., and Sun, S., 2020a, Early Paleozoic ocean plate stratigraphy of the Beishan orogenic zone, NW China: Implications for regional tectonic evolution: Acta Geologica Sinica (English edition), v. 94, p. 1042–1059, https://doi.org/10.1111/1755-6724.14559.
- Wang, L., Kusky, T.M., Polat, A., Wang, S.J., Jiang, X.F., Zong, K.Q., Wang, J.P., Deng, H., and Fu, J.M., 2014a, Partial melting of deeply subducted eclogite from the Sulu orogen in China: Nature Communications, v. 5, 5604, https://doi.org/10.1038/ncomms6604.
- Wang, L., Wang, S.J., Brown, M., Zhang, J.F., Feng, P., and Jin, J.M., 2018a, On the survival of intergranular coesite in UHP eclogite: Journal of Metamorphic Geology, v. 36, no. 2, p. 173–194, https://doi.org/10.1111/jmg.12288.
- Wang, S.D., Zhang, K.X., Song, B.W., Li, S.C., Li, M., and Zhou, J., 2018b, Geochronology and geochemistry of the Niujuanzi ophiolitic mélange, Gansu Province, NW China: Implications for tectonic evolution of the Beishan Orogenic Collage: International Journal of Earth Sciences, v. 107, p. 269–289, https://doi.org/10.1007/s00531-017-1489-2.
- Wang, Q.C., and Cong, B.L., 1999, Exhumation of UHP terranes: A case study from the Dabie Mountains, Eastern China: International Geology Review, v. 41, p. 994–1004, https://doi.org/10.1080/00206819909465185.
- Wang, Y. (Yang), Zhang, L.F., Li, Z.H., Li, Q.Y., and Bader, T., 2019, The exhumation of subducted oceanic-derived eclogites: Insights from phase equilibrium and thermomechanical modeling: Tectonics, v. 38, p. 1764–1797, https://doi.org/10.1029/2018TC005349.
- Wang, Y. (Ye), Chen, X.H., Zhang, Y.Y., Yin, Z., Zuza, A.V., Yin, A., Wang, Y.C., Ding, W.C., Xu, S.L., Zhang, Y.P., Li, B., and Shao, Z.G., 2022, Superposition of Cretaceous and Cenozoic deformation in northern Tibet: A far-field response to the tectonic evolution of the Tethyan orogenic system: Geological Society of America Bulletin, v. 134, p. 501–525, https://doi.org/10.1130/B35944.1.
- Wang, Y. (Yu), Luo, Z.H., Santosh, M., Wang, S.Z., and Wang, N., 2017, The Liuyuan Volcanic Belt in NW China revisited: Evidence for Permian rifting associated with the assembly of continental blocks in the Central Asian Orogenic Belt: Geological Magazine, v. 154, p. 265–285, https:// doi.org/10.1017/S0016756815001077.
- Wang, Y.H., Zhang, F.F., Li, B.C., Xue, C.J., Liu, J.J., Zhao, Y., and Zhang, W., 2020b, Geology and genesis of the Cihai mafic intrusions in Beishan Terrane, Xinjiang, Northwest China: Implication for iron mineralization and tectonic setting: Ore Geology Reviews, v. 121, https://doi. org/10.1016/j.oregeorev.2020.103573.
- Warren, C.J., 2013, Exhumation of (ultra-)high-pressure terranes: Concepts and mechanisms: Solid Earth, v. 4, p. 75–92, https://doi.org/10.5194/se-4-75-2013.
- Webb, L.E., Graham, S.A., Johnson, C.L., Badarch, G., and Hendrix, M.S., 1999, Occurrence, age, and implications of the Yagan–Onch Hayrhan metamorphic core complex, southern Mongolia: Geology, v. 27, p. 143–146, https://doi.org/10.1130/0091-7613(1999)027<0143:0AAIOT>2.3.CO:2.
- Wilhem, C., Windley, B.F., and Stampfli, G.M., 2012, The Altaids of Central Asia: A tectonic and evolutionary innovative review: Earth-Science Reviews, v. 113, p. 303–341, https://doi.org/10.1016/j.earscirev.2012.04.001.
- Windley, B.F., and Xiao, W.J., 2018, Ridge subduction and slab windows in the Central Asian Orogenic Belt: Tectonic implications for the evolution of an accretionary orogen: Gondwana Research, v. 61, p. 73–87, https://doi.org/10.1016/j.gr.2018.05.003.
- Windley, B.F., Alexeiev, D., Xiao, W.J., Kröner, A., and Badarch, G., 2007, Tectonic models for accretion of the Central Asian Orogenic Belt: Journal of the Geological Society, v. 164, p. 31–47, https://doi.org/10.1144/0016-76492006-022.
- Wu, C., Liu, C.F., Zhu, Y., Zhou, Z.G., Jiang, T., Liu, W.C., Li, H.Y., Wu, C., and Ye, B.Y., 2016a, Early Paleozoic magmatic history of central Inner Mongolia, China: Implications for the tectonic evolution of the Southeast Central Asian Orogenic Belt: International Journal of Earth Sciences, v. 105, p. 1307–1327, https://doi.org/10.1007/s00531-015-1250-7.
- Wu, C., Yin, A., Zuza, A.V., Zhang, J.Y., Liu, W.C., and Ding, L., 2016b, Pre-Cenozoic geologic history of the central and northern Tibetan Plateau and the role of Wilson cycles in constructing the Tethyan orogenic system: Lithosphere, v. 8, no. 3, p. 254–292, https://doi.org/10.1130/L494.1.
- Wu, C., Liu, C.F., Fan, S., Zuza, A.V., Ding, L., Liu, W.C., Ye, B.Y., Yang, S.J., and Zhou, Z.G., 2020, Structural analysis and tectonic evolution of the western domain of the Eastern Kunlun

- Range, northwest Tibet: Geological Society of America Bulletin, v. 132, p. 1291–1315, https://doi.org/10.1130/B35388.1.
- Wu, C., Li, J., Zuza, A.V., Haproff, P.J., Chen, X.H., and Ding, L., 2022a, Proterozoic-Phanerozoic tectonic evolution of the Qilian Shan and Eastern Kunlun Range, northern Tibet: Geological Society of America Bulletin, v. 134, p. 2179–2205, https://doi.org/10.1130/B36306.1.
- Wu, C., Li, J., Zuza, A.V., Haproff, P.J., Yin, A., and Ding, L., 2022b, Paleoproterozoic-Paleozoic tectonic evolution of the Longshou Shan, western North China craton: Geosphere, v. 18, p. 1177–1193, https://doi.org/10.1130/GES02491.1.
- Wu, L., Monié, P., Wang, F., Lin, W., Ji, W.B., Bonno, M., Münch, P., and Wang, Q.C., 2016c, Cenozoic exhumation history of Sulu terrane: Implications from (U-Th)/He thermochrology: Tectonophysics, v. 672–673, p. 1–15, https://doi.org/10.1016/j.tecto.2016.01.035.
- Wu, L., Shi, G.H., Danišík, M., Zhang, Z.Y., Wang, Y.Z., and Wang, F., 2019, MK-1 apatite: A new potential reference material for (U-Th)/He dating: Geostandards and Geoanalytical Research, v. 43, p. 301–315, https://doi.org/10.1111/ggr.12258.
- Wu, L., Wang, F., Zhang, Z.Y., Shi, G.H., Danišík, M., He, D.F., Sun, J.B., Wang, Y., Shen, X.M., and Zaw, T., 2021, Reappraisal of the applicability of MK-1 apatite as a reference standard for (U-Th)/ He geochronology: Chemical Geology, v. 575, https://doi.org/10.1016/j.chemgeo.2021.120255.
- Wu, P., Wang, G.Q., Li, X.M., Yu, J.Y., and Kang, L., 2012, The age of Niujuanzi ophiolite in Beishan area of Gansu Province and its geological significance: Geological Bulletin of China, v. 31, no. 12. p. 2032–2037 (in Chinese with English abstract).
- Xiao, W.J., Windley, B.F., Yuan, C., Sun, M., Han, C.M., Lin, S.F., Chen, H.L., Yan, Q.R., Liu, D.Y., Qin, K.Z., Li, J.L., and Sun, S., 2009, Paleozoic multiple subduction–accretion processes of the southern Altaids: American Journal of Science, v. 309, p. 221–270, https://doi.org/10.2475/03.2009.02.
- Xiao, W.J., Mao, Q.G., Windley, B.F., Han, C.M., Qu, J.F., Zhang, J.E., Ao, S.J., Guo, Q.Q., Cleven, N.R., Lin, S.F., Shan, Y.H., and Li, J.L., 2010, Paleozoic multiple accretionary and collisional processes of the Beishan orogenic collage: American Journal of Science, v. 310, p. 1553–1594, https://doi.org/10.2475/10.2010.12.
- Xiao, W.J., Han, C.M., Liu, W., Wan, B., Zhang, J.E., Ao, S.J., Zhang, Z.Y., Song, D.F., Tian, Z.H., and Luo, J., 2014, How many sutures in the southern Central Asian Orogenic Belt: Insights from East Xinjiang–West Gansu (NW China)?: Geoscience Frontiers, v. 5, p. 525–536, https://doi.org/10.1016/j.gsf.2014.04.002.
- Xiao, W.J., Windley, B.F., Sun, S., Li, J.L., Huang, B.C., Han, C.M., Yuan, C., Sun, M., and Chen, H.L., 2015, A tale of amalgamation of three Permo-Triassic collage systems in Central Asia: Oroclines, sutures, and terminal accretion: Annual Review of Earth and Planetary Sciences, v. 43, p. 477–507, https://doi.org/10.1146/annurev-earth-060614-105254.
- Xie, L.W., Zhang, Y.B., Zhang, H.H., Sun, J.F., and Wu, F.Y., 2008, In situ simultaneous determination of trace elements, U-Pb and Lu-Hf isotopes in zircon and baddeleyite: Chinese Science Bulletin, v. 53, p. 1565–1573, https://doi.org/10.1007/s11434-008-0086-y.
- Xu, W., Xu, X.Y., Niu, Y.Z., Song, B., Chen, G.C., Shi, J.Z., Zhang, Y.X., and Li, C.H., 2019, Geochronology and petrogenesis of the Permian marine basalt in the southern Beishan region and their tectonic implications: Acta Geologica Sinica, v. 93, no. 8, p. 1928–1953 (in Chinese with English abstract).
- Yakubchuk, A., 2017, Evolution of the Central Asian Orogenic Supercollage since Late Neoproterozoic revised again: Gondwana Research, v. 47, p. 372–398, https://doi.org/10.1016/j .gr.2016.12.010.
- Yang, H.B., Yang, X.P., Zhan, Y., Cunningham, D., Zhao, L.Q., Sun, X.Y., Hu, Z.K., Huang, X.N., Huang, W.L., and Miao, S.Q., 2019, Quaternary activity of the Beihewan Fault in the southeastern Beishan Wrench Belt, Western China: Implications for crustal stability and intraplate earthquake hazards North of Tibet: Journal of Geophysical Research: Solid Earth, v. 124, p. 13,286–13,309, https://doi.org/10.1029/2018JB017209.
- Yang, H.B., Cunningham, D., and Yang, X.P., 2021a, Quaternary crustal reactivation of the south-western Beishan, NW China: The Liuyuan sinistral transpressional duplex: Tectonophysics, v. 803, https://doi.org/10.1016/j.tecto.2021.228758.
- Yang, J.S., Wu, C.L., Chen, S.Y., Shi, R.D., Zhang, J.X., Meng, F.C., Zuo, G.C., Wu, H.Q., and Constantinovskaya, E., 2006, Neoproterozoic eclogitic metamorphic age of the Beishan eclogite of Gansu, China: Evidence from SHRIMP U-Pb isotope dating: Geology in China, v. 33, no. 2, p. 317–325 (in Chinese with English abstract).
- Yang, Q., Shi, W., Hou, G.T., Zhang, Y., and Zhao, Y.L., 2021b, Late Mesozoic intracontinental deformation in the northern margin of the North China Craton: A case study from the Shangyi Basin, northwestern Hebei Province, China: Frontiers in Earth Science, v. 9, https://doi.org/10.3389/feart.2021.710758.

- Ye, X.F., Zong, K.Q., Zhang, Z.M., He, Z.Y., Liu, Y.S., Hu, Z.C., and Wang, W., 2013, Geochemistry of Neoproterozoic granite in Liuyuan area of southern Beishan orogenic belt and its geological significance: Geological Bulletin of China, v. 32, no. 2–3, p. 307–317 (in Chinese with English abstract).
- Yin, A., 2010, Cenozoic tectonic evolution of Asia: A preliminary synthesis: Tectonophysics, v. 488, p. 293–325, https://doi.org/10.1016/j.tecto.2009.06.002.
- Yin, A., and Harrison, T.M., 2000, Geologic evolution of the Himalayan-Tibetan orogen: Annual Review of Earth and Planetary Sciences, v. 28, p. 211–280, https://doi.org/10.1146/annurev.earth.28.1.211.
- Yin, A., Manning, C.E., Lovera, O., Menold, C.A., Chen, X.H., and Gehrels, G.E., 2007, Early Paleozoic tectonic and thermomechanical evolution of ultrahigh-pressure (UHP) metamorphic rocks in the northern Tibetan Plateau, northwest China: International Geology Review, v. 49, p. 681–716, https://doi.org/10.2747/0020-6814.49.8.681.
- Yu, H.F., Mei, H.L., Lu, S.N., and Li, Q., 1999, Mineral characteristics and temperature-pressure conditions of Beishan eclogite, Gansu Province: Journal of Changchun University of Science and Technology, v. 29, no. 2, p. 110–115 (in Chinese with English abstract).
- Yu, J.Y., Li, X.M., Wang, G.Q., Wu, P, and Yan, Q.J., 2012, Zircon U-Pb ages of Huitongshan and Zhang-fangshan ophiolite in Beishan of Gansu–Inner Mongolia border area and their significance: Geological Bulletin of China, v. 31, no. 12, p. 2038–2045 (in Chinese with English abstract).
- Yuan, Y., Zong, K.Q., He, Z.Y., Klemd, R., Liu, Y.S., Hu, Z.C., Guo, J.L., and Zhang, Z.M., 2015, Geochemical and geochronological evidence for a former early Neoproterozoic microcontinent in the South Beishan Orogenic Belt, southernmost Central Asian Orogenic Belt: Precambrian Research, v. 266, p. 409–424, https://doi.org/10.1016/j.precamres.2015.05.034.
- Yuan, Y., Zong, K.Q., Cawood, P.A., Cheng, H., Yu, Y.Y., Guo, J.L., Liu, Y.S., Hu, Z.C., Zhang, W., and Li, M., 2019, Implication of Mesoproterozoic (~1.4 Ga) magmatism within microcontinents along the southern Central Asian Orogenic Belt: Precambrian Research, v. 327, p. 314–326, https://doi.org/10.1016/j.precamres.2019.03.014.
- Yun, L., Zhang, J., Wang, J., Zhao, Z.T., Bao, Y.T., Zhuang, H.Y., Chen, S., Zhang, J.J., Zhang, J., Zhao, H., and Zhang, B.H., 2021, Discovery of active faults in the southern Beishan area, NW China: Implications for regional tectonics: Journal of Geometry, v. 27, no. 2, p. 195–207 (in Chinese with English abstract).
- Zhang, J., and Cunningham, D., 2012, Kilometer-scale refolded folds caused by strike-slip reversal and intraplate shortening in the Beishan region, China: Tectonics, v. 31, TC3009, https://doi.org/10.1029/2011TC003050.
- Zhang, J.J., 2014, The petrogenesis and mineralization potential of two types of mafic-ultramafic intrusions, Gansu Beishan, China [Ph.D. thesis]: Xi'an, China, Chang'an University (in Chinese with English abstract).
- Zhang, L.F., and Wang, Y., 2020, The exhumation of high- and ultrahigh-pressure metamorphic terranes in subduction zone: Questions and discussions: Science China Earth Sciences, v. 63, p. 1884–1903, https://doi.org/10.1007/s11430-020-9579-3 (in Chinese with English abstract).
- Zhang, Y.Y. (Yuanyuan), and Guo, Z.J., 2008, Accurate constraint on formation and emplacement age of Hongliuhe ophiolite, boundary region between Xinjiang and Gansu Provinces and its tectonic implications: Acta Petrologica Sinica, v. 24, no. 4, p. 803–809 (in Chinese with English abstract).
- Zhang, Y.Y. (Yuanyuan), Dostal, J., Zhao, Z.H., Liu, C., and Guo, Z.J., 2011, Geochronology, geochemistry and petrogenesis of mafic and ultramafic rocks from Southern Beishan area, NW China: Implications for crust-mantle interaction: Gondwana Research, v. 20, p. 816–830, https://doi.org/10.1016/j.gr.2011.03.008.
- Zhang, Y.Y. (Yunying), Yuan, C., Sun, M., Long, X.P., Xia, X.P., Wang, X.Y., and Huang, Z.Y., 2015, Permian doleritic dikes in the Beishan Orogenic Belt, NW China: Asthenosphere-lithosphere interaction in response to slab break-off: Lithos, v. 233, p. 174–192, https://doi.org/10.1016/j.lithos.2015.04.001.

- Zhang, Z.P., Xin, H.T., Cheng, H.F., Zhang, Y., Liang, G.Q., Ti, Z.H., Zhu, W., Su, P.T., Du, J.L., Wang, M., and Zhao, Q.Y., 2020, The discovery of the Elegen ophiolite in Beishan orogenic belt, Inner Mongolia: Evidence for the east extension of the Hongshishan-Baiheshan ophiolite belt: Geological Bulletin of China, v. 39, no. 9, p. 1389–1403 (in Chinese with English abstract).
- Zhao, K.Q., Ma, S.M., Xi, M.J., Yang, J.Z., Cai, Y.W., and Gong, J.J., 2020, The LA-ICP.MS zircon U-Pb ages and geochemical characteristics of Late Paleozoic intermediate-acidic intrusive complexes in Shibanjing area, Beishan Mountains, Inner Mongolia, and their geological significance: Geological Review, v. 66, no. 1, p. 69–87 (in Chinese with English abstract).
- Zhao, Z.H., Guo, Z.J., and Wang, Y., 2007, Geochronology, geochemical characteristics and tectonic implications of the granitoids from Liuyuan area, Beishan, Gansu province, northwest China: Acta Petrologica Sinica, v. 23, no. 8, p. 1847–1860 (in Chinese with English abstract).
- Zheng, R.G., Xiao, W.J., Li, J.Y., Wu, T.R., and Zhang, W., 2018, A Silurian–early Devonian slab window in the southern Central Asian Orogenic Belt: Evidence from high-Mg diorites, adakites and granitoids in the western Central Beishan region, NW China: Journal of Asian Earth Sciences, v. 153, p. 75–99, https://doi.org/10.1016/j.jseaes.2016.12.008.
- Zheng, R.G., Li, J.Y., Zhang, J., and Xiao, W.J., 2021, A prolonged subduction-accretion in the southern Central Asian Orogenic Belt: Insights from anatomy and tectonic affinity for the Beishan complex: Gondwana Research, v. 95, p. 88–112, https://doi.org/10.1016/j.gr.2021.02.022.
- Zheng, Y., Zhang, Q., Wang, Y., Liu, R., Wang, S.G., Zuo, G., Wang, S.Z., Lkaasuren, B., Badarch, G., and Badamgarav, Z., 1996, Great Jurassic thrust sheets in Beishan (North Mountains) Gobi areas of China and southern Mongolia: Journal of Structural Geology, v. 18, p. 1111–1126, https://doi.org/10.1016/0191-8141/96)00038-7.
- Zhu, J., Lv, X.B., and Peng, S.G., 2016, U-Pb zircon geochronology, geochemistry and tectonic implications of the early Devonian granitoids in the Liuyuan area, Beishan, NW China: Geosciences Journal, v. 20, p. 609–625, https://doi.org/10.1007/s12303-016-0004-2.
- Zonenshain, L.P., Kuz'min, M.I., and Natapov, L.M., 1990, Geology of the USSR: A Plate-Tectonic Synthesis: American Geophysical Union Geodynamics Series 21, 242 p., https://doi.org/10 .1029/GD021.
- Zong, K.Q., Klemd, R., Yuan, Y., He, Z.Y., Guo, J.L., Shi, X.L., Liu, Y.S., Hu, Z.C., and Zhang, Z.M., 2017, The assembly of Rodinia: The correlation of early Neoproterozoic (ca. 900 Ma) high-grade metamorphism and continental arc formation in the southern Beishan Orogen, southern Central Asian Orogenic Belt (CAOB): Precambrian Research, v. 290, p. 32–48, https://doi.org/10.1016/j.precamres.2016.12.010.
- Zuo, G.C., Liu, C.Y., Bai, W.C., and Feng, Y.Z., 1995, Volcano-molasse geological structure and geochemical signature in Devonian period collision orogenic in Beishan, Gansu: Acta Geologica Gansu, v. 4, no. 1, p. 35–43 (in Chinese with English abstract).
- Zuo, G.C., Zhang, S.L., Wang, X., and Jin, S.Q., 1987, Characteristics of the turbidite and volcanic-sedimentary assemblages of Cambrian-Middle Ordovician in the Xichangjing area of Beishan: Acta Sedimentologica Sinica, v. 5, no. 2, p. 63–71 (in Chinese with English abstract).
- Zuo, G.C., Zhang, S.L., He, G.Q., and Zhang, Y., 1991, Plate tectonic characteristics during the early Paleozoic in Beishan near the Sino-Mongolian border region, China: Tectonophysics, v. 188, p. 385–392, https://doi.org/10.1016/0040-1951(91)90466-6.
- Zuza, A.V., and Yin, A., 2017, Balkatach hypothesis: A new model for the evolution of the Pacific, Tethyan, and Paleo-Asian oceanic domains: Geosphere, v. 13, p. 1664–1712, https://doi.org/10.1130/GES01463.1.
- Zuza, A.V., Wu, C., Reith, R.C., Yin, A., Li, J.H., Zhang, J.Y., Zhang, Y.X., Wu, L., and Liu, W.C., 2018, Tectonic evolution of the Qilian Shan: An early Paleozoic orogen reactivated in the Cenozoic: Geological Society of America Bulletin, v. 130, p. 881–925, https://doi.org/10.1130/B31721.1.
- Zuza, A.V., Cao, W.R., Hinz, N.H., DesOrmeau, J.W., Odlum, M.L., and Stockli, D.F., 2019, Foot-wall rotation in a regional detachment fault system: Evidence for horizontal-axis rotational flow in the Miocene Searchlight pluton, NV: Tectonics, v. 38, p. 2506–2539, https://doi.org/10.1029/2019TC005513.